



University of Cagliari

University of Sassari

PhD Course in Chemical Science and Technology

XXXVI cycle

Doctoral Thesis

Exploring *Intra* and *Inter*-Molecular Engineering of Thiophene-Based Derivative for the Development of Advanced Organic Semiconductors

PhD Candidate

Anna Laura Sanna

Supervisor

Prof. Giuseppe Sforazzini

Co-Tutor

Prof. Andrea Porcheddu

Academic Year 2023- 2024

Acknowledgments

I wish to express my sincere gratitude to my supervisor, Prof. Giuseppe Sforazzini, for his precious guidance, support, and encouragement throughout my doctoral studies. His expertise and insights have been invaluable in shaping the direction and success of my research. My gratitude extends to my co-supervisor, Prof. Andrea Porcheddu, for sharing essential tools and spaces crucial for the advancement of the project.

It is my earnest desire to thank all those who contributed to the advancement of the research project: Prof.ssa Safaa Shoee (Institute of Physics and Astronomy, University of Potsdam), the research groups led by Prof. Massimiliano Arca and Prof.ssa M. Carla Aragoni, Prof. Vito Lippolis (Department of Chemical and Geological Science, University of Cagliari), Prof. Piero Cosseddu (Department of Electrical and Electronic Engineering, University of Cagliari), Prof. Arrigo Calzolari (CNR-NANO, Istituto Nanoscienze, Modena).

I would like to thank Prof. Holger Frauenrath from the Institute of Materials at the École Polytechnique Fédérale de Lausanne (EPFL), Switzerland, for involving me in the research project conducted at the foreign institution. I also thank the entire LMOM research group for their assistance with the laboratory activities at EPFL.

I extend my profound gratitude to Prof. Carlo Ricci and Dr.ssa Stefania Porcu for their contribution in collecting data and generosity in allowing the use of the equipments located at Department of Physics at the University of Cagliari.

I would like to thank Prof. Enzo Cadoni, Prof. M. Grazia Cabiddu, and Prof. Claudia Fattuoni (Department of Chemical and Geological Science, University of Cagliari) for providing access to their laboratories and equipment during my doctoral studies.

Additionally, I would like to express gratitude to Dr.ssa Sandrina Lampis, Dr. Enrico Podda and Dr. Giulio Ferino (Centro Servizi per la Ricerca, University of Cagliari) for their availability in performing fundamental analysis for my research.

I would like to thank all my research team, particularly Bachelor and Master Degree Students who contribute to the development of the results obtained: Dr. Giuseppe Seddone, Dr. Federico Sbressa, Dr.ssa Giulia D'Alise, Dr. Simone Acca.

Abbreviations List

^{1}H-NMR = Proton nuclear magnetic resonance

^{13}C-NMR = Carbon nuclear magnetic resonance

Å = Ångström

A(t) = Maximum absorbance of light

A_0 = Time zero absorbance

A_∞ = Maximum absorbance amplitude

AB = Azobenzene

ALA = alanine

BHJs = Bulk Heterojunctions

BuLi = Buthyllithium

BTR = Bithiophene-Rhodanine

BTR-2S = Bithiophene-Rhodanine Disulphur

$CDCl_3$ or chloroform-*d* = Deuterated chloroform

CO_2Me = Carboxymethyl

CT = Charge Transfer

DBDMF = 7-dibromo-9,9-dimethyl fluorene

DFT = Density functional theory

DMF = Dimethyl formamide

DPP-T = Diketopyrrolopyrrole-thiophene

E_g = Energy Bandgap

EPFL = École Polytechnique Fédérale de Lausanne

F4-TCNQ = Tetrafluorotetracyanoquinodimethane

FCA = 9-fluorenone-1-carboxylic acid

FMOs = Frontiers Molecular Orbitals

GLY = glycine

h = Hours

h^{-1} = per hour

HH = Head-to-head

HT = Head-to-tail

HOMO = Highest Occupied Molecular Orbital

I_2 = diiodine

IR = Infrared

k_R = Thermal relaxation rate constants

L = Lewis base

LD = Diffusion Length

LMOM = Laboratory of Macromolecular and Organic Materials

LP = lone pair of electrons

LUMO = Lowest Unoccupied Molecular Orbital

Me = Methyl

NMR = Nuclear Magnetic Resonance

nm = nanometers

NFAs = Non-fullerene acceptors

OFETs = Organic Field-Effect Transistors

OLEDs = Organic Light-Emitting Diodes

OMe = Methoxyl

OPVs = Organic Photovoltaics

OSCs = Organic Solar Cells

P3EHT = poly(3-hexylthiophene)

P3HT = poly(3-hexylthiophene)

PCE = Power Conversion Efficiency

PQT-12 = Poly[5,5'-bis(3-alkylthiophen-2-yl)-2,2'-bithiophene]

ppm = part per million

PSS = Photo-stationary state

PTS = Photochromic Torsional Switch

PyBOP = benzotriazol-1-yloxytripyrrolidinophosphonium hexafluorophosphate

RSS = Residual sum square

TFA = trifluoroacetic acid

THF = Tetrahydrofuran

THF-d_8 = Deuterated tetrahydrofuran

TT = Tail-to-tail

t = Relaxation time

$\tau_{1/2}$ = Half-life

UV = Ultraviolet

UV-Vis = Ultraviolet-visible

Table of Contents

1. Introduction 9
   1.1. State of Research 9
   1.2. n/p-Heterojunction Organic Solar cells 10
   1.3. n/p-Heterojunction Morphology 12
   1.4. Evolution of Organic Semiconductors 13
   1.5. Small Molecules Semiconductors 15
   1.6. Tailoring π-Conjugated Systems Through Synthetic Chemistry 17
   1.7. The Role of Intermolecular Interactions in Organic Electronics 18
   1.8. Tailoring π-Conjugated Systems Through Structural Distortion 18
   1.9. Intra-molecular Tuning and Supramolecular Control 20
   1.10 Aims and Objectives 21
2. Intramolecular Properties Tuning Through Azobenzene 22
   2.1. State of Research 22
   2.2. Results and Discussion 28
      2.2.1. Design of Azobenzene Compounds 28
      2.2.2. UV-vis Absorption Spectroscopy 29
      2.2.3. Photochemical Stability Testing 31
      2.2.4. Isomerization Yields 31
      2.2.5. Kinetics of Thermal Relaxation 33
      2.2.6. DFT Calculation 37
   2.3. Experimental Details 40
      2.3.1. Isomerization and PSS experiments for AB.Me, AB.OMe, AB.CO_2Me 40
      2.3.2. Absorption Spectra and Cyclability 47
      2.3.3. Thermal Relaxation Details 47
3. Supramolecular Interactions as a Control Mechanism in Organic Electronics 48
   3.1. State of Research 48
   3.2. Supramolecular Modification of P3EHT 51
      3.2.1. Regioregular Polymers: McCollough Reaction 53
      3.2.2. Results and Discussion 57
   3.3. Charge-Transfer Adduct in Bithiophene Derivatives 61
      3.3.1. Crystal Engineering 61
      3.3.2. Results and Discussion 64
      3.3.3. Experimental Details 86
4. Photochromic Torsional Switch 90
5. Conclusions 91
6. Synthetic Procedures and NMR Spectra 93
7. References 116

1. Introduction

1.1. State of Research

In the last 30 years organic semiconductors have played a crucial role in the advancement of cost-effective, flexible, and lightweight optical and electronic devices.[1,2] Organic semiconductors have been worldwide investigated as active materials in wide range of applications ranging from the field of material science and engineering to biology and medical technology.[3,4] In the recent years, some of these devices have reached a level of advancement to reach commercial distribution. Organic light-emitting diodes (OLEDs), for instance, are included in TV screen and automotive lighting.[5] On the other hand, optoelectronic devices such as organic photovoltaics (OPVs),[6] and organic field-effect transistors (OFETs),[7] Figure 1, while showing improvements in efficiency, stability, and scalability over the years, have not yet attained the required level of advancement for widespread commercial application. Continuous research efforts devoted to the design of new organic semiconductors, alongside the development of methods to precisely control the formation of organized assemblies at both the molecular and micrometer scales, are essential. A common approach to developing new organic semiconductors involves introducing functional groups or structural building blocks that adjust the electron distribution along the π-conjugation of a selected molecular architecture.[8] In contrast, control over molecular packing relies firstly on the introduction of solubilizing side chains, enabling good solubility during synthesis and purification.[9,10] Secondly, it involves a post-synthetic processability approach, utilizing solvent-based film deposition and thermal annealing.[11] In this context, the goal of the current work is to investigate new design towards light-responsive organic semiconductors, as well as to develop novel approaches to tune their molecular packing at the solid state, envisioning a potential application in organic solar cells (OSCs).



Figure 1. Examples of optoelectronic devices: OLEDs (a), organic solar cells (b), OFETs (c).

1.2. n/p-Heterojunction Organic Solar cells

The journey into organic semiconductors began in the early 20th century, but significant interest surged with the discovery of conductive polymers in the 1970s. This pivotal moment, marked by the awarding of the Nobel Prize in Chemistry in 2000 to Heeger, MacDiarmid, and Shirakawa, underscored the potential of conjugated polymers in conducting electricity.[12] Since then, advancements in molecular engineering and device architecture have propelled the field, leading to the development of several classes of devices. The development of organic photovoltaics has seen substantial advancements from 1976 to 2023. Originally, OPVs had power conversion efficiencies (PCE) below 1%, but strategic improvements in device architecture and the control of mixing and phase separation of semiconductor components increased PCEs to over 19% by 2023.[13,14] Such advancements have been achieved through meticulous research into the operational mechanisms underlying semiconductor materials.

Organic semiconductive materials have several advantages compared to their inorganic counterparts: i) easy modulation of the frontier orbitals energy levels *via* both molecular structural changes and thin-film morphology modification ii) the compatibility with low temperature/solution-based processing techniques, and iii) the ability to be integrated into flexible materials and substrates, allowing for devices with assorted form factors.[15,16] The significant advancements in organic solar cells stem from the ongoing development of new materials and fabrication technologies for devices, along with a profound understanding of film morphology, molecular arrangement, and device physics. In the last 20 year considerable attention has been drawn to organic solar cells with bulk n/p-heterojunction (BHJ) architecture, that is, an active layer with microphase-segregated domains of the electron donor and the acceptor component.[15,16,17,18,19] Such BHJ organic solar cells are commonly prepared by combining conjugated donor (D, p-type) polymers or macromolecules with electron-accepting (A, n-type) compounds (Figure 2).[15,16] First generation BHJ were commonly prepare by sandwiching the n-type and p-type layer, resulting in a planar D-A contact area.[15]

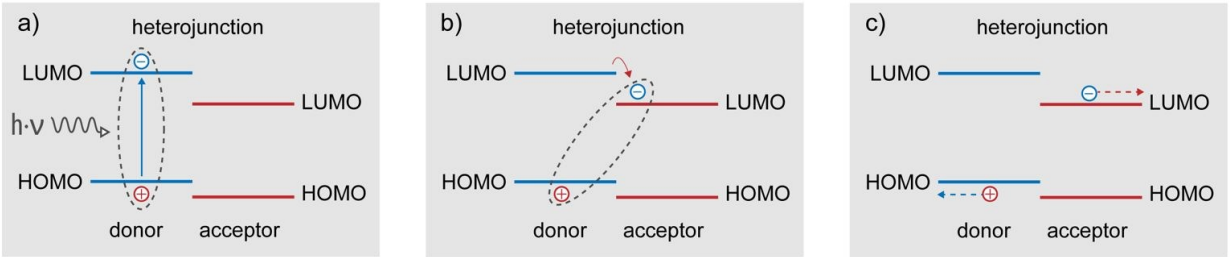


Figure 2. Schematic of the process of light absorption, exciton formation, and charge separation in bulk n/p-heterojunction solar cells.

Upon absorption of a photon in the electron donor material, with energy that is greater than or equal to its bandgap (E_g), an exciton forms, which can be regarded as an electron-hole pair bound together by electrostatic interactions. The exciton has to reach the electron acceptor material in order to split into an electron and a hole (charge carrier).[15,16] When the exciton reaches this interface, it becomes thermodynamically advantageous for the electron to transfer to the LUMO of the electron acceptor and for the hole to stay in the HOMO of the electron donor. From here, the electron-hole pair can follow one of two paths: i) the exciton binding energy may be overcome by a thermodynamic driving force, leading to spatially separated free charge carriers (referred to as the charge separated state), or ii) the electron and hole may recombine, reverting to a ground-state system without generating free charge carriers. Bearing this in mind, it is evident that to generate the maximum number of free charge carriers upon exposure to light, it is crucial to enhance the rates of charge transfer and reduce the rate of recombination.[15,16]

In light of this, various parameters must be considered for the design of an efficient semiconductor device. Due to the relatively high exciton binding energy in organic semiconductors (0.3–0.5 eV),[15,20,21] a significant driving force is required to separate the exciton into free charge carriers. Given that a substantial energetic driving force, provided by the energy offset at the D-A interface, is necessary to dissociate excitons into free charges, before they revert to the ground state. The maximum distance that an exciton can travel before this reversion is termed the exciton diffusion length (L_D). While there is some discussion regarding this specific distance, it is generally estimated that L_D in organic semiconductors ranges between 5 and 10 nm.[16,22,23] To bypass this limitation, the architecture of the D-A interface in BHJs has evolved into an interdigitating network so to maximize the n/p-type surface contact so as to maximize the exciton formation, and at the same time to guarantee a smooth percolation of the formed charge carrier towards the corresponding electrodes, Figure 3. This structure contrasts sharply with the planar interfaces of traditional bilayer cells and allows excitons – electron-hole pairs created by the absorption of light – to find an interface much more efficiently before they can relax back to their ground state. This efficient management of excitons is crucial because the exciton diffusion lengths in organic materials are typically very short, only about 10-20 nm.[15,16] Moreover, such an interdigitating D-A configuration has allowed for the thickening of the active layer without significantly increasing optical and electrical losses due to recombination and relaxation. This configuration enables the harvesting of a larger fraction of incident photons, significantly improving the photocurrents and overall device performance compared to earlier generations of solar cells. Early BHJ cells achieved power conversion efficiency (PCE) of around 3-5%, but through continuous improvements in the chemical design of donor and acceptor materials, efficiencies have now surpassed 19%.[15,24]

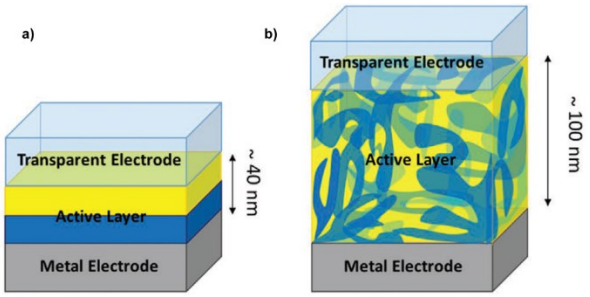


Figure 3. Schematic of bilayer (a) and bulk heterojunction organic solar cells (b).

1.3. n/p-Heterojunction Morphology

The meticulous selection of appropriate donor and acceptor materials is crucial in the development of new BHJ solar cells, focusing on both the optoelectronic and structural characteristics of each organic semiconductor. As previously mentioned, it is essential to consider the energy levels of the HOMO and LUMO for both donor and acceptor. Additionally, the bandgap (E_g) and absorption spectra of these materials should complement each other, allowing for the maximum utilization of the solar spectrum's incident photons. Managing phase separation is equally critical in BHJ solar cells, as it ensures the formation of an ideal interpenetrating network of donor and acceptor domains at the nanoscale.[16] Typically, this is influenced by the relative level of order and disorder at the D-A blend active layer. If in one side, the crystallinity of the donor and acceptor materials assists the formation of charger carrier, their percolation results restricted within a small domain. On the other hand, amorphous morphology resulting from poor molecular organization increase the possibility of charge recombination, but at the same time can act as bring to connect several crystallin domains so assisting the migration of the charges towards the corresponding electrodes.[16,25] There is a delicate balance required to maintain sufficient crystallinity and structural disorder, in each component to facilitate effective charge transport with minimal losses, while also preserving enough compatibility between the donor and acceptor to achieve nanoscale phase separation. This balance can be attained through several strategies: i) tailoring the miscibility of donor and acceptor materials with careful selection of side-chain solubilizing groups[26,27] ii) processing thermally the active layer,[28] and iii) using additives (solid or liquid) in the solution of organic semiconductors to undergo drying process.[29]

1.4. Evolution of Organic Semiconductors

The active layers of BHJ solar cells are composed of both donor and acceptor materials, intricately blended to form a network that facilitates efficient charge separation and transport.[15,16,30,31] Historically, the BHJ landscape was dominated by the use of fullerenes as the principal acceptors. These spherical carbon structures were favored for their ability to efficiently accept and transport electrons.[30,31] Concurrently, the most commonly used donor materials were polymers based on thiophene, such as polythiophene derivatives. These conjugated π-systems based on thiophene units represent a cornerstone in the domain of organic electronics, due to their exceptional ability to enable efficient charge transport and their inherent structural versatility.[30,32] Thiophene, a sulfur-containing heterocycle, constitutes the backbone of numerous high-performance organic semiconductors.

Among the plethora of thiophene-based polymers, the afore mentioned poly(3-hexylthiophene) (P3HT) stands out for its favorable optoelectronic properties, including a broad absorption spectrum in the visible region and high charge carrier mobility.[33,34] The regioregularity of P3HT, or the consistent orientation of thiophene units along the polymer chain, is crucial in achieving high levels of crystallinity and, consequently, efficient charge transport.[35] Furthermore, the alkyl side chains linked to the thiophene rings play a significant role in solubilizing the polymer and facilitating solution processing, a key advantage in the manufacture of printed electronic devices.[36] Another notable example of a thiophene-based polymer is polythiophene-co-benzodithiophene (PTB7), which has been utilized in high-efficiency bulk heterojunction solar cells.[37] The integration of benzodithiophene units into the polymer backbone extends the absorption into the near-infrared region, enhancing the photovoltaic performance by capturing a broader spectrum of solar radiation. Examples of thiophene-based polymers are illustrated in Figure 4.

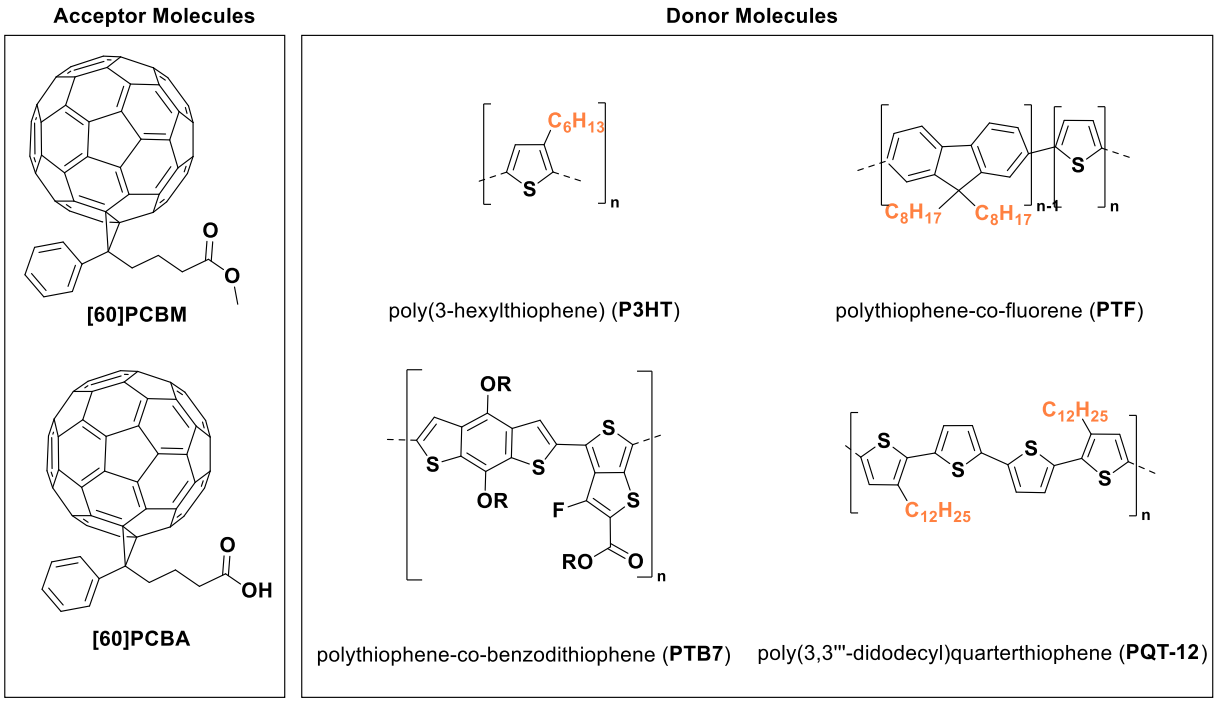


Figure 4. Fullerenes-derivatives acceptors [60]PCBM and [60]PCBA (on the left) and thiophene-based polymers donors (on the right). Solubilizing groups are depicted in orange.

Beyond poly(3-hexylthiophene) and polythiophene-co-benzodithiophene, several other thiophene-based polymers have been instrumental in pushing the boundaries of performance in organic electronics, Figure 4. Polythiophene-co-fluorene (PTF) is a copolymer that integrates fluorene units into the thiophene backbone, aiming to improve the polymer's optical properties and electronic stability.[38] The fluorene component contributes to widening the material's bandgap, making PTF suitable for blue-light-emitting diodes and high-voltage solar cells. Poly[5,5'-bis(3-alkylthiophen-2-yl)-2,2'-bithiophene] (PQT-12),[39] designed for high-performance OFETs, exhibits high charge carrier mobility due to its rigid backbone and effective π-π stacking. The alkyl side chains ensure solubility and facilitate solution processing.

Initially, the integration of fullerenes in bulk heterojunction cells was straightforward, but the use of thiophene-based polymer donors often required the addition of solubilizing side chains. These side chains were essential to enhance polymer solubility, yet they added complexity to the synthesis and affected the reproducibility of the manufacturing processes. Over time, however, the reliance on fullerenes started to decrease, especially around 2017, when the field of organic photovoltaics began embracing non-fullerene acceptors (NFAs). The first example reported of NFA was Y6 (Figure 5)[40] which offered high power conversion efficiencies that exceeded those of their fullerene-based predecessors.

Among the primary advantages of non-fullerenic acceptors over fullerene-based acceptors is the ability to readily adjust the energy levels of the frontier orbitals and improve molecular organization and compatibility with the donor material through thoughtful selection of the solubilizing chains. Furthermore, due to the straightforward customization of non-fullerene acceptor molecular architecture, these emerging acceptors have demonstrated compatibility with donor molecules of lower molecular weight, commonly known as 'small molecules'. This compatibility opened up new avenues for enhancing the efficiency and functionality of organic photovoltaics. These small molecules offer several advantages over traditional polymers, including ease of synthesis, batch-to-batch reproducibility, enhanced solubility, and precise control over molecular properties.[41]

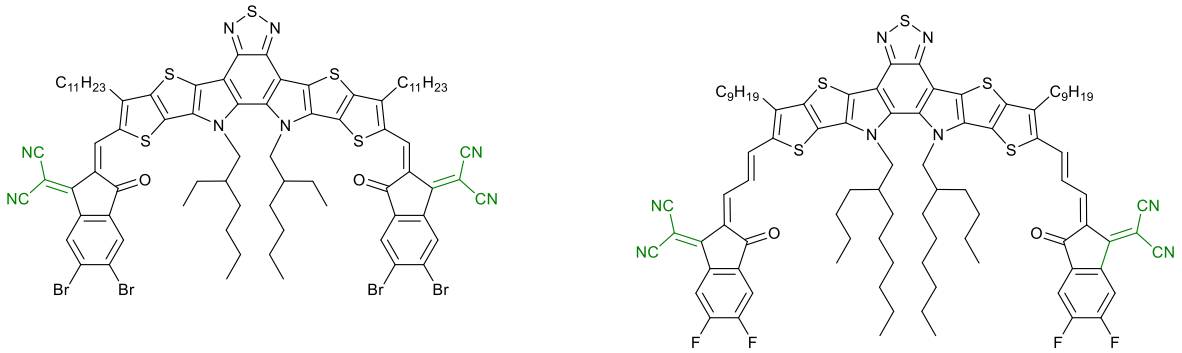


Figure 5. Non-fullerene acceptor examples.

1.5. Small Molecules Semiconductors

These small molecule donors typically feature a π-conjugated core (electron-rich, D, or electron-poor, A) flanked by π-conjugated lateral segments with electron-directing terminal groups, that play a pivotal role in the field of organic electronics (Figure 6). Their molecular architecture not only supports efficient light absorption and charge transport but also allows for the precise tuning of electronic properties through synthetic modifications.[42] Notably, small molecules can be synthesized to have well-defined chemical structures and exhibit high purity levels. Furthermore, their exceptional synthetic repeatability from batch to batch makes them more suitable for industrial-scale production through printing techniques.[42,43]

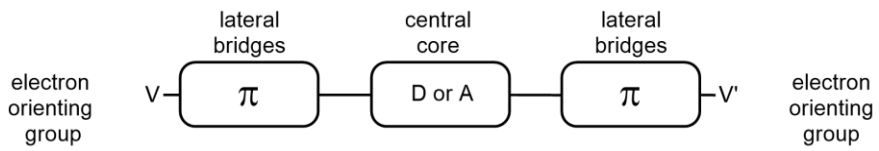


Figure 6. Small molecule molecular architecture.

To simultaneously meet all the aforementioned requirements, the structural components of organic semiconductors, including donor/acceptor units, π-conjugated bridges, alkyl side chains and/or pendant chains, and terminal electron orienting functionalities, must be carefully selected. Despite the design of these compounds being relatively straightforward to rationalize, their preparation often requires linear and multistep synthetic pathways. These pathways involve the serial insertion of various structural components, starting from the core. In the field of small molecules, thiophene units have been ingeniously incorporated into various structures to achieve desired optoelectronic characteristics, as reported in, Figure 7. Mention should be made to the benzodithiophene-thiophene co-oligomers, capable to extend the absorption spectrum and enhance charge transport properties.[44,45] Their design is tailored for OPV applications, where broad-spectrum absorption and efficient charge transport are fundamental. Among the various electron-orienting groups, it is worth mentioning the integration of electron-withdrawing groups such as dicyanovinyl and rhodanine. Small molecules used for solar cell applications feature a thiophene core in the center of the small molecule with two dicyanovinyl groups at the ends[46] (Figure 7). Improvements in charge transport performance in solar cell applications have been observed with the integration of rhodanine groups[47] into oligothiophene structures, as reported in Figure 7.

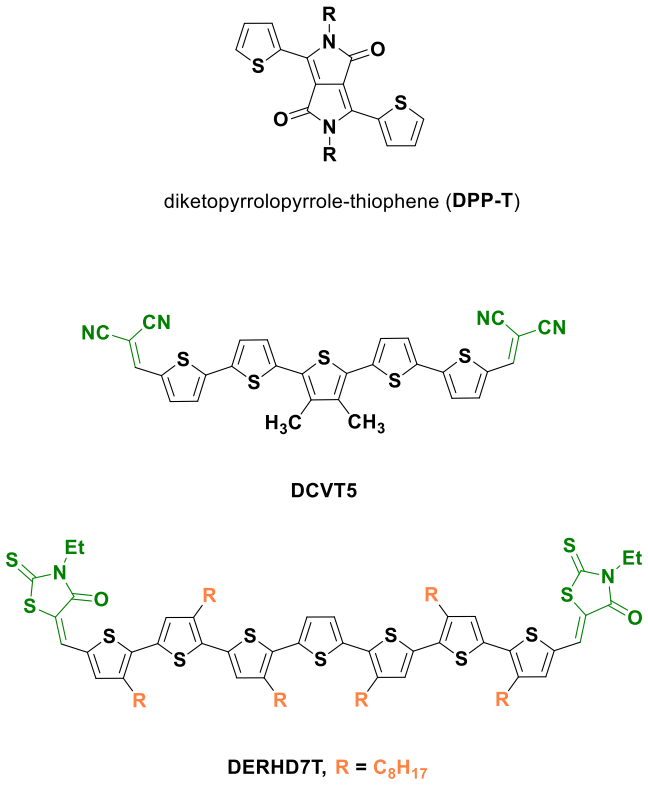


Figure 7. Thiophene-based small molecules donors. Electron directing groups are shown in green, while solubilizing chains are depicted in orange.

1.6. Tailoring π-Conjugated Systems Through Synthetic Chemistry

Organic semiconductors such as polymers, fused polyaromatic systems, and oligomeric 'small molecules', can be structurally tailored to modulate their optical and electronic properties. As previously mentioned, the introduction of specific functional groups into π-conjugated systems significantly alter the electron delocalization along the molecular structure so resulting into variation on frontier orbital band gap, energy levels, conductance thereby enhancing their performance in electronic devices. For example, the incorporation of electron-withdrawing groups, such as cyano (-CN) or nitro ($-NO_2$) groups, can lower the HOMO level, leading to materials with improved electron affinity and stability.[48,49] Conversely, electron-donating groups, like amino ($-NH_2$) or methoxy ($-OCH_3$), can raise the HOMO level, making materials more effective as hole transport.[50,51] Similarly, incorporation of electron rich or electron poor aromatic unit building block into the organic semiconductor architecture, allow for the adjustment of the frontier orbital band gap and energy levels. For instance, integrating electron-poor units into the π-conjugated backbone of an n-type semiconductor can dramatically lower its LUMO level. This adjustment transforms the resulting semiconductor into a more effective n-type material or electron acceptor in OPVs. On the other hand, the introduction of electron-enriched aromatic unit into a p-type semiconductor's structure can elevate its HOMO level, thereby improving air stability by diminishing its susceptibility to oxidation and facilitating hole injection and transport.[52] Beyond incorporating electron-orienting functionalities and aromatic units, the properties of semiconducting materials can be finely tuned by controlling their arrangement at both nano- and macro-meter scales when they are deposited as thin films.[53] Thus, introducing functionalities capable of regulating intermolecular interactions among molecules is essential for controlling the molecular organization of organic semiconductors. For instance, long alkyl chains have shown the ability to enhance solubility, processability, and allow for self-assembling of liner rod-like semiconductors like thiophene derivatives.[54] The strategic incorporation of functional groups through synthetic organic chemistry provides a powerful toolset for the design and optimization of materials for organic electronics.

1.7. The Role of Intermolecular Interactions in Organic Electronics

The spatial arrangement of organic semiconductors at solid state plays a critical role in governing the charge carriers (electrons and holes) percolation through the material. As we anticipated, the introduction of dedicated functional groups is a common strategy to reach this goal. Understanding the relationship between molecular structure and intermolecular interaction is the key to designing materials that meet specific application requirements.[15]

Intermolecular forces encompass π-π stacking, hydrogen bonding, van der Waals interactions, and halogen bonding, all of which play critical roles in dictating the crystallinity, molecular arrangement, and orientation in these materials. The π-π interactions between aromatic rings lead to the formation of well-ordered, stacked molecular arrangements. This stacking facilitates efficient charge carrier mobility by providing a pathway for electrons to move through the molecular assemblies.[55] Hydrogen bonds can direct the orientation of molecules relative to each other, leading to more predictable and desirable packing arrangements. While not as strong as covalent bonds, hydrogen bonds can significantly impact the material's mechanical and electronic properties.[56] Van der Waals forces, though weaker than hydrogen bonds, contribute to the overall stability of the molecular packing. They play a crucial role in the self-assembly of organic semiconductor molecules, influencing their solubility and processability. The use of halogen atoms can introduce specific directional interactions that can be exploited to control molecular organization further. Halogen bonds have been used to engineer specific packing motifs and enhance the crystallinity of organic semiconductor films.[57]

1.8. Tailoring π-Conjugated Systems Through Structural Distortion

In addition to incorporating dedicated electron-directing functional groups to fine-tune the optical and electronic properties of organic semiconductors, it is well-established that these properties are significantly influenced by the geometric conformation of the π-system. Consequently, varying the regioregularity or adjusting the steric interactions of lateral substituents are commonly employed strategies for customizing the physical properties of linear thiophene-based semiconductors.[58] The pronounced optical response resulting from twisting the π-system of this class of semiconductors has, for instance, found successful applications in ion and viscosity sensing.[59] Considering the widespread use of oligothiophene and polythiophene-based polymers as electron-donating materials in bulk heterojunction (BHJ) solar cells,[60] coupled with the potential to modulate their optical and electronic properties through conformational twisting, the Sforazzini laboratory has pioneered the development of a light-responsive building block capable of controlling the geometric conformation of the π-system.[61]

The developed molecular actuator is referred to as a 'Photochromic Torsional Switch' (PTS), illustrated in Figure 8. The PTS unit consists of a bithiophene core linked directly and *via* alkyl chain to a photosensitive actuator, azobenzene. The substitution at the *meta* position of azobenzene ensures that the molecular switch is oriented orthogonally relative to the bithiophene fragment, which is crucial to avoid cross-talk among the π -orbitals between the two components. The PTS unit can retain a twisted geometric conformation of the bithiophenic π-system when the azobenzene is in *trans*, while assume its corresponding planar form when the azobenzene in in its *cis* form. The inclusion of this light responsive PTS unit into thiophen-based oligomers and polymers can therefore allow for the dynamic and reversable tuning of their optical and electronic properties.[62]

As previously mentioned, one of the challenges in the field of organic electronics is the design of organic semiconductor materials that meet specific electrical and optical characteristics. With the broad application of OSCs, researchers face a new challenge: designing and synthesizing OSC materials with specific functions to meet the requirements of high-performance semiconductor devices. Our research group has chosen to tackle the topic by focusing on the application of building-integrated photovoltaics, specifically photovoltaic windows.[61] In the diverse field of organic electronics applications, photovoltaic windows emerge as a promising area. Currently, colorless organic solar cells utilized in these windows suffer from low efficiencies due to their absorption primarily in the ultraviolet (UV) and infrared (IR) regions. In contrast, high energy conversion efficiencies are linked with a broader absorption range that spans the UV-Visible spectrum, resulting in intense coloration. This poses a clear challenge: to develop organic solar cells that not only meet aesthetic and architectural demands but also maintain high energy efficiency.

PTS-based semiconductors have the dual capability to change color, thus meeting aesthetic requirements, and achieve high energy conversion yields. The optical activity of the resulting light responsive semiconductors can be fine-tuned to be conductive and colorful under light exposure and non-conductive and colorless in low lighting conditions.

For optoelectronic devices, light can be an optimal method for tuning the planarization of their conjugated system, as it can penetrate the device encapsulation without inducing reactions that would alter the composition of the conductive material.

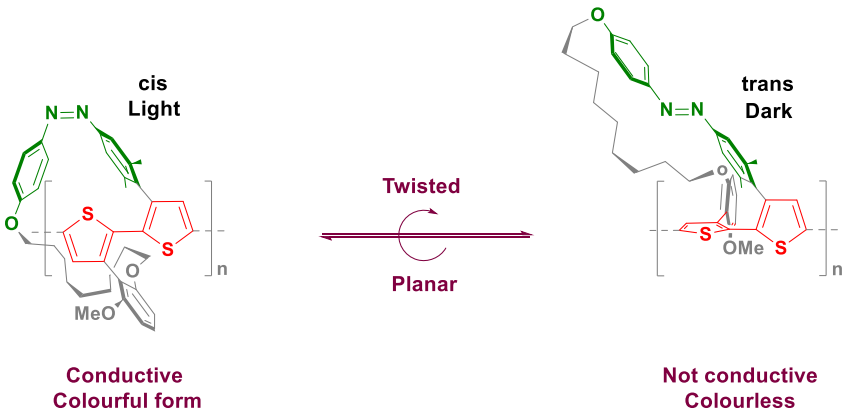


Figure 8. PTS unit. This architecture consists of a bithiophene segment (red) and a *meta*-substituting azobenzene (the light responsive switching unit, green) connected both directly and through an olefinic chain (linker).

With this approach, the conformational variation of the π-system will thus enable modulation of parameters such as material absorption and, consequently, cell efficiency. The materials can then shift between being transparent/colourless and non-conductive in low light conditions (distorted/interrupted conjugation) to more colourful and conductive when exposed to sunlight (planar conjugation). The first configuration ensures a clear view through the windows, while the second guarantees satisfactory efficiency of the photovoltaic device, thanks to panchromatic spectral absorption. As will be discuss in detail later on, with the vision to get an insight into the role of the azobenzene for the PTS unit, in the present thesis work, we investigated the effect of electron-orienting substituents in the *meta* position.

1.9. Intra-molecular Tuning and Supramolecular Control

In the present thesis work, efforts have been directed towards two possible approaches aimed at tuning the properties of the final organic semiconductor.

On one hand, the choice was made to investigate the insertion of intramolecular photosensitive units - specifically azobenzene - evaluating the structure-property relationships as the substituent groups vary. This exploration shed light on the dynamic capabilities of azobenzene to induce reversible changes in material properties through light stimulation, introducing a novel layer of functionality to semiconductor devices.

The second approach focused on the use of supramolecular interactions to control the solid-state packing interactions within thiophene-based materials. These non-covalent interactions, driven by the strategic placement of functional groups in the molecular architecture, play a crucial role in tailoring the material's properties for specific applications, such as optimizing the electrical properties and processability of the final material.

The findings of this thesis underscore the versatility and potential of thiophene-based compounds in the field of organic electronics.

1.10 Aims and Objectives

The principal aim of this thesis is to advance the understanding and development of organic semiconductors through two innovative approaches: the integration of intramolecular photosensitive units and the manipulation of supramolecular interactions. This research seeks to elucidate the underlying principles governing the optoelectronic properties of these materials and to explore their potential applications in organic electronics.

Specific objectives include:

1. Investigating the structure-property relationships in azobenzene-containing organic semiconductors, particularly how varying substituent groups influence the dynamic capabilities of azobenzene to induce reversible changes in material properties through light stimulation.
2. Exploring the use of supramolecular interactions to control solid-state packing interactions within thiophene-based materials, focusing on how the strategic placement of functional groups affects the electrical properties and processability of the final material.

By achieving these objectives, this thesis aims to significantly contribute to the field of organic electronics, providing a comprehensive theoretical and experimental framework to guide future research and innovation. The detailed examination of azobenzene as a molecular actuator, coupled with the insights into supramolecular interactions, provides a solid foundation for future research aimed at exploiting these mechanisms to create more efficient, adaptable, and sustainable electronic materials.

2. Intramolecular Properties Tuning Through Azobenzene

2.1. State of Research

Embedding photoswitchable moieties into organic semiconductor materials is poised to revolutionize the field of organic electronics, offering unprecedented control over material properties through light.[62,63] As research in this area progresses, driven by a deeper understanding of photoisomerization processes and innovative molecular engineering, the potential applications of these materials are set to expand, directing in a new era of functional, adaptive materials for a broad spectrum of technological applications.

Photochromic materials, capable of altering their color states under light exposure, are crucial in developing advanced technologies ranging from smart windows to data storage systems. Among the many families of photochromic materials, diarylethenes, spiropyrans, fulgides and azobenzenes (Figure 9) exhibit unique chemical characteristics and potential applications that are briefly and schematically summarized below.

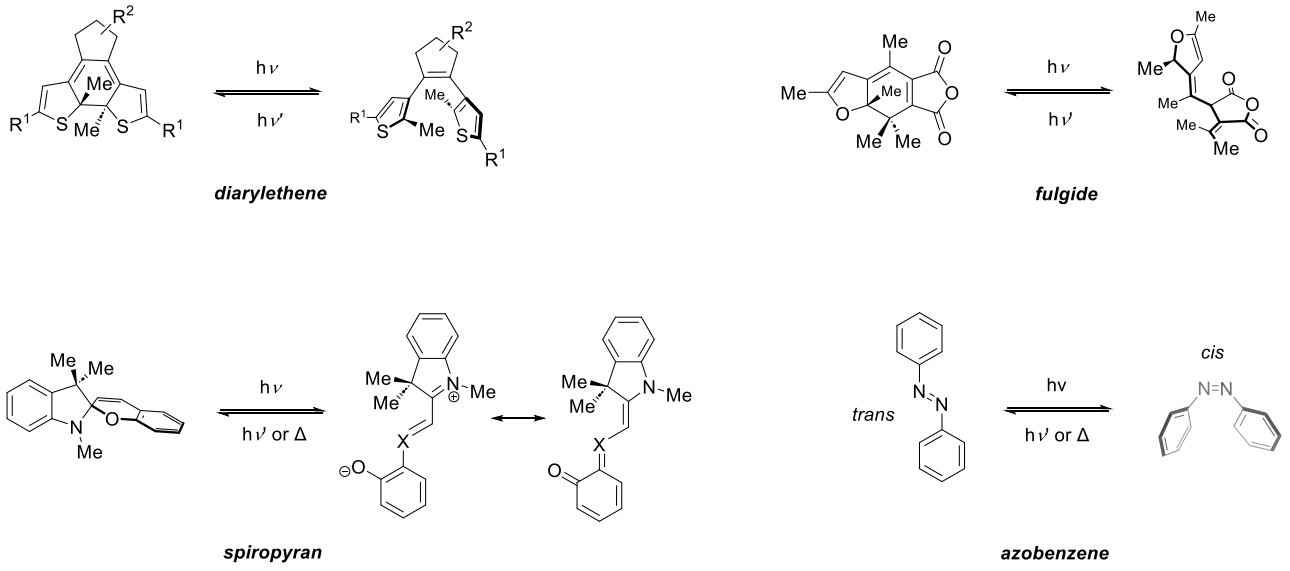


Figure 9. Examples of photochromic molecules: diarylethenes, fulgides, spiropyrans, and azobenzenes.

The unique photochromic behavior of diarylethenes is attributed to their structural transformation between open and closed forms. They are composed of two aromatic rings, typically thiophenes, furans or pyrroles, connected through a central ethene bridge that undergoes cycloaddition upon UV irradiation. A critical advantage of diarylethenes is their ability to maintain the colored or decolored state even in the absence of activating light, a property termed 'photochromic memory', which is pivotal for applications in optical switches and data storage devices.[64] The primary limitation,

however, is their often-complex synthesis, which can hinder large-scale production and application.[65] Spiropyrans are notable for their dramatic color change from colorless (closed form) to intense colors upon UV exposure. The mechanism involves the cleavage of a spiropyran ring to form a colored merocyanine form, which can revert to the original spiropyran upon visible light irradiation or heating. Drug delivery systems and chemo- and biosensing are just some of their versatile applications.[66] Unfortunately, spiropyrans are generally less photostable compared to other photochromic materials, which can limit their utility in outdoor applications.[67] Fulgides are characterized by their robustness and remarkable photo-stability, with the ability to undergo reversible isomerization between open and closed forms without significant degradation. This stability is crucial for applications where long-term durability is required, such as in optical memory devices.[68] Fulgides can be engineered to absorb specific wavelengths of light, making them versatile for multiplexed data storage solutions. The main challenge with fulgides lies in their relatively slower photo-response compared to other photochromic materials, which might be a limiting factor for applications requiring fast switching speeds.[69]

Since in this thesis, the focus has been placed on azobenzene as light-responsive unit, the following sections will detail its properties, applications and photoisomerization mechanism, aiming to prepare the reader for a comprehensive understanding of the purpose of this thesis work.

Azobenzene, a unique and versatile organic compound, has gained considerable attention in the scientific community for its remarkable photo-responsive properties.[70,71,72] Characterized by its distinctive azo group (-N=N-), azobenzene can undergo reversible *E/Z* isomerization upon exposure to light, a feature that renders it a highly effective molecular actuator. This photoisomerization, involving a transition from a more stable *E* (trans) form to a less stable *Z* (cis) form, is typically triggered by ultraviolet light, while thermal or visible light irradiation facilitates the reverse process. The profound implications of azobenzene's photoresponsive behavior span across various domains of research, encompassing chemistry, physics, materials science, biology, and pharmacology. Its ability to alter molecular conformation in response to light stimuli has led to innovative applications in the development of smart materials, molecular devices, and biological systems.[15,73,74,75]

To investigate the mechanisms underlying the light-responsive properties of azobenzenes, the photoisomerization processes will be examined in detail below. At the molecular level, azobenzene consists of two phenyl rings connected by an azo group (N=N). The fundamental mechanism of photoisomerization in azobenzenes involves the transition between two geometric isomers: the more stable *E* (trans) form and the less stable *Z* (cis) form. This transformation is initiated by the absorption of light, which induces an electronic transition in the molecule.[76] The photoisomerization process is

driven by specific electronic transitions, primarily the π-π^* and n-π^* transitions. These transitions are associated with the movement of electrons in the molecule and are critical in determining the absorption characteristics of azobenzenes. The π-π^* transitions involve the promotion of an electron from a bonding π molecular orbital (MO) to an unoccupied π^* MO localized on the N=N bond. In azobenzenes, the π-π^* transition typically manifests as an intense absorption band around 320 nm. This transition is central to the $E \rightarrow Z$ isomerization upon UV-light irradiation. The π-π^* band is highly sensitive to the nature and position of substituents on the phenyl rings, influencing the absorption properties and photoisomerization efficiency of azobenzene derivatives. The n-π^* transitions involve the excitation from the non-bonding orbital (n) of the N lone electron pairs to the empty π^* MO of the double bond N=N. This transition results in a weaker, broader absorption band typically centered around 450 nm. It is noteworthy that the n-π^* band is generally red-shifted relative to the π-π^* band, primarily due to the higher energy levels of n electrons compared to π electrons. The n-π^* transition plays a critical role in the reverse $Z \rightarrow E$ isomerization process, which can be induced by visible light irradiation. The *E/Z* isomerization of azobenzenes is a reversible process. While the conversion from the *E* to *Z* form is exclusively light-induced, the reverse *Z* to *E* transformation can occur either through thermal relaxation or photochemically. The efficiency and kinetics of these processes are greatly influenced by the electronic structure of the azobenzene molecule, particularly the energy levels and characteristics of the π-π^* and n-π^* transitions. The position and nature of these substituents can significantly influence the molecule's absorption spectrum. By attaching electron-donating or electron-withdrawing groups to the azobenzene structure, it is possible to alter the wavelengths required for effective *E/Z* isomerization, leading to shifts in the absorption bands.[76] These modifications ultimately change the photophysical behavior of the azobenzene molecule, impacting both the fundamental understanding of azobenzenes and their practical applications. A major limitation has been the tendency of small azobenzene-containing molecules to be photoactive primarily under UV light. This characteristic limits their range of applications due to UV light's low penetration depth in tissues and toxicity for biological applications.[77] Furthermore, UV light constitutes only a small portion of sunlight, thus posing an obstacle to some uses of such molecules for applications related to solar energy. Overcoming this challenge requires shifting the absorption of azobenzene-containing compounds towards the red spectrum. Moreover, significant attempts have been dedicated to minimizing the spectral overlap between the π-π^* and n-π^* transition bands, in order to fine-tune the switching processes *E/Z* and *Z/E*. Additionally, the study of thermal relaxation processes in azobenzenes is of paramount importance. Understanding the kinetics of the thermal $Z \rightarrow E$ isomerization offers valuable information about the stability of the isomers and the energy barriers

involved. This knowledge is crucial for designing azobenzene-based systems with desired lifetimes of the activated state, a key factor in applications requiring controlled and sustained response to light.

To fulfill these goals, thorough and detailed research has been conducted over the years,[70-72,78] focusing on the functionalization of azobenzenes at both the *ortho* and *para* positions in relation to the N=N group (Figure 10), providing insight into their structural and electronic effects, which in turn impacts the azobenzene's photochemical and photophysical properties.

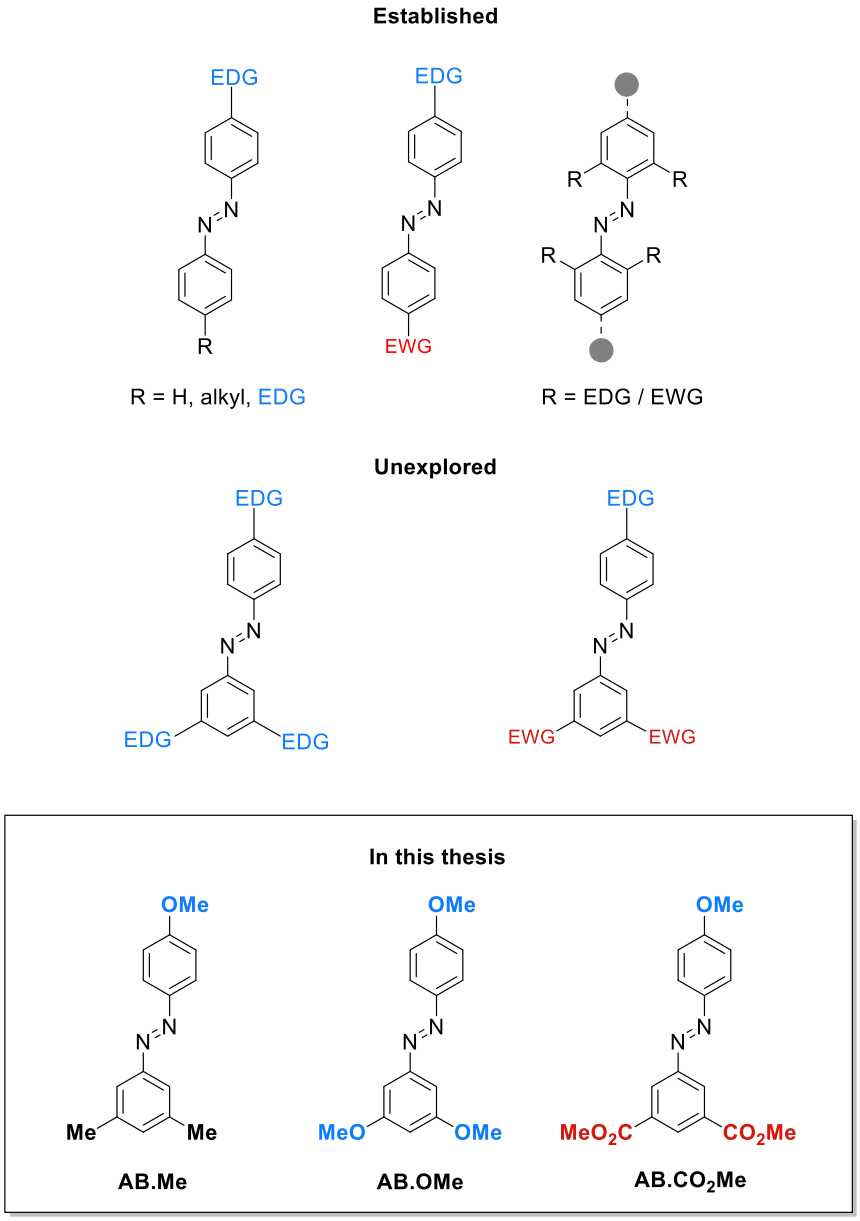


Figure 10. Schematic representation of functionalized azobenzenes. Functionalizations in either one or two *para* positions, functionalization in push-pull system, and functionalization in *ortho* positions (top half); functionalization in *meta* (bottom half); and the compound investigated in this work (framed).

During 1973 Rau meticulously categorized azobenzene derivatives into three distinct groups based on the effects of substitution patterns on their photophysical behavior.[79] The first group consists of unsubstituted azobenzene moieties, characterized by a clear distinction in the UV-vis spectra between the *trans* and *cis* isomers. Within this classification, the two absorption bands associated with the π–π^* and n–π^* transitions exhibit minimal overlap, resulting in a significant divergence in the UV–vis spectra of the *trans* and *cis* isomers. For the *trans* isomer, the pronounced π–π^* transition band appears at 310 nm, contrasted by a feeble n–π^* transition band at 440 nm. Conversely, for the *cis* isomer, the n–π^* transition becomes more pronounced. The second category of Rau's classification contains the so-called "amino-azobenzenes". Specifically, *para*-substituted azobenzenes (positions 4) with electron-donating groups (such as hydroxy, amino, etc.) induces a red-shift in the π–π^* absorption band (400–450 nm), while the n–π^* band remains unchanged. This leads to a convergence and partial overlap of the two bands. This type of functionalization is frequently employed to introduce a reactive site into azobenzenes for attaching solubilizing chains and linkers and has been successfully utilized in the development of photo-switchable surfactants[80] and photo-reactive monolayers on surfaces and nanoparticles[81]. The third category, "pseudostilbenes" includes azobenzenes substituted with electron-donor and electron-acceptor groups, leading to a substantial overlap of the transition bands. The incorporation of strong electron-withdrawing groups (like cyano and nitro) at the second *para* position of azobenzene (position 4') results in the formation of pseudo-stilbene-type azobenzenes, which exhibit overlapping π–π^* and n–π^* absorption bands within the visible spectrum. This diminishes the yield of the *E/Z* isomerization due to concurrent reverse *Z/E* isomerization triggered by the same wavelength. Pseudo-stilbene azobenzenes find applications in nonlinear optics[82] and light-responsive polymeric materials[83]. Functionalization at the *para* position also significantly impacts the half-life of *Z* isomers, reducing it drastically, typically to the order of seconds for azobenzenes substituted at position 4 and milliseconds for those substituted at positions 4,4'-azobenzenes, compared to the hours required for the original azobenzene configuration.

From the perspective of achieving the desired photoresponsive properties outlined earlier, researchers' efforts have turned towards the challenging functionalization at the *ortho* position to the N=N double bond. *Ortho*-substituted azobenzenes, especially those with electron-withdrawing or electron-donating groups placed at all four ortho positions, have emerged as significant compounds for controlling biomolecular structures through photoactivation. The steric hindrance and electronic effects introduced by *ortho* substitution have been shown to enhance the stability of the *Z* isomer, leading to prolonged thermal relaxation times.[84,85] These modifications allow for fine-tuning the azobenzene's absorption spectrum and photostability, making ortho-substituted derivatives particularly useful in biological applications where controlled activation and deactivation are crucial.

Meta-substituted azobenzenes have been explored to a lesser extent compared to their *para* and *ortho* counterparts. However, recent studies have revealed that substituents at the *meta* position can significantly affect the azobenzene's photophysical properties and thermal relaxation dynamics. The introduction of electron-directing groups at the *meta* positions has been shown to influence the absorption spectrum and enhance the stability of the *Z* isomer. This structural modification opens up new avenues for the design of azobenzene-based materials with tailored optical properties and thermal behaviors. Applications of *meta*-substituted azobenzenes include the development of light-responsive elastomers, molecular cages, and organic semiconductors.[86-87]

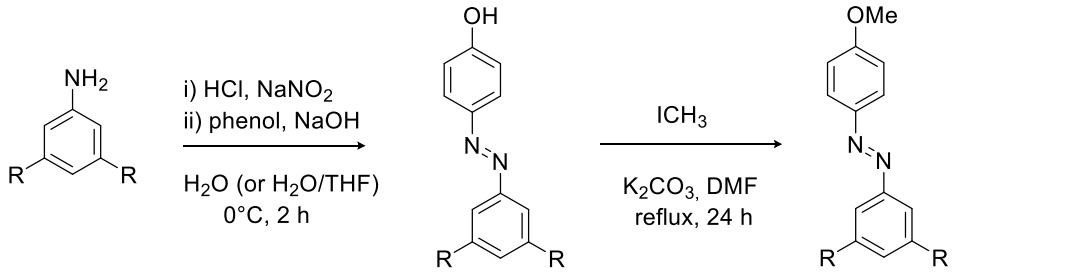
In the present work, we delve into the effects of the nature of substituent groups located in the *meta*-positions of the azobenzene molecule. Given the broad spectrum of interest in this class of molecules, this study's findings are not limited to theoretical understanding but extend to practical applications in the field of photoresponsive materials. As mentioned before, the light-induced molecular switch in the PTS unit is performed/realized through the incorporation of an azobenzene unit as the photoresponsive unit. In this regard, it is noteworthy that the placement of *meta*-groups in the azobenzenes examined in this study aligns with the molecular architecture of photo-torsional switch macromolecules (PTS). This comprehensive investigation involved three distinct types of substituents placed in the meta-positions of alkoxyl-azobenzenes. The compounds were analyzed spectroscopically to assess their photoswitching activity and thermal relaxation behavior. Moreover, a computational approach was employed to elucidate the energy levels of their *E* (*trans*) and *Z* (*cis*) isomers, which are crucial for understanding their photoresponsive behavior**.**

2.2. Results and Discussion

2.2.1. Design of Azobenzene Compounds

Aimed to investigate the structure-property relationship of azobenzene, we chose to incorporate two methoxy groups as electron-donating functionalities, two carbonyl groups as electron-donating functionalities and two methyl groups as bulky, non-electron-donating reference compounds.

Three different azobenzenes have been synthetized by two-step synthetic route. Starting from commercial *meta* di-substituted amino benzenes (**Ph.NH$_2$.Me**, **Ph.NH$_2$.OMe**, **Ph.NH$_2$.CO$_2$Me**), the first step involves the reaction of diazonium salt of amino benzenes with phenol resulting in the production of the corresponding *meta* di-substituted hydroxyl azobenzenes (**AB-OH.Me**, **AB-OH.OMe**, **AB-OH.CO$_2$Me**). The second step consists in the functionalization of the hydroxyl group by a nucleophilic reaction between the phenyl fragment and an alkyl halide (iodomethane) to obtain the desired compounds **AB.Me**, **AB.OMe**, **AB.CO$_2$Me**. Since various applications require the insertion of solubilizing and linker groups to link polymers and biomolecules in subsequent reactions, we decided to alkylate the hydroxyl group in anticipation of future potential applications.



Ph-NH$_2$.Me, R=Me — **AB-OH.Me, R=Me,** 36% — **AB.Me, R=Me,** 83%
Ph-NH$_2$.OMe, R=OMe — **AB-OH.OMe, R=OMe,** 46% — **AB.OMe, R=OMe,** 55%
Ph-NH$_2$.CO$_2$Me, R=CO$_2$Me — **AB-OH.CO$_2$Me, R=CO$_2$Me,** 68% — **AB.CO$_2$Me, R=CO$_2$Me,** 32%

Scheme 1. Synthetic pathway used for *meta*-substituted azobenzenes.

2.2.2. UV-vis Absorption Spectroscopy

In an effort to characterize the synthesised azobenzenes, UV-Vis absorption spectroscopy experiments were conducted to reveal the characteristic peaks of the *E* and *Z* forms. A characteristic trend can be observed in the absorption spectrum of *m*-methylated azobenzene in its *E*-form, showing two separate bands. Regarding the reference compound **AB.Me**, we observe a first pronounced peak around 350 nm, derived from π-π* excitation, and a weaker band centered at 444 nm, corresponding to the *n*-π* transition (Figure 11). Since the value measured for the first two bands are in good agreement with those reported in literature for alkoxylazobenzens[80,88-89], so highlighting that the alkylation on *meta* position has proven to have a negligible effect on the absorption spectra features. Moreover, the π-π* high energy transition - resulting from molecular orbitals located mainly on aromatic rings - is associated with an additional higher energy band around 237 nm. Modest changes in all three bands occur with the replacement of the two methyl units with two electron-donor methoxy groups. Actually, the **AB.OMe** compound shows a λmax at 353 nm resulting from the π-π* transition and a signal at 440 nm for the *n*-π* counterpart. Unlike the previous case, however, the peak correlated with the high-energy π-π* transition is shifted towards blue, overlapping with the solvent cut-off area and resulting in an undefined band. Overall, the introduction of electron donating functionalities at the *meta* position of the azobenzenes induces limited spectral variations, suggesting that the electronic delocalization on the molecules remains largely unaffected. Conversely, incorporating two carbonyl groups, which serve as electron-withdrawing entities at the meta positions, markedly alters the spectral characteristics of azobenzene. The incorporation induces a bathochromic shift of approximately 8 nm in the low-energy π-π* transition band of **AB.CO$_2$Me**, culminating in a maximum absorption wavelength (λ_{max}) of 358 nm. Furthermore, this modification results in a red-shift of approximately 14 nm in the high-energy π-π* transition, located at 251 nm. Relative to **AB.Me**, the *n*-π* transition signal displays a hypsochromic shift of approximately 7 nm. The advantage conferred by the spectral band shift, attributable to the substituent's nature, lies in the enhanced utility of the high-energy excitation band for facilitating *Z*→*E* isomerization in scenarios where the *n*-π* transition band is not easily accessible. The significant redshift observed in the π-π* band effectively mitigates its spectral overlap with the absorption spectra of solvents commonly employed in sample preparation, thereby improving accessibility to this band. This shift not only optimizes the photoisomerization process but also expands the versatility of azobenzenes for various applications by enabling more precise control over their photoresponsive behavior.

To investigate the *Z*-isomer counterparts, the *E*-isomers of the azobenzenes were subjected to irradiation at 365 nm (see Experimental Section for more details). The absorption spectrum characteristic of the *Z* conformation is depicted in Figure 1, illustrating an increase in the *n*-π* band alongside a decrement in the π-π* band's intensity, which varies according to the substituent involved. Specifically, the spectral signatures of azobenzenes in their *Z* conformation show an intensity reduction of the π-π* band amounts to approximately 87% for AB.Me, 83% for AB.OMe, and 79% for **AB.CO$_2$Me**. In the context of the π-π* band, the *Z*-isomer of **AB.CO$_2$Me** exhibits a discernible bathochromic shift of approximately 21 nm relative to both **AB.Me** and **AB.OMe**. This observation underscores a critical insight: electron-withdrawing groups positioned at the meta location predominantly influence the electronic transitions of the *Z*-isomer, while their impact on the E-isomer's transitions remains minimal. Upon exposure to light at 450 nm, the *Z*-form azobenzenes of **AB.Me**, **AB.OMe**, and **AB.CO$_2$Me** revert to their respective *E*-forms through retroisomerization. This light-mediated mechanism facilitates a recovery of approximately ∽75%, ∽85%, and ∽60% of the initial absorption intensity of the *trans* isomer for **AB.Me**, **AB.OMe**, and **AB.CO$_2$Me**, respectively. This sequence culminates in a photo-stationary state (PSS), as delineated in Figure 11.

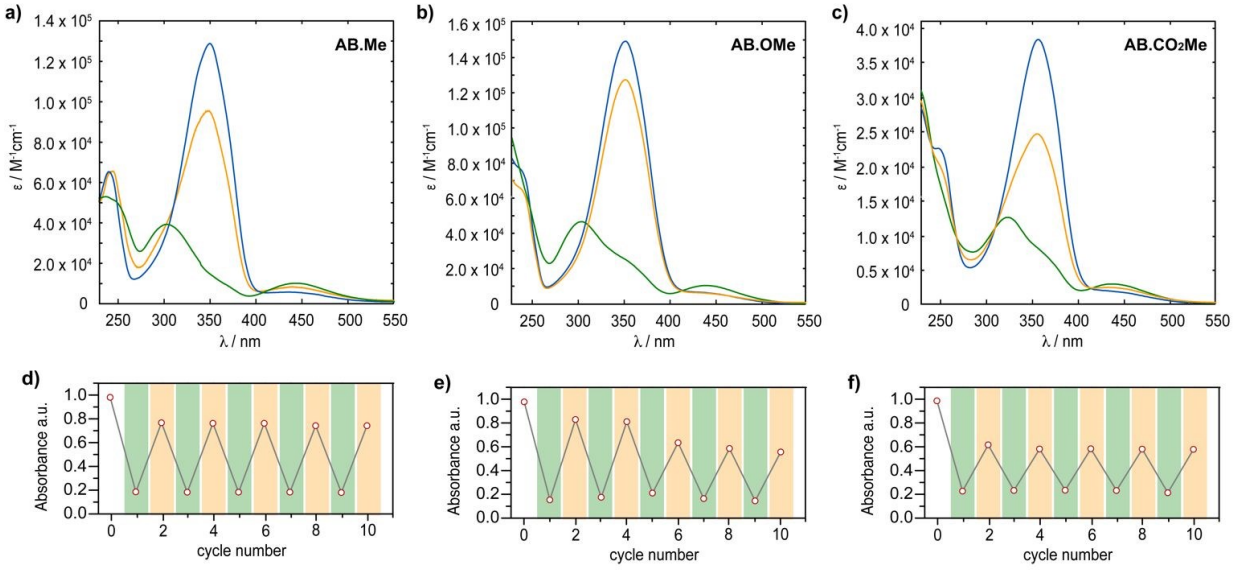


Figure 11. Absorption spectra of **AB.Me** (a), **AB.OMe** (b), and **AB.CO$_2$Me** (c) in tetrahydrofuran (THF) solution; *E* isomer (blue), *Z* isomer (green), and photostationary state PPS450 nm (orange). Measured absorbance at λ_{max} for **AB.Me** (d), **AB.OMe** (e), and **AB.CO$_2$Me** (f) in THF solutions by alternately irradiating the sample at λ = 365 nm (green) and λ = 450 nm (orange) in repeated switching cycles.

2.2.3. Photochemical Stability Testing

The compounds underwent alternating irradiation cycles at wavelengths of 365 nm and 450 nm to assess potential degradation under these conditions, as illustrated in Figure 11. The photoisomerization process between the two isomers did not result in noticeable degradation for the compounds **AB.Me** and **AB.CO$_2$Me**, indicating that the incorporation of electron-withdrawing groups at the *meta* position does not detract from the structural integrity of the azobenzene framework. However, when **AB.OMe** was exposed to alternating cycles of irradiation, a progressive decline in the absorption intensities of both *E* and *Z* isomers was observed, suggesting a gradual photodegradation linked to the light-induced isomerization process.

2.2.4. Isomerization Yields

The quantitative analysis of the *E* and *Z* isomers of azobenzenes, following photoexcitation at wavelengths of 365 nm and 450 nm, was meticulously carried out using nuclear magnetic resonance (NMR) spectroscopy, comparing the effect on photoexcitation results induced by two different solvents (THF-d_8 and chloroform-*d*). This advanced spectroscopic technique provided a clear distinction between the spectral signatures of pristine *E* isomers and their *Z* counterparts. Specifically, a detailed examination of the ^{1}H-NMR spectra for **AB.OMe** and **AB.CO$_2$Me**, in comparison to the reference molecule **AB.Me**, elucidated a pronounced shift in the aromatic proton peaks within the meta-substituted benzene rings, as depicted in Figure 10 and 11. Expanded spectra of photoexcitation results are shown in Experimental Section.

Regarding the THF-d_8 spectra (Figure 12), in the reference compound **AB.Me**, the protons of the dimethylphenyl moiety are positioned at 7.50 and 7.09 ppm, respectively. Upon substituting the methyl group with the electron-donating, the protons experience a shielding effect, resulting in a downfield shift to 7.07 and 6.57 ppm. Conversely, the introduction of carbonyl functionalities in place of the methyl group induces a deshielding effect, shifting the proton peaks to a lower magnetic field at 8.69 and 8.67 ppm. Upon irradiation at 365 nm, all the compounds adopt their respective Z forms. The ^{1}H-NMR spectral profiles reveal the positions of protons in **AB.Me** at 6.75 and 6.40 ppm, in **AB.OMe** at 6.23 and 5.94 ppm, and in **AB.CO$_2$Me** at 8.38 and 7.64 ppm. Upon comparing the ^{1}H-NMR signal intensities of the *E* and *Z* isomers, we determined that photoisomerization of **AB.Me** occurs with a yield of 93%, while **AB.OMe** and **AB.CO$_2$Me** exhibit yields of 90% and 89%, respectively.

Irradiation at 450 nm facilitates the generation of the initial *E* isomer, ultimately attaining a PSS with yields of 51%, 49%, and 51% for **AB.Me**, **AB.OMe**, and **AB.CO$_2$Me**, respectively.

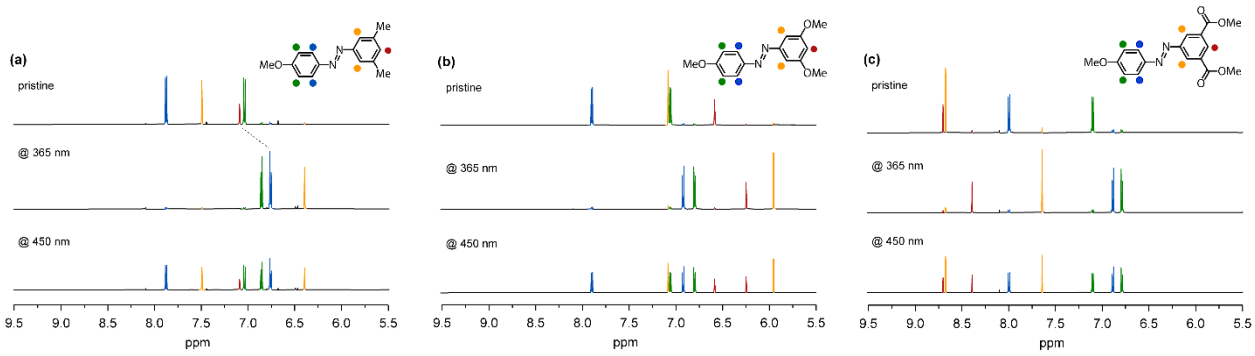


Figure 12. Aromatic region of the ^{1}H-NMR spectrum of compound **AB.Me** (a), **AB.OMe** (b), **AB.CO$_2$Me** (c) in THF-d_8. Pristine (top spectrum), after irradiation at 365 nm (middle spectrum), and after irradiation at 450 nm (bottom spectrum).

Regarding the use of $CDCl_3$ (Figure 13), in the case of **AB.Me**, the dimethylphenyl moiety's protons are located at 7.50 and 7.09 ppm. Substitution with electron-donating groups led to a shielding effect, manifesting as a downfield shift to 7.09 and 6.57 ppm for **AB.OMe**. Conversely, the incorporation of carbonyl functionalities in **AB.CO$_2$Me** resulted in a deshielding effect, with proton peaks shifting to a lower magnetic field at 8.75 and 8.70 ppm. Upon irradiation at 365 nm to induce *E* to *Z* isomerization, analogous shifts were observed for the *Z* forms, confirming the consistency of the spectral trends. The proton positions for **AB.Me** in the *Z*-form were found at 6.79 and 6.46 ppm, for **AB.OMe** at 6.26 and 6.00 ppm, and for **AB.CO$_2$Me** at 8.48 and 7.68 ppm, attributable to the respective shielding or deshielding effects.

The efficiency of photoisomerization was rigorously quantified by analyzing the ^{1}H-NMR signal intensities for both *E* and *Z* forms. Irradiation at 365 nm resulted in conversion yields of 90% for **AB.Me**, 88% for **AB.OMe**, and 79% for **AB.CO$_2$Me** from their *E* to *Z* isomers. Subsequent exposure to 450 nm light facilitated the reverse process, achieving a photo-stationary state (PSS) with *E*-form regeneration yields of 41% for **AB.Me.*E***, 34% for **AB.OMe.*E***, and 37% for **AB.CO$_2$Me.*E***, respectively. As a result, under photo-stationary state (PSS) conditions, 59% of **AB.Me.*Z***, 66% of **AB.OMe.*Z***, and 63% of **AB.CO$_2$Me.*Z*** are observed.

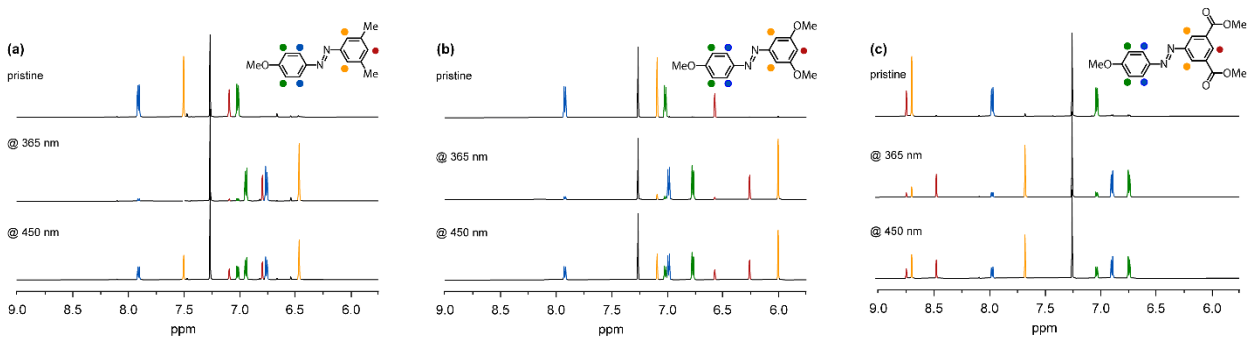


Figure 13. Aromatic region of the ^{1}H-NMR spectrum of compound **AB.Me** (a), **AB.OMe** (b), **AB.CO$_2$Me** (c) in chloroform-d. Pristine (top spectrum), after irradiation at 365 nm (middle spectrum), and after irradiation at 450 nm (bottom spectrum).

2.2.5. Kinetics of Thermal Relaxation

As anticipated, the metastable *Z* isomer of the three compounds can spontaneously revert to the their *E* form by thermal relaxation (Figure 14a-c). The kinetics of *Z*-to-*E* isomerization process was investigated through UV-Vis spectroscopy to evaluate the capability of the substituted EWG or EDG to influence the thermal relaxation process of the reference compound **AB.Me**. Kinetic curves were plotted by following the maximum absorbance of light, $A(t)$, - at 350 nm for **AB.Me**, 353 nm for **AB.OMe** and 357 nm for **AB.CO$_2$Me** - during thermal relaxation from the *Z* form to the *E* one (Figure 14).

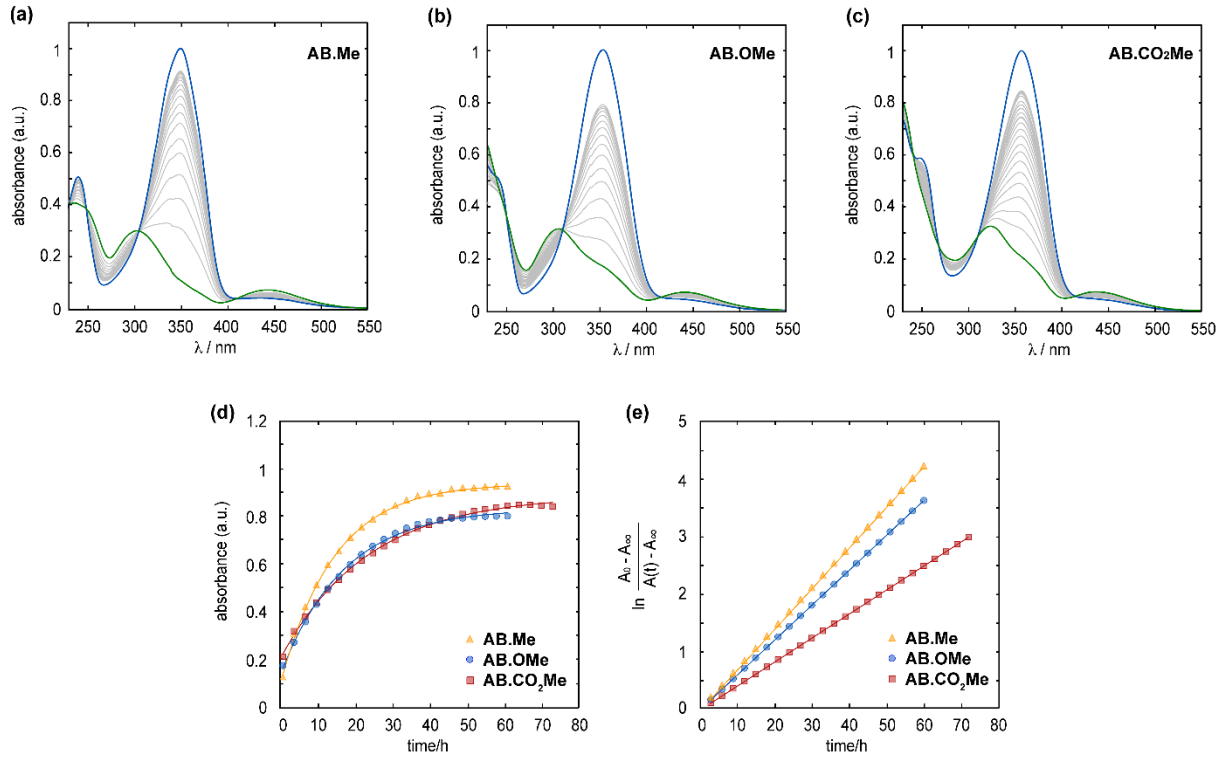


Figure 14. Measured absorption spectra for the Z to E thermal relaxation of **AB.Me** (a), **AB.OMe** (b), and **AB.CO₂Me** (c) in diluted THF solutions at 25°C. Measured absorbance at λ_{max} for **AB.Me** (yellow triangle), **AB.OMe** (blue circle), and **AB.CO₂Me** (red square) in THF solutions over time; a logaritmic fit (d), and a linear fit was used to estimate relaxation rate constants (e).

The experimental data shown were normalized to the asymptotic absorbance value (*E* isomer) for each of the three datasets.

As can be seen from Figure 14d, the trends of thermal relaxation are similar, growing to the asymptotic value fairly smoothly. All the *meta*-substituted azobenzenes reach a certain asymptotic value of absorbance, depending on the nature of the substituent groups. Experimental evidence suggests that complete back isomerization is achieved faster for donating substituted **AB.Me** and **AB.OMe** (approximately 1.8 days), while an additional day is required for **AB.CO₂Me** (totalling 2.7 days).

Experimental data points were analyzed through two mathematical fitting (logistic and logarithmic type) in order to evaluate some crucial parameters governing the kinetics processes, such as half-life and thermal relaxation rate constants. In the following, the parameters estimated from the interpolation performed will be commented on in detail.

Half-life ($\tau_{1/2}$) was calculated by logistic fit, while the logarithmic fit was applied to estimate the thermal relaxation rate constants (k_R). Further details on mathematical modeling are reported in the following sections. At a temperature of 25°C, the half-life for the *Z*-to-*E* isomerization was approximately 9.5 hours for **AB.CO₂Me** and 8.5 hours for **AB.OMe** and

AB.Me. Kinetics analysis of the *Z* to *E* back isomerisation reveals a trend in the thermal relaxation rate constants, which precisely follow the order **AB.Me** > **AB.OMe** > **AB.CO₂Me** with thermal relaxation rate constants 7.0 × 10^{-2} h^{-1}, 5.9 × 10^{-2} h^{-1} and 4.3 × 10^{-2} h^{-1}, respectively (Figure 14e).

A plausible explanation for this phenomenon can be attributed to the enhanced stability of the *Z* isomer conferred by the electron-directing groups. This increased stability is primarily ascribed to the electronic effects of the electron-directing functionality, as opposed to the bulkiness of the group, which would otherwise promote the destabilization of the Z isomers. This scenario is especially pronounced with the carbonyl group, being the largest functionality among the three, yet exhibiting a slower thermal relaxation rate. Recent literature on azobenzenes suggests that the thermal isomerization mechanism involves both singlet and triplet electronic states, engaging in inversion and rotation processes.[90,91] Notably, the rotation mechanism through triplet states has been recognized as the predominant.

The two mathematical models differ regarding the type of equation and the parameters involved. In the following sections, a detailed discussion of the models involved will be presented.

The logistic model consist in a sigmoidal curve – logistic type[92], which equation is:

$$A(t) = \frac{A_\infty}{1+e^{-k_R(t-\tau_{1/2})}} \quad (1)$$

where *t* is the relaxation time, A_∞ is the maximum absorbance amplitude; $\tau_{1/2}$ is the time at which half of the maximum amplitude is reached - the half-life time; k_R is the coefficient of logistic growth rate – the back *Z* to *E* relaxation constant.

The model parameters are summarized in Table 1.

Table 1. Thermal relaxation parameters and fitting results – Logistic Model.

Compound	Parameter	Value	St. Error	Fitting Results	Value
AB.Me	A_∞	0.90419	0.01065	**R^2**	0.98225
	$\tau_{1/2}$	8.41098 h	0.47022	**RSS**	0.01682
	k_R	0.13805 h^{-1}	0.0098		
AB.OMe	A_∞	0.79548	0.00533	**R^2**	0.99491
	$\tau_{1/2}$	8.60355 h	0.2737	**RSS**	0.00339
	k_R	0.11813 h^{-1}	0.0044		
AB.CO₂Me	A_∞	0.8449	0.00707	**R^2**	0.99184
	$\tau_{1/2}$	9.45788 h	0.41801	**RSS**	0.00624
	k_R	0.08169 h^{-1}	0.00356		

The back isomerization *Z* to *E* trend can be also rationalized through a logarithmic model[93], which equation is:

$$\ln \frac{A_0 - A_\infty}{A(t) - A_\infty} = k_R^* t \quad (2)$$

where A_0, $A(t)$, A_∞^* are the *Z* form absorbances corresponding to the time 0, t and photostationary state respectively; *t* is the relaxation time and k_R^* is the rate constant of the *Z/E* relaxation.

Expressing Eq. 2 in relation to the absorbance value we obtain:

$$A(t) = A_\infty^* + \frac{A_0 - A_\infty}{e^{k_R^* t}} \quad (3)$$

As can be seen from the Figure 14, the logarithmic curve (dashed lines) overlaps nicely with the experimental points, allowing an accurate estimation of the model quantities A_∞^*, A_0 and k_R^*.

The model parameters are summarized in Table 2.

Table 2. Thermal relaxation parameters and fitting results – Logarithmic Model.

Compound	Parameter	Value	St. Error	Fitting Results	Value
AB.Me	A_∞^*	0.93734	0.00317	**R^2**	0.9992
	A_0	0.13132	0.00517	**RSS**	0.00076
	k_R^*	0.07002 h^{-1}	0.00112		
AB.OMe	A_∞^*	0.8322	0.00526	**R^2**	0.99794
	A_0	0.159	0.00673	**RSS**	0.00137
	k_R^*	0.05901 h^{-1}	0.00165		
AB.CO_2Me	A_∞^*	0.88657	0.00477	**R^2**	0.99856
	A_0	0.21938	0.00501	**RSS**	0.00084
	k_R^*	0.04294 h^{-1}	0.00099		

Concerning the fitting performances, some considerations can be made.

The coefficient of determination, R^2, for the three datasets, is quite high, suggesting that the two models explain the mainly variability of the responses data around its mean. Finally, the residual sum of square (RSS) shows – in all three fitting runs – a value close to zero, thus indicating that the datasets are reasonably well represented by the chosen kinetic model.

2.2.6. DFT Calculation

To gain insight into the stability of the *E* and *Z* isomers, we analyzed their frontier HOMO and LUMO orbitals resulting from first-principles calculations based on density functional theory (DFT). The results for the *E* and *Z* conformations are summarized in Figure 15. All states have a π-character spread over the phenyl groups, with minor or no contributions on the attached groups, regardless their electron attractive/withdrawing character. The structural folding in *Z* configurations put the aromatic rings closer, promoting an enhanced π-overlap between them. The LUMO states of are hardly affected by the different functionalization for all the geometries. On the other hand, HOMO states are more sensitive to the position of attached group and isomerization. In particular, the HOMO state for *E* configuration of **AB.OMe** differs from the other orbitals shown in Figure 15a for both symmetry and for the contribution of the attached methoxy groups. The methyl and the carbonyl terminations do not contribute to the HOMO states of the corresponding molecules. These characteristics of the **AB.OMe** HOMO state change in the *Z* configurations, where both the symmetry and the methoxy contribution results more similar to other azobenzenes. The overall similarities of the frontier orbitals concur with the orbital-transition analysis deduced from the absorption spectra. The different electron donor/acceptor character of the attached groups changes the overall polarization of the molecules. The specific dipolar interaction affects the energy position of the frontier orbitals and, therefore, the different energy transitions (i.e. peak energy) detected in the optical spectra. As shown in Figure 15c, **AB.Me** and **AB.OMe** have very similar orbital energy distributions. The electron withdrawing character of **AB.CO$_2$Me** accumulates charge in one part of the molecule increasing the internal dipole. The effect is a down-shift of frontiers orbitals (for both *E* and *Z* configuration) of ~30 meV. This agrees with the stability analysis described above.

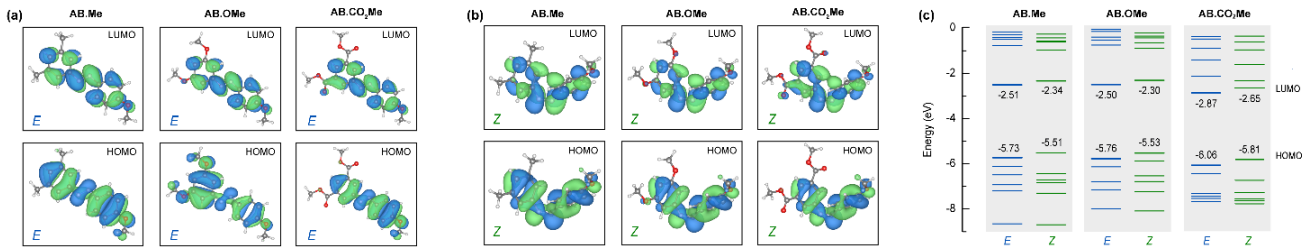


Figure 15. Calculated molecular orbitals HOMO and LUMO for all the *E* (a) and *Z* (b) isomers studied in this work; and corresponding energy levels (c).

Computational analysis has been carried out by using first principles simulations based on density functional theory (DFT), as implemented in the QuantumEspresso suite. A van der Waals corrected functional (vdw-df2-b86r) is used to optimize the geometry of the systems in the E and Z conformations, while a hybrid functional (HSE06) is used describe the electronic structure of the resulting optimized geometries. Atomic coordinates were relaxed until all force components were smaller than 0.03 eV/Å. Ultrasoft pseudopotentials of the Vanderbilt type are used to describe the electron-ion interaction for each chemical species. Single particle wavefunctions (charges) are expanded in planewaves up to an energy cutoff of 30 Ry (300 Ry), respectively. Isolated molecules are simulated in cubic cells of 30.0 Å of size, which include a sufficient vacuum space to avoid spurious interactions among replica. The Brillouin zone of the reciprocal lattice was sampled at the Γ point.

Ground state of all azobenzene-derived molecules have been evaluated through a total-energy-and-forces minimization procedure. The final total energies of *E* isomers are always lower (i.e. more stable configuration) than the Z ones. The numerical values are summarized in Table 3 (unfunctionalized pristine azobenzene was included for comparison) .

Table 3. Total energy of azobenzene derivatives in *E* and *Z* configurations.

Compound	Isomer *E*	Isomer *Z*
AB	-188.1780003244 Ry	-188.1396345584 Ry
AB.Me	-261.4194234596 Ry	-261.3791013955 Ry
AB.OMe	-325.1457693207 Ry	-325.1055627704 Ry
AB.CO_2.Me	-411.7971856261 Ry	-411.7572072099 Ry

The electronic structures of the optimized molecules have been evaluated at the hybrid HSE level of theory. The results are summarized in Figure 16, which displays the total density of states (DOS), and in Table 4 which collects the energy bandgap and the energy of the HOMO and LUMO energy.

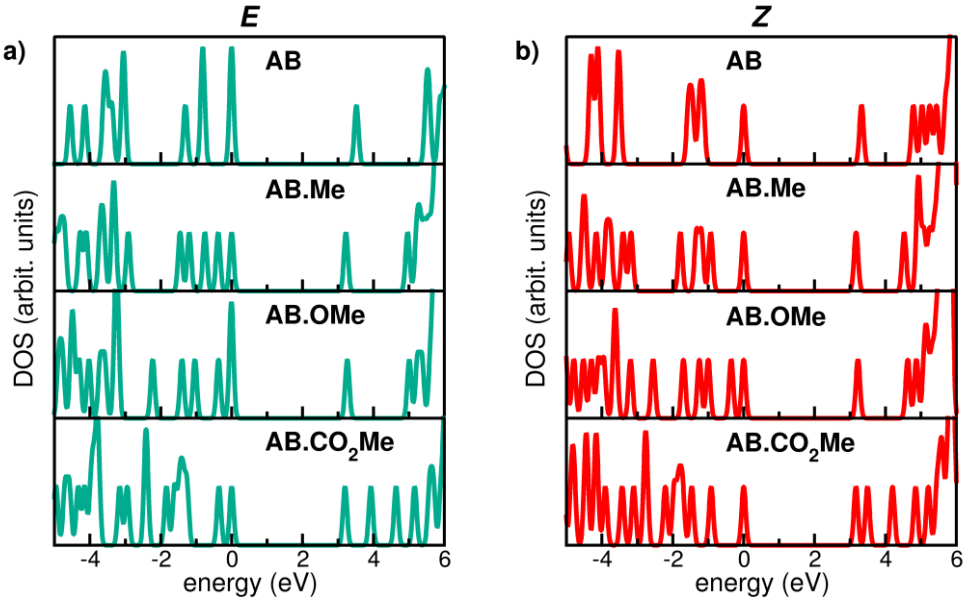


Figure 16. Density of states (DOS) of azobenzene derivatives in *E* (a) and *Z* (b) configuration. Zero energy reference is set to HOMO state of each system.

Table 4. Bandgap (Eg) and energy level of HOMO and LUMO states of azobenze derivatives in *E* (a) and *Z* (b) configuration. Zero energy reference is set to the vacuum level.

Compound	Isomer *E*			Isomer *Z*		
	E_g	HOMO	LUMO	E_g	HOMO	LUMO
AB	3.52 eV	-6.33 eV	-2.81 eV	3.33 eV	-5.89 eV	-2.57 eV
AB.Me	3.22 eV	-5.73 eV	-2.51 eV	3.17 eV	-5.51 eV	-2.34 eV
AB.OMe	3.26 eV	-5.76 eV	-2.50 eV	3.22 eV	-5.53 eV	-2.30 eV
AB.CO2.Me	3.20 eV	-6.06 eV	-2.87 eV	3.17 eV	-5.81 eV	-2.65 eV

2.3. Experimental Details

2.3.1. Isomerization and PSS experiments for AB.Me, AB.OMe, AB.CO_2Me

Isomerization experiments from *E* to *Z* were performed on Compound **AB.Me**, **AB.OMe** and **AB.CO_2Me** and PSS conditions were determined through ^{1}H-NMR spectroscopy. Samples of **AB.Me**, **AB.OMe** and **AB.CO_2Me** were prepared with the same quantity (0.00415 mmol) of product in $CDCl_3$ and THF-d8. Samples were irradiated at 25°C with 365 nm wavelength for t_{365nm} to promote the *Z* form of compounds and ^{1}H-NMR spectra acquired. Then, the samples were irradiated at 25 °C at 450 nm for t_{450nm} to investigate the PSS conditions and ^{1}H-NMR spectra acquired. Comparison between the *E* form (first spectrum), the *Z* form (second spectrum) and PSS (third spectrum) are shown below in Figure 17-22. The lamp power used to irradiate at 365 nm is 6 W and the NMR tube was placed at a distance of ~4 cm from the lamp. The lamp used at 450 nm is 1 mW cm^{-2} and the NMR tube was placed at a distance of ~4 cm.

Table 5. Irradiation time and sample concentration for **AB.Me**, **AB.OMe** and **AB.CO_2Me.**

Compound	t_{365nm} [min]	t_{450nm}[min]	Solvent
AB.Me	5	225	$CDCl_3$
AB.OMe	50	200	
AB.CO_2Me	60	60	
AB.Me	40	170	THF-d_8
AB.OMe	40	170	
AB.CO_2Me	40	170	

2.3.1.1. ^{1}H NMR spectra of *E/Z* isomerization and PSS of AB.Me

^{1}H-NMR ($CDCl_3$) spectroscopy shows that when **AB.Me.*E*** is exposed to 365 nm light, ~90% of **AB.Me.*E*** is converted to **AB.Me.*Z***. By irradiating at 450 nm, the inverted process occurs obtaining ~41% of **AB.Me.*E*** and ~59% of **AB.Me.*Z***.

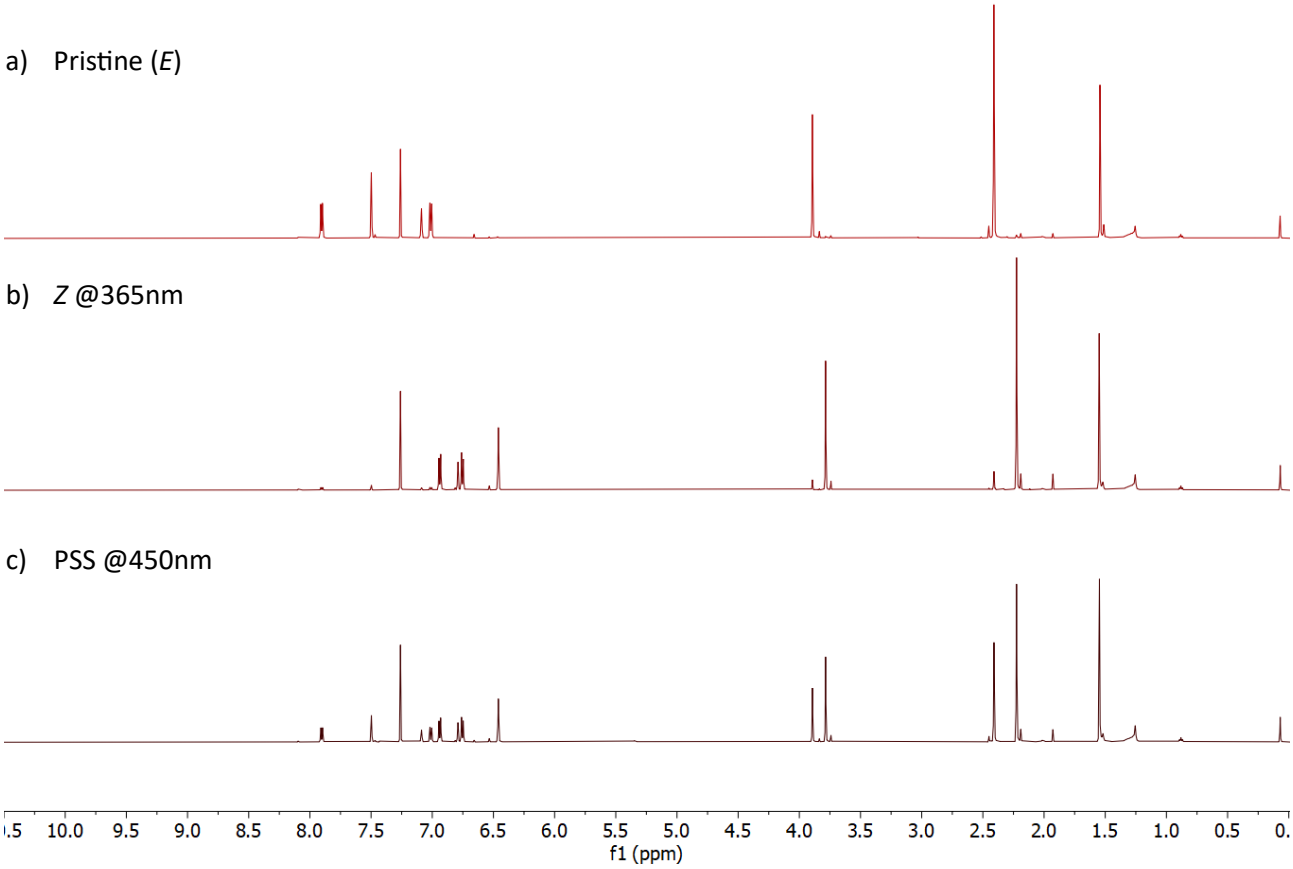


Figure 17. *E* form (a), *Z* form (b) and PSS state (c) for **AB.Me** ($CDCl_3$).

^{1}H-NMR (THF-d_8) spectroscopy shows that when **AB.Me.*E*** is exposed to 365 nm light, ~93% of **AB.Me.*E*** is converted to **AB.Me.*Z***. By irradiating at 450 nm, the inverted process occurs obtaining ~51% of **AB.Me.*E*** and ~49% of **AB.Me.*Z***.

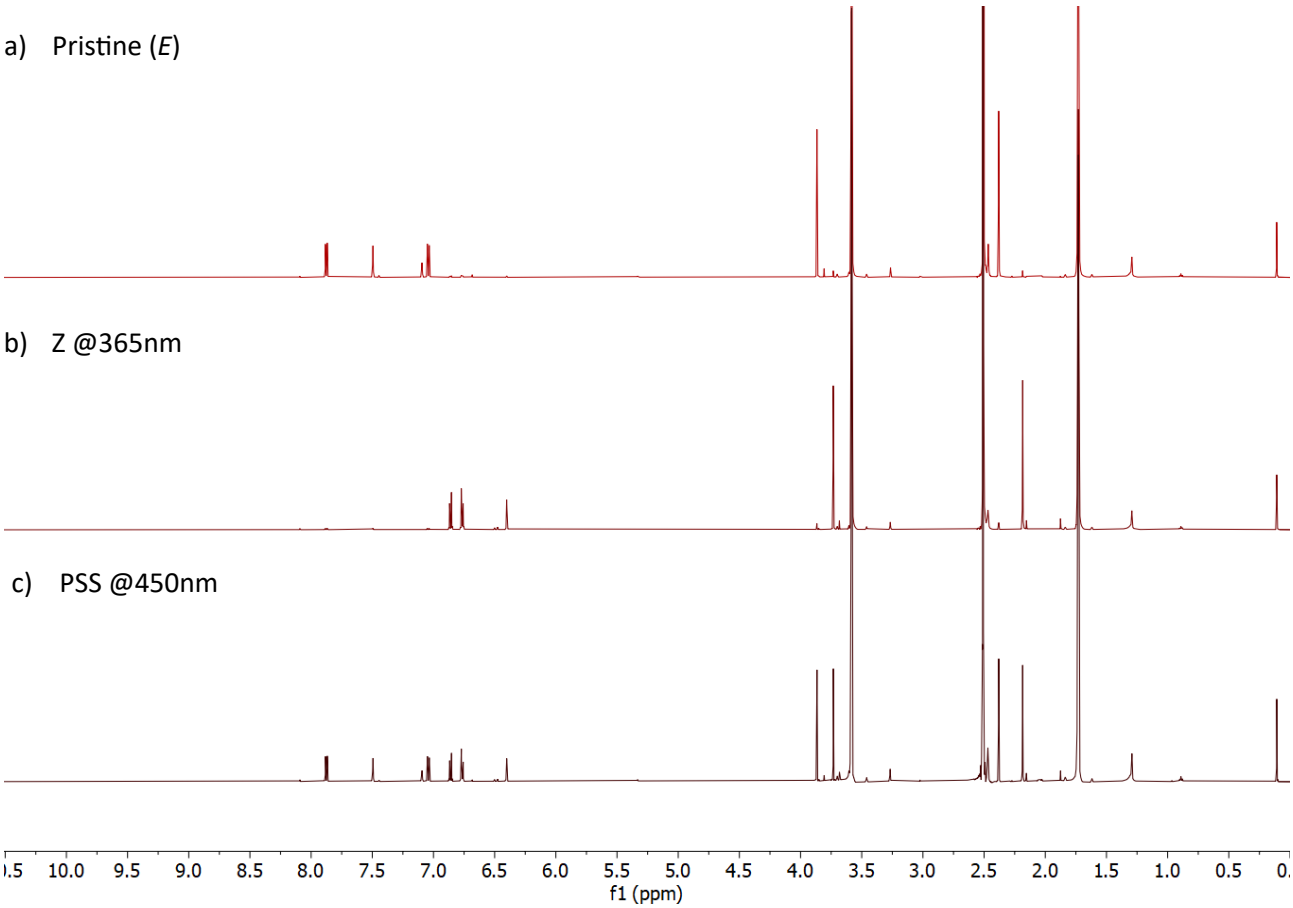


Figure 18. E form (a), Z form (b) and PSS state (c) for AB.Me (THF-d_8).

2.3.1.2. ^{1}H NMR spectra of *E/Z* isomerization and PSS of AB.OMe

^{1}H-NMR ($CDCl_3$) spectroscopy shows that when **AB.OMe.*E*** is exposed to 365 nm light, ~88% of **AB.OMe.*E*** is converted to **AB.OMe.*Z***. By irradiating at 450 nm, the inverted process occurs obtaining ~34% of **AB.OMe.*E*** and ~66% of **AB.OMe.*Z***.

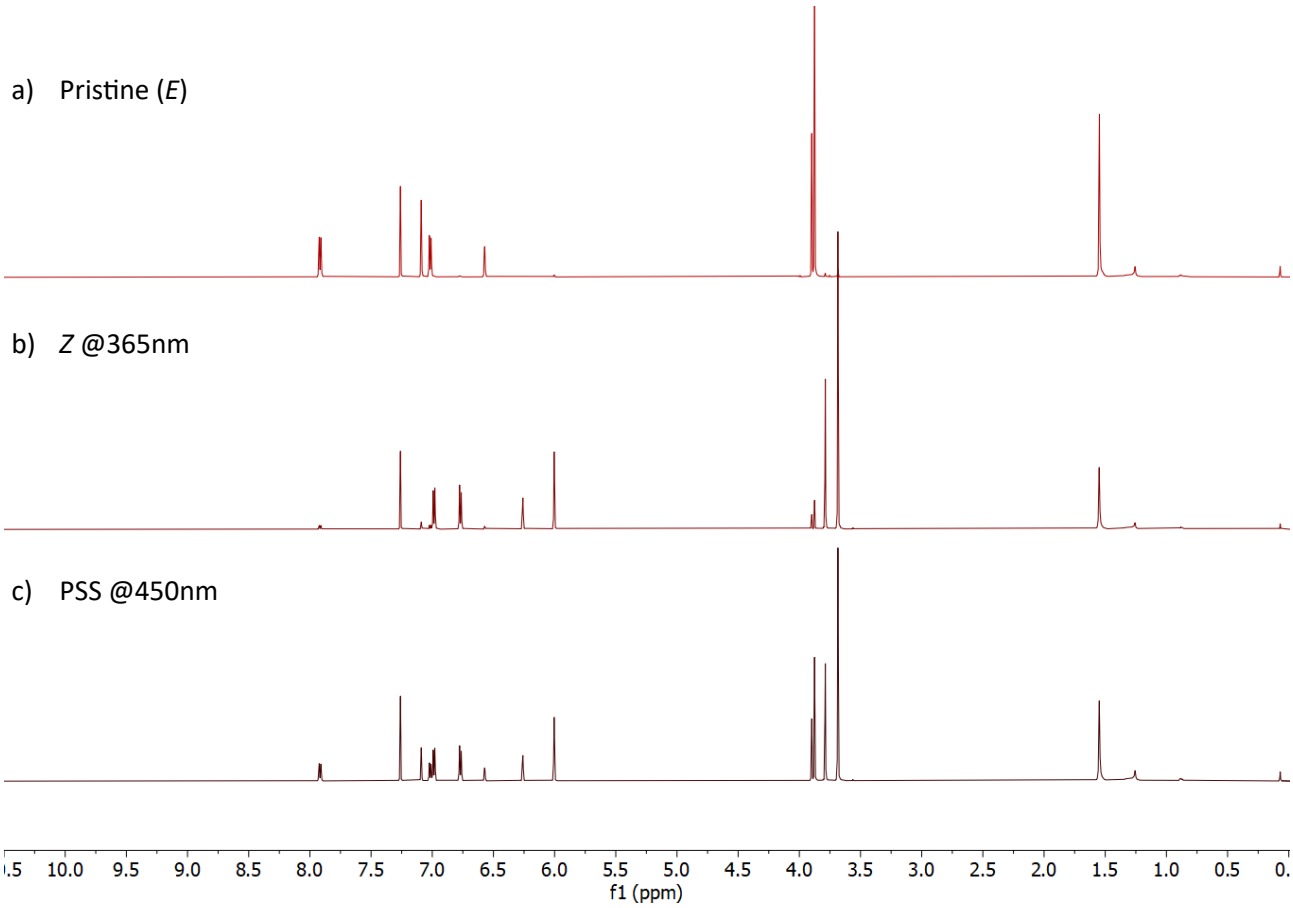


Figure 19. *E* form (a), *Z* form (b) and PSS state (c) for **AB.OMe** ($CDCl_3$).

^{1}H-NMR (THF-d_8) spectroscopy shows that when **AB.OMe.*E*** is exposed to 365 nm light, ~90% of **AB.OMe.*E*** is converted to **AB.OMe.*Z***. By irradiating at 450 nm, the inverted process occurs obtaining ~49% of **AB.OMe.*E*** and ~51% of **AB.OMe.*Z***.

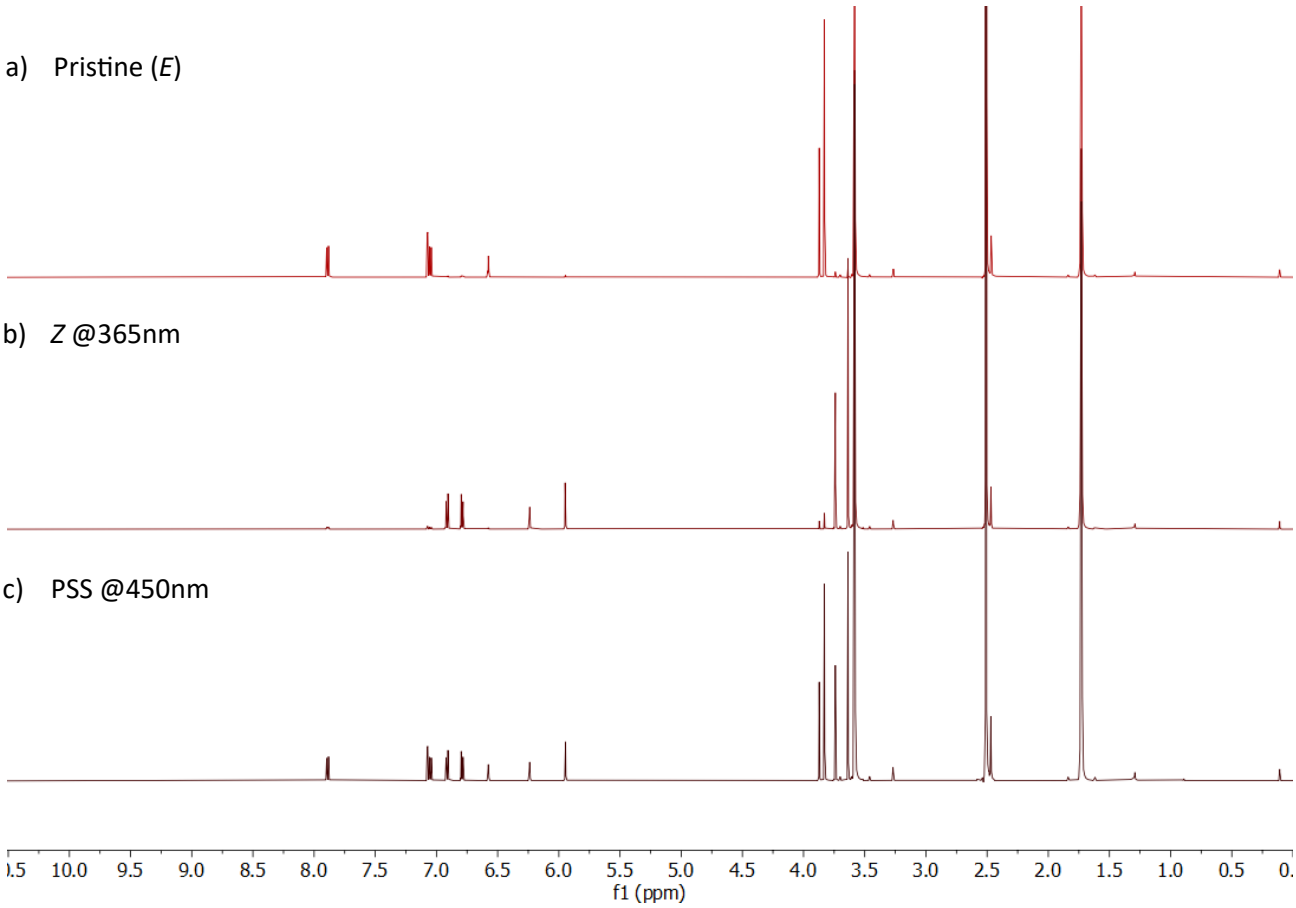


Figure 20. E form (a), Z orm (b) and PSS state (c) for AB.OMe (THF-d_8).

2.3.1.3. ^{1}H NMR spectra of *E/Z* isomerization and PSS of AB.CO$_2$Me

^{1}H-NMR ($CDCl_3$) spectroscopy shows that when **AB.CO$_2$Me.*E*** is exposed to 365 nm light, ~79% of **AB.CO$_2$Me.*E*** is converted to **AB.CO$_2$Me.*Z***. By irradiating at 450 nm, the inverted process occurs obtaining ~37% of **AB.CO$_2$Me.*E*** and ~63% of **AB.CO$_2$Me.*Z***.

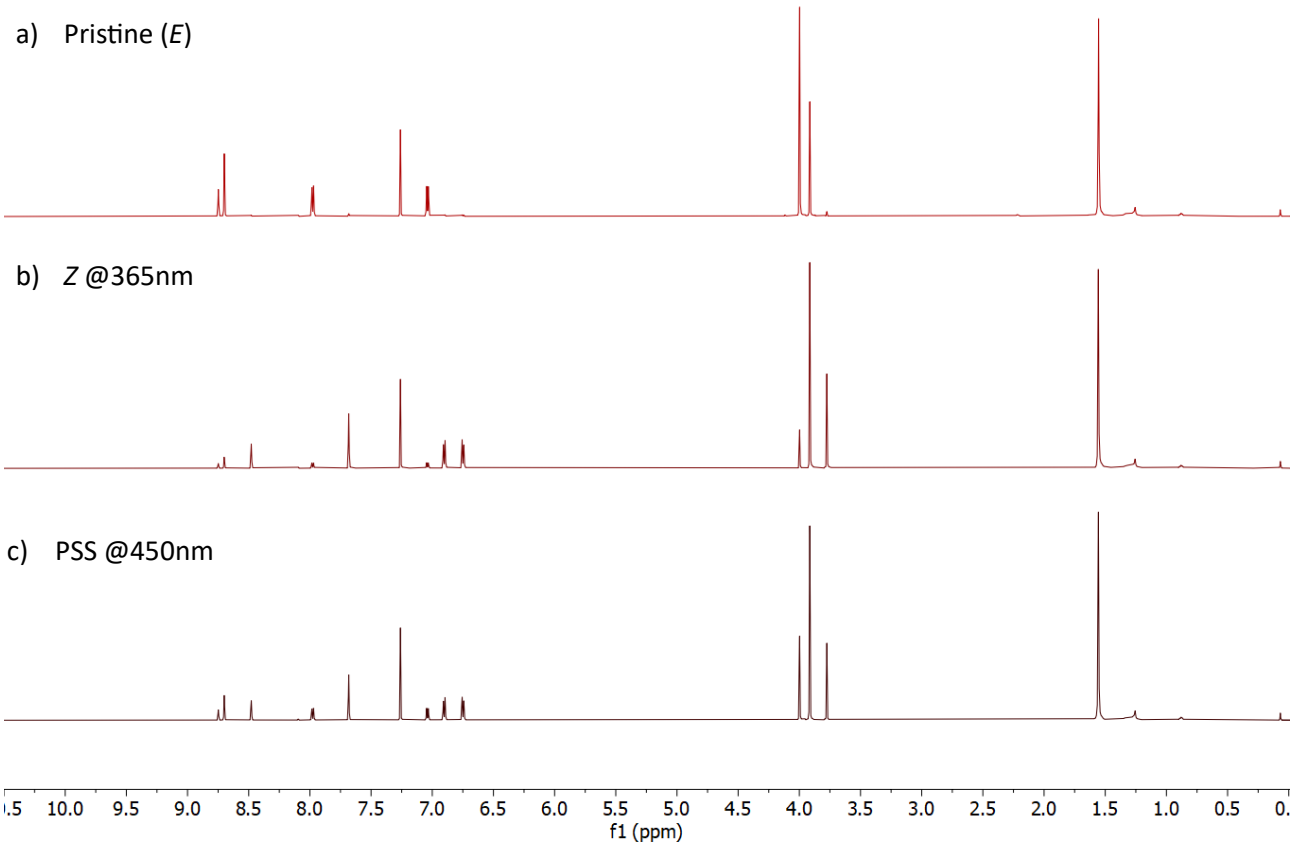


Figure 21. *E* form (a), *Z* form (b) and PSS state (c) for **AB.CO$_2$Me** ($CDCl_3$).

^{1}H-NMR (THF-d_8) spectroscopy shows that when **AB.CO$_2$Me.*E*** is exposed to 365 nm light, ~89% of **AB.CO$_2$Me.*E*** is converted to **AB.CO$_2$Me.*Z***. By irradiating at 450 nm, the inverted process occurs obtaining ~51% of **AB.CO$_2$Me.*E*** and ~49% of **AB.CO$_2$Me.*Z***.

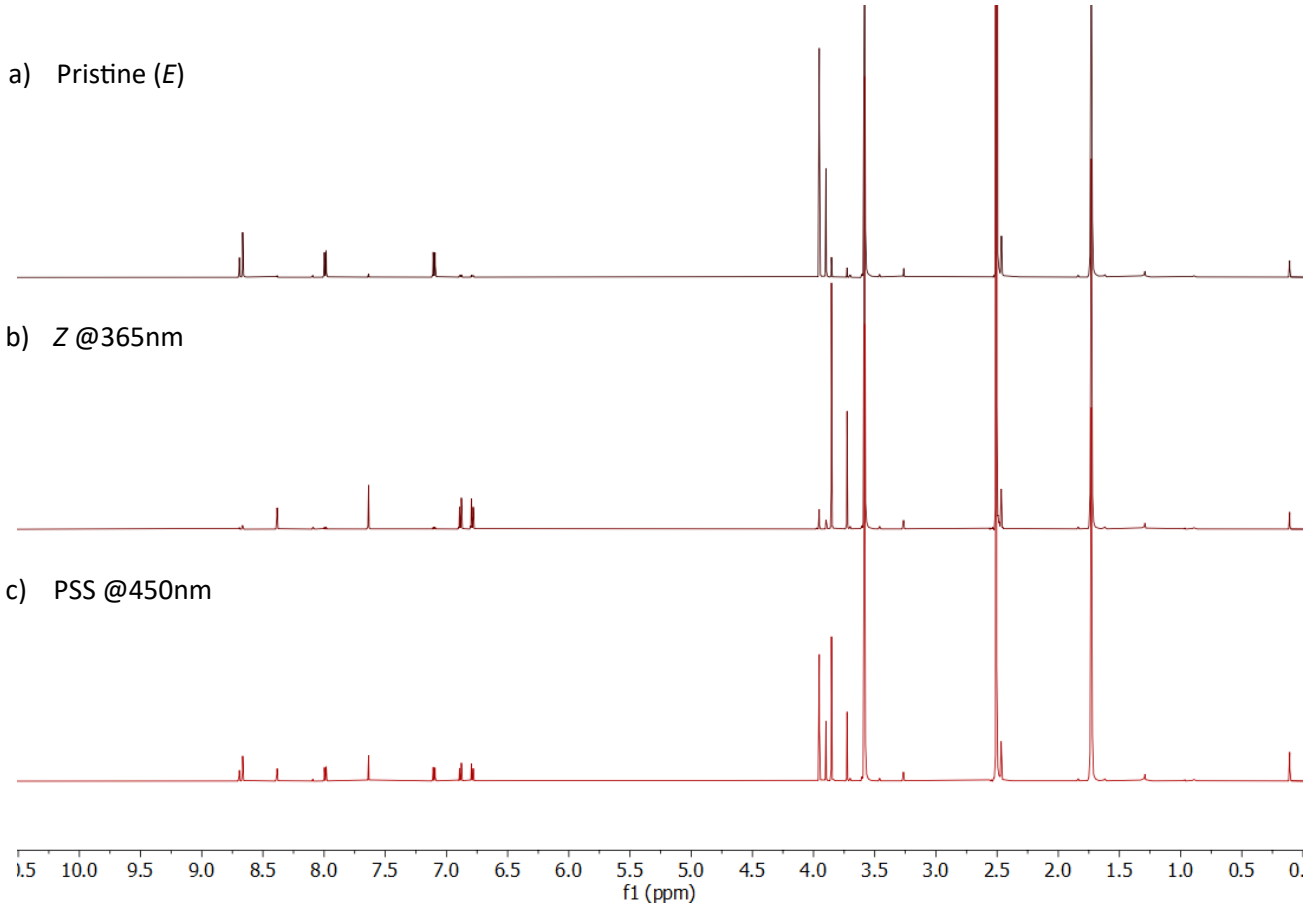


Figure 22. *E* form (a), *Z* form (b) and PSS state (c) for AB.CO$_2$Me (THF-d_8).

2.3.2. Absorption Spectra and Cyclability

A dilute solutions of **AB.Me, AB.OMe** (~7 x 10^{-6} M) and **AB.CO$_2$Me** (~2 x 10^{-5} M) in THF were placed ~4 cm from the light source and irradiated with repeated alternating cycles of t_{365nm} with 350 nm (lamp power source 6 W) and t_{450nm} with 450 nm wavelengths nm (lamp source 1 mW cm^{-2}). Irradiation time are reported in Table 6.

Table 6. Cyclability: irradiation time for **AB.Me**, **AB.OMe** and **AB.CO$_2$Me.**

Compound	t_{365nm} [min]	t_{450nm}[min]
AB.Me	13	60
AB.OMe	8	30
AB.CO$_2$Me	10	25

UV-Vis absorption spectra were recorded at 25 °C. Cyclability graphs shown in Figure 2 d-f (in the Article text) are obtained plotting the absorbance value corresponding to the λ_{max} of each compound (350 nm for **AB.Me**, 353 for **AB.OMe** and 358 nm for **AB.CO$_2$Me**) for each cycle of irradiation.

2.3.3. Thermal Relaxation Details

The thermal relaxation kinetics of compounds **AB.Me**, **AB.OMe**, **AB.CO$_2$Me** were investigated by UV-Vis spectroscopy. Diluted solutions (~1 x 10^{-4} M) of the compounds in THF were prepared and the UV-Vis absorption spectra were recorded at 25 °C. Samples were irradiated with 365 nm wavelength for 30 s and then analysed through UV-vis spectrometer in every 3 hours. Kinetic curves were plotted by following the maximum absorbance of light (at 350 nm for **AB.Me**, 353 nm for **AB.OMe** and 357 nm for **AB.CO$_2$Me**) during thermal relaxation from *Z* form to the *E* one.

Reproduced from Sanna A.L., Pachova T., Catellani A., Calzolari A., Sforazzini G., Meta-Substituted Asymmetric Azobenzenes: Insights Into Structure-Property Relationship, *Molecules*, **2024**, 29, 1929 with permission from MDPI.

Link to the published article https://doi.org/10.3390/molecules29091929.

---

3. Supramolecular Interactions as a Control Mechanism in Organic Electronics

3.1. State of Research

In organic electronics, the arrangement of π-conjugated molecules in their solid form is pivotal. The molecular layout is heavily influenced by intermolecular forces such as π-π stacking, dipolar interactions, and charge transfer mechanisms, which are crucial in determining the routes for charge flow.[94-96] Gaining insights into the way these forces operates in semiconductor thin films is crucial for enhancing the power conversion efficiency, durability, and performance of devices based on organic electronics. A careful selection of the functionalities placed both as side and terminal groups, as well as the strength of the molecular interactions to be promoted, is crucial for appropriately balancing and optimizing both the electrical and mechanical characteristics of the material. The use of supramolecular interactions necessitates a meticulous evaluation of the molecular design to be adopted to avoid disadvantages such as the sensitivity of supramolecular assemblies to external conditions and unfavorable morphologies, potentially hindering the efficiency of charge transport.
There has been considerable effort in refining OSC efficiency by fine-tuning the energy levels of π-conjugated molecules and polymers and judiciously choosing solubilizing side chains to influence their solid-state configuration post-solution processing. Indeed, selecting inappropriate solubilizing groups can negatively affect optoelectronic device performance. This is due to the fact that these side chains might encourage molecular structures conducive to local charge mobility but result in limited overall charge transport.[97-101]

Investigating post-synthesis methods to manage the structural arrangement of molecules is highly intriguing. Standard approaches include employing processing additives in the organic semiconductor solutions during the drying phase, and applying heat treatments to the resultant thin films. Owing to their unique properties and impacts, additives are divided into two groups: solvent additives and solid additives. Solvent additives, the first group, mainly influence the state of the solution and the dynamics of evaporation throughout the film creation process. These additives possess a boiling point higher than that of the primary solvent, resulting in a decelerated evaporation time during film formation, thereby enabling precise adjustments to film crystallinity and phase segregation in blends.[102]

On the other hand, solid additives function differently from their solvent-based counterparts, primarily by modifying the intermolecular interactions within π-conjugated materials and because they get integrated into the films, eliminating the need for high-temperature removal. This aspect is particularly advantageous as it circumvents the potential for film deterioration that could degrade device efficiency. Notable examples of solid additives include 7-dibromo-9,9-dimethyl fluorene (DBDMF), derivatives of hydroxy-methylpyrimidine, 9-fluorenone-1-carboxylic acid (FCA), 2-benzylidene-1-indene-1,3-dione and its variants, and diiodine (I_2).[103] The latter is especially interesting as it's also commonly used as a p-type chemical dopant in both small molecules and π-conjugated polymers, enhancing the density of charge carriers in the semiconductor layer. Yet, the effective generation of charge carriers is critically dependent on the even distribution of the dopant within the substance. To meet this goal, several factors during the film laying process must be meticulously adjusted. It has been shown that the application of elevated temperatures can be beneficial for this aim. Thus, employing a solid dopant might be less energy-efficient if heating is required during the production of optoelectronic devices.[103]

In this thesis work, we have chosen to focus on the use of solid additives. Specifically, to address this issue, we propose utilizing the end functionality of semiconductors as anchorage points for solid additives to achieve a uniform distribution within the materials even at ambient temperature. In our research efforts, we have adopted two distinct approaches to explore innovative pathways in organic electronics, each tailored to enhance the performance and integration of organic materials into electronic devices through molecular functionalization.

The first research approach involves the synthesis of a polymer, specifically poly(3-hexylthiophene) (P3EHT), where terminal units have been functionalized to foster hydrogen bonding interactions with matching additives. This approach is aimed at improving the intermolecular cohesion and assembly of the polymer chains, potentially leading to enhanced charge transport properties. The functionalized terminations are designed to engage in specific hydrogen bonding interactions (Figure 23), thereby influencing the polymer's microstructure and electronic properties. This method holds promise for the development of materials with controlled morphologies and tailored optoelectronic characteristics.

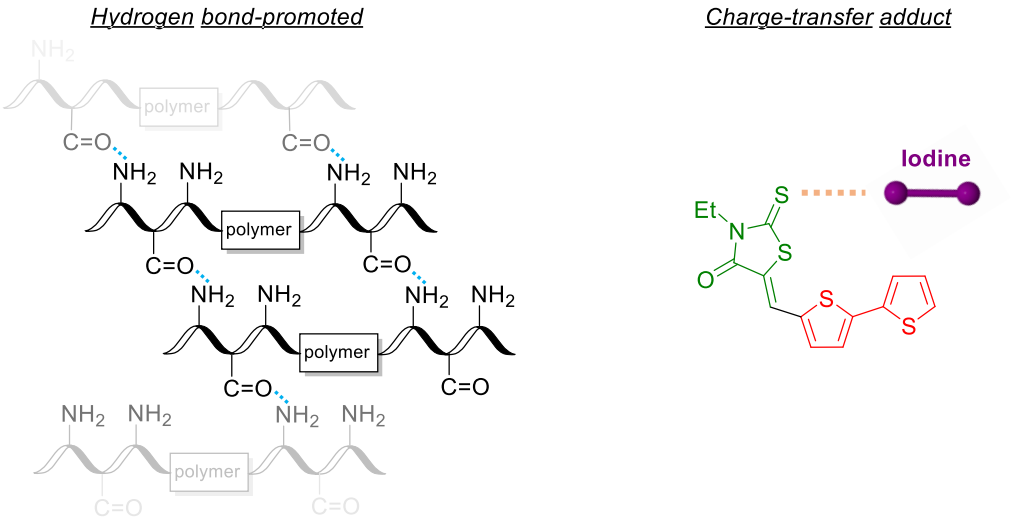


Figure 23. Schematic representation of the intermolecular interactions promoted in P3EHT and rhodanine-based bithiophene.

The second line of research is focused instead on small molecular building-blocks based on bithiophene (Figure 23) to investigate their ability to form charge transfer adducts with iodine, exploring the use of an dihalogen molecule as an additive. This approach leverages the intrinsic electronic properties of the bithiophene core and explores the potential for direct charge transfer interactions with iodine, aiming to elucidate the mechanisms governing these processes and their implications for material design in organic electronics.

Both approaches underscore the pivotal role of terminal unit functionalization in modulating the physical and electronic properties of organic materials. The exploration of hydrogen bonding interactions and direct charge transfer mechanisms opens up avenues for the rational design of organic semiconductors with enhanced performance. Further details regarding the outcomes and insights derived from these research pathways will be provided subsequently.

3.2. Supramolecular Modification of P3EHT

This part of the PhD project was carried out during the 6 months research period spent at the École Polytechnique Fédérale de Lausanne (EPFL) in Switzerland, conducted in the Laboratory of Macromolecular and Organic Materials (LMOM) led by Prof. Holger Frauenrath.

P3EHT stands as a pivotal polymer in the field of organic electronics, primarily attributed to its impressive charge transport properties and environmental stability. This semiconducting polymer has garnered significant attention due to its extensive application in devices such as OFETs, OPVs and OLEDs. Structurally similar to the more widely known poly(3-hexylthiophene), P3EHT differentiates itself through its ethylhexyl side chain, which imparts unique characteristics to the polymer, including solubility and film-forming properties. The alkyl side chains of P3EHT not only afford solubility in common organic solvents, facilitating processability, but also play a crucial role in determining the polymer's crystallinity and, consequently, its electronic properties. Moreover, good processability is crucial for the fabrication of organic electronic devices through cost-effective methods such as spin-coating and printing technologies.

The exploration of P3EHT stems from the broader research into conducting and semiconducting polymers that began in the latter part of the 20th century. Following the pioneering discovery of the conductive properties of polyacetylene in the 1970s, there was a surge in interest in conjugated polymers as potential materials for electronic applications. P3EHT was developed in the quest for polymers that combined the processability and mechanical flexibility of plastics with the electronic functionalities of metals or semiconductors. Its discovery was part of the ongoing effort to optimize the side chain structure of polythiophenes to enhance their solubility, processability, and device performance.

Hydrogen-bonding interactions aligned with the π–π stacking direction have frequently been employed to enhance supramolecular self-assembly in solutions of oligothiophene or perylene bisimide derivatives.[104] In the field of supramolecular chemistry, the intricate process of constructing helical-type structures through hydrogen bonding[105] showcases a novel method for organizing complex molecular systems. This approach leverages the specificity and directionality inherent in hydrogen bonding, enabling the self-assembly of sophisticated architectures from relatively simple polymeric chains. A critical aspect of this technique involves the careful design of these units to feature complementary hydrogen-bonding sites, often incorporating functional groups like amides or carboxylic acids known for their robust hydrogen-bonding capabilities.

This strategic inclusion ensures that upon mixing with an appropriate matching additives, the polymer chains initiate a self-assembly process guided by hydrogen bonds. The resultant helical architectures not only benefit from the thermal stability conferred by hydrogen bonds but also offer potential for various applications, enhancing the field of materials science, nanotechnology, and beyond. Yet, the challenge lies in selecting substituents that can engage in desired hydrogen bonding without disrupting their interaction with processing additives. This compatibility is vital for maintaining the structural integrity of the helices during processing, ensuring the preservation of hydrogen bonds essential for the assembly. Achieving this balance enables the creation of helical thiophene-based materials, which hold promise for a myriad of applications, including organic semiconductors, sensors, and more.

In this thesis work the synthesis of this modified P3EHT was carried out, ensuring that the newly introduced functional groups at the polymer's termination are precisely positioned to foster hydrogen bonding with specific additives. To this scope, the synthetized polymers will carry self-assembling end groups (like carboxylic acids, amides, or hydroxyl groups) that can allow the formation of one-dimensional helical aggregates when matched with low molecular weight additive based on the same self-assembling motif. By varying the terminal self-assembling functionalities and the additive, it will be possible to tailor the formation of nanofibrils in the materials, and as so to modulate their physical properties. In parallel, the synthesis of these complementary additives has been successfully achieved. These molecular entities are designed to integrate seamlessly into the P3EHT framework, establishing a synergistic relationship that enhances the overall performance of the resulting composite material. By creating these non-covalent bonds, an improvement in the morphological stability and charge transport capabilities of P3EHT could be afford, thereby extending its applicability in organic electronics. This tailored approach not only demonstrates the versatility of P3EHT as a foundational material for organic electronics but also highlights the importance of chemical synthesis and material engineering in the development of advanced functional materials.

In order to explore an additional application of this approach, we have opted to utilize this strategy of functionalizing the terminations by also leveraging a hypothetical bithiophene central core, the synthetic design of which will be presented later.

3.2.1. Regioregular Polymers: McCollough Reaction

The development of regioregular polymers represents a pivotal advancement in the field of organic electronics, underpinning significant progress in the synthesis of conductive and semiconductive polymeric materials. Among the myriad of synthetic methodologies devised for this purpose, the McCullough method for the synthesis of regioregular polyalkylthiophenes has garnered substantial attention due to its effectiveness and the high quality of the polymers obtained.[106] In polymer chemistry, the regiochemistry of polymerization reactions—specifically the orientation of substituent groups attached to the monomer units in a polymer chain—is of paramount importance. Given that 3-alkylthiophene lacks symmetry, three distinct spatial configurations are possible when two thiophene rings are linked between the 2- and 5-positions. The initial configuration is 2,5' or head-to-tail coupling (hereinafter referred to as HT), the second configuration is 2,2' or head-to-head coupling (HH), and the third is 5,5' or tail-to-tail coupling (TT). Each of these methods results in compounds that exhibit three potential regiochemical orientations: HH, TT, and HT (Figure 24). For polythiophenes and other conjugated polymers, achieving a regioregular HT configuration is crucial for optimizing the material's electronic properties. This configuration promotes an extended π-conjugation along the polymer backbone, essential for efficient charge transport and high electrical conductivity.

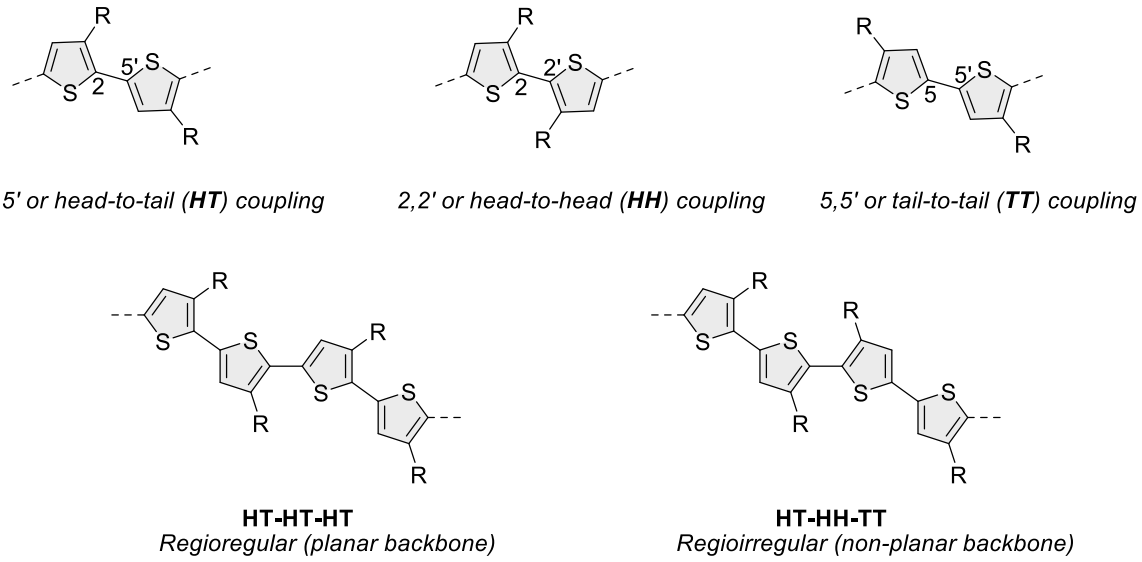
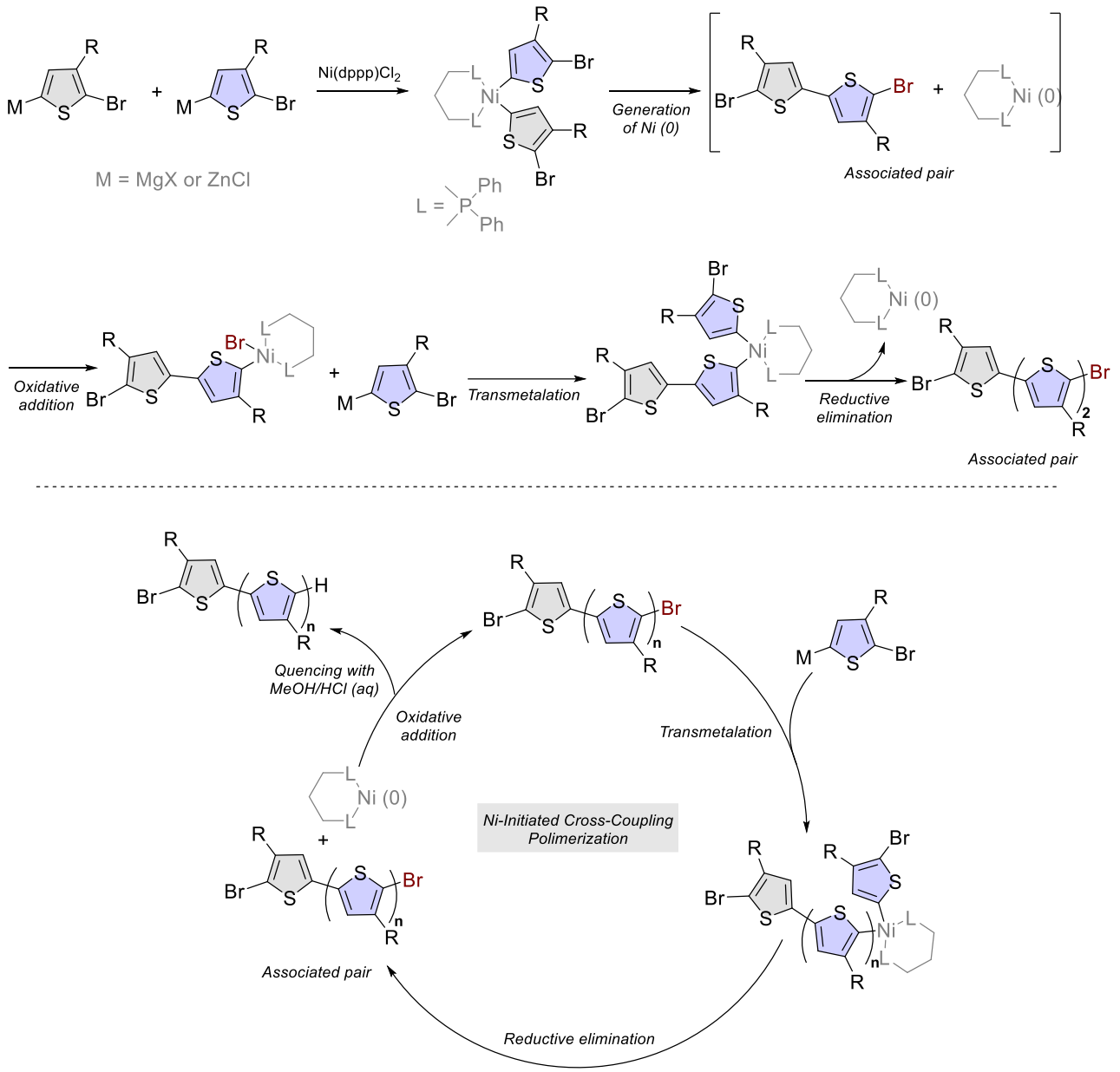


Figure 24. Spatial conformations of 3-alkylthiophenes: head-to-tail (**HT**), head-to-head (**HH**), tail-to-tail (**TT**).

Prior to the development of the McCullough method, the synthesis of regioregular polythiophenes was met with significant challenges that largely stemmed from the limitations of existing synthetic techniques. These early methods often produced polymers with mixed regiochemistry, which in turn, led to materials with variable electronic properties and diminished performance in electronic applications. One of the first approaches to synthesizing polythiophenes involved chemical oxidative polymerization.[107] This method used iron(III) chloride or other strong oxidizing agents to facilitate the coupling of thiophene monomers. However, this technique suffers from several drawbacks, including a lack of control over the polymer's molecular weight, a tendency to produce polymers with a broad molecular weight distribution, and, most critically, an inability to selectively achieve head-to-tail regiochemistry. The resulting polymers were often a mixture of head-to-head, head-to-tail, and tail-to-tail couplings, leading to a non-uniform π-conjugation along the polymer backbone and, consequently, inconsistent electrical conductivity. Electrochemical polymerization of thiophenes represented another method used before the advent of the most recent techniques.[108] While this approach offered some advantages, such as the direct formation of polythiophene films on electrodes, it similarly suffered from a lack of regiocontrol. The electrochemical conditions favored the rapid formation of polymers but did not discriminate between different orientations of thiophene units. Thus, like oxidative polymerization, this method yielded polymers with varied and unpredictable electronic properties. Moreover, early attempts at the chemical synthesis of polythiophenes often relied on step-growth polymerization strategies, which also struggled to produce regioregular polymers. These reactions, while useful for demonstrating the feasibility of synthesizing polythiophenes, did not provide a practical pathway to materials with the consistent and reproducible properties necessary for electronic applications.[109] The McCullough method, developed in the early 1990s by Richard D. McCullough at the University of Florida, emerged as a breakthrough in this context. By employing a controlled metal-catalyzed cross-coupling reaction, this method allowed for precise control over the polymerization process, ensuring that the resulting polythiophenes possessed a regular head-to-tail configuration. This method hinges on the controlled coupling of 3-alkylthiophene monomers to achieve a predominant head-to-tail (HT) configuration, which is essential for optimizing the material's electronic properties. The mechanism of this synthetic strategy can be described in the following steps, as reported in Scheme 2.



Scheme 2. Mechanism of McCollough Reaction.

The first step involves a magnesium-bromine exchange reaction. This transmetalation step is crucial for preparing the monomer for the subsequent polymerization process, as it forms a stable organometallic species that is more reactive towards the nickel-catalyzed coupling reaction. The final step involves the polymerization of the organometallic monomer under the catalysis of a nickel(II) complex. Commonly, nickel dichloride ($NiCl_2$) in combination with a bidentate phosphine ligand (e.g., 1,3-bis(diphenylphosphino)propane, dppp) is used as the catalyst. The nickel catalyst facilitates the coupling of the monomer units through a cross-coupling reaction, leading to the formation of the polythiophene chain. Importantly, this catalytic system promotes the formation of the polymer with a regioregular HT configuration.

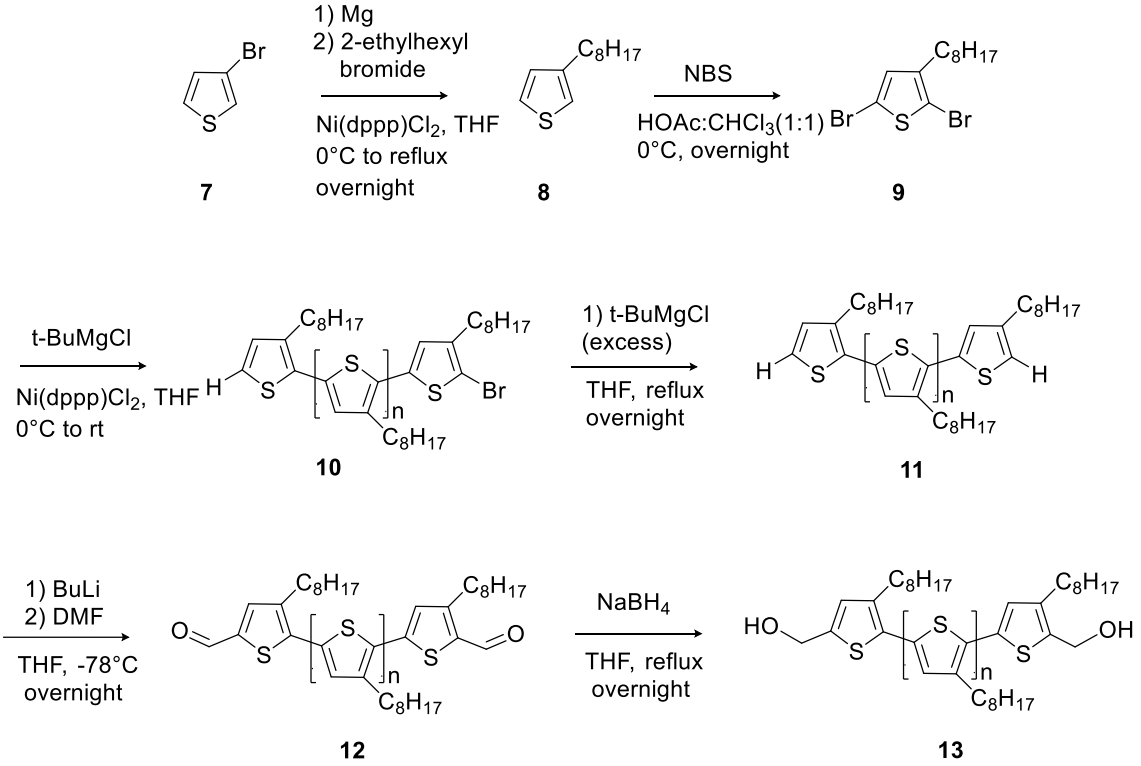
The strength of the McCullough method lies in its simplicity and the high degree of control it offers over the polymerization process. It enables the synthesis of polythiophenes with regioregularities exceeding 90%, a significant improvement over previous techniques. Additionally, the method is versatile, allowing for the introduction of various alkyl side chains, which can tailor the solubility and processing properties of the resulting polymers. The McCullough method for synthesizing regioregular polythiophenes stands as a cornerstone in the field of conductive polymer chemistry. This control over regiochemistry was unprecedented and addressed the primary limitation of earlier synthesis techniques. Its development not only solved a fundamental challenge in the synthesis of polythiophenes but also set the stage for the widespread adoption and continued innovation in organic electronics. The method's simplicity, effectiveness, and versatility underscore its importance and continue to make it a valuable tool for researchers and industry professionals alike.

As mentioned previously, in this thesis work, we have focused on the molecular design of P3EHT and corresponding matching additives. To this end, we have chosen to utilize the McCollough reaction with the aim of obtaining a polymer with maximum HT regioregularity. The results of the experimental activities conducted will be presented in the following sections.

3.2.2. Results and Discussion

3.2.2.1. Design of P3EHT Synthesis

Starting from 3-bromo thiophene (**7**), the branched alkyl chain of ethyl hexyl was introduced through a Grignard reaction, utilizing Ni(dppp)Cl_2 as a catalyst (Compound **8**, Scheme 3). The resulting compound underwent bromination at the 2 and 5 positions of the thiophene ring, employing N-bromosuccinimide as the brominating agent, obtaining Compound **9**. Subsequently, we embarked on the McCollough synthesis aimed at yielding a regioregular polymer (**10**).



Scheme 3. Synthetic path for functionalized P3EHT (**13**).

Experiments were conducted to assess the molecular weight of the polymer over time (Figure 25), reaching a molecular weight of 12000 g/mol. Molar weight of the polymers obtained was estimated through Gel Permeation Chromatography (GPC) measurement. GPC separates polymer molecules based on their size as they pass through a porous column. Larger molecules elute faster because they are excluded from entering the smaller pores, while smaller molecules penetrate these pores and elute later. THF was used as solvent for both prepare the samples and running through the system.

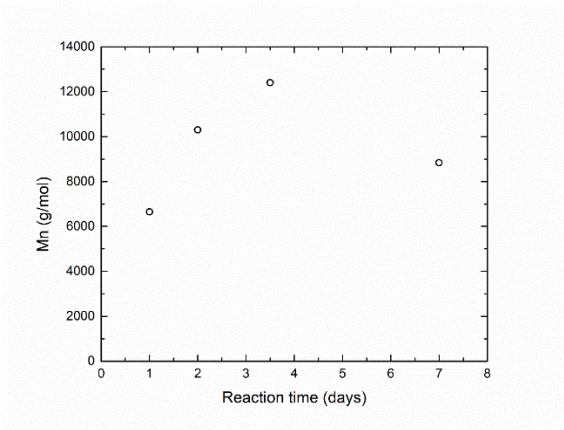


Figure 25. Molecular weight of obtained polymer vs reaction time.

As can be seen from Figure 25, while keeping the molar ratio of the monomer to the catalyst constant, an increase in the molecular weight of the polymer is observed as the reaction time extends from 1 day to 3.5 days. With longer times (7 days), a decrease in the final molecular weight was recorded. This effect could be due to an increased probability of side reactions occurring between polymer chains. The obtained polymer **10** was then treated with tert-butyl magnesium chloride to substitute the bromine on the terminal thiophene of the chain with a hydrogen (**11**), thereby rendering two active terminal sites available for further functionalizations. Two aldehyde groups were incorporated through metallation with butyllithium, followed by quenching with DMF (**12**). Subsequently, the aldehyde group was reduced using sodium borohydride, making the hydroxyl functionality available for coupling reactions with carboxylic acids compatible with the matching additives, **13**. This methodical approach not only facilitated the synthesis of a functionalized P3EHT but also ensured its compatibility with additives used in processing these molecules, particularly emphasizing thiophene-based monomers or matrices. The strategic insertion of functional groups and the subsequent polymer treatment aimed to enhance the material's applicability in organic electronic devices, leveraging the intrinsic properties of P3EHT and its functional derivatives. Regarding the functionalization of the polymer terminations, the laboratory activity concluded with the obtaining of the alcohol group due to the duration of the project at the LMOM Laboratory. Due to the timing related to the period spent abroad, it was not possible to proceed with obtaining supramolecular compounds resulting from the

combination of the functionalized P3EHT polymer with the matching additives. The synthetic pathway would involve a Steglich esterification reaction, utilizing synthesized carboxylic acids whose synthesis is shown in the following section, in order to introduce terminations in the polymer containing functional groups suitable for promoting hydrogen bonds between the polymer and matching additives, as illustrated in Figure 26.

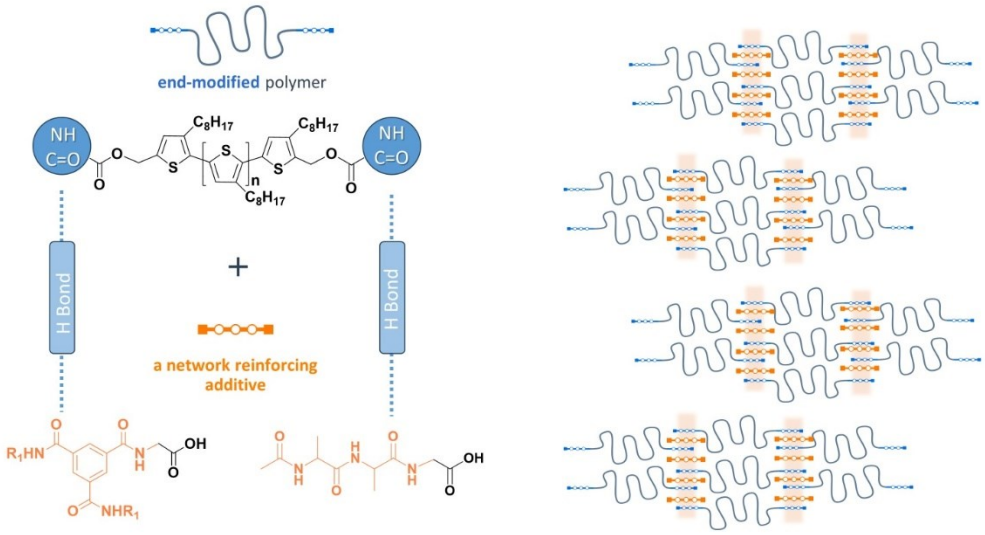


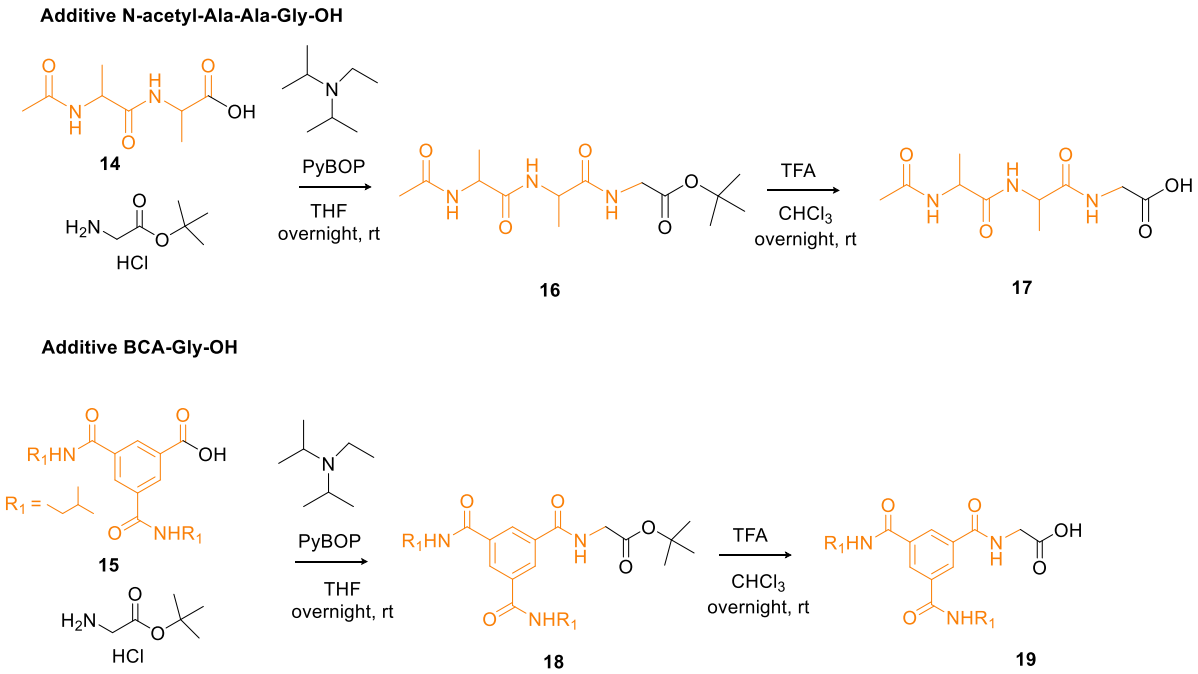
Figure 26. Formation of hydrogen-bond promoted motif between end-modified polymer and the reinforcing additives.

3.2.2.2. Matching Additives Synthesis

As previously mentioned, the matching additives were designed to feature terminal self-assembling functionalities compatible with those of the polymer. We opted to synthesize structures containing amide bonds internally, utilizing glycine through two potential synthetic routes.

The first amidation reaction involved the coupling of tert-butyl protected glycine hydrochloride with the amino acid N-acetyl-Ala-Ala-OH, in the presence of a base (di-isopropyl ethyl amine) and the coupling agent PyBOP. The resulting compound was then deprotected using trifluoroacetic acid (TFA) to obtain the desired compound **N-acetyl-Ala-Ala-Gly-OH** (**17**) with a yield of 90 % (Scheme 4).

The second synthesized additive used the same reaction conditions as described above. This time, glycine was reacted with a benzene carboxamide derivative (**BCA**, previously synthesized by the staff of the host laboratory) to produce the compound **18** which was subsequently deprotected with TFA to obtain the final desired compound **BCA-Gly-OH** (**19**), with a yield of 98% (Scheme 4).



Scheme 4. Synthetic path for Additive **N-acetyl-Ala-Ala-Gly-OH** and Additive **BCA-Gly-OH**.

3.3. Charge-Transfer Adduct in Bithiophene Derivatives

Diving into the study of the domain of charge transfer adducts between bithiophene building blocks and dihalogens, this chapter addresses the synthesis of such organic compounds and the investigation of various crystallization conditions to foster these soft-soft interactions. The focus on bithiophene-functionalized and iodine stems from their potential to create materials with customizable electronic properties, leveraging the soft-soft interactions crucial for the advancement of organic electronics. Bithiophene-based systems are particularly appealing due to their electronic flexibility and structural adaptability, positioning them as ideal candidates for the formation of charge transfer complexes with significant implications for tunable conductivity, photo-responsiveness, and semiconducting behavior.

This section of the PhD project was carried out within the collaboration with Professor Arca and Prof.ssa Aragoni from the Department of Chemical and Geological Sciences.

3.3.1. Crystal Engineering

Crystal engineering is a multidisciplinary field of science involving the design and synthesis of solid structures with desired properties and functionalities. It focuses on understanding and manipulating the intermolecular interactions that govern the formation and organization of crystals. Crystal engineering goes further by employing principles of supramolecular chemistry and crystallography to design and create new, highly organized (crystalline) structures with specific properties.[110] The precise design of π-conjugated compounds with specially tailored functional groups to control molecular organization, combined with the development of material processing methodologies (for example, the addition of additives, controlled solvent evaporation, etc.), has enabled the production of high-performance optoelectronic devices. In the crystal engineering of organic π-conjugated materials, molecules are bonded through weak interactions such as hydrogen bonds, π-stacking, van der Waals forces, and halogen bonds.

Aiming to develop a method to control the molecular organization of organic semiconductors using terminal functional groups, we analyzed which type of interaction could be effective without compromising the chemical structures of the semiconductors themselves. Considering the chemical structure of the functional groups in Chapter 1, such as rhodanine and its derivatives, it can be hypothesized that the thio-carbonyl sulfur is susceptible to forming adducts with external species (additives). These additives must satisfy two essential conditions: the first is not to negatively

compromise the performance of the device, while the second is to have sufficiently strong interactions with the heteroatoms present in the terminal functional groups of the compounds.

Considering our intention to leverage the terminations of molecules to promote a precise arrangement in the solid state, we have directed our attention towards atoms (and, in general, functional groups) commonly found in the structures of organic semiconductors and towards additives that can be utilized in room temperature treatment processes, with the aim of avoiding complex post-synthesis crystallization strategies. Non-metallic species like dihalogen molecules can also be used for this scope. It is known that these can strongly interact with chalcogens (S, Se, etc.) to form stable adducts. Moreover, dihalogen molecules are compatible with the π-conjugated architecture of the semiconductors, as they are also used as dopants for organic semiconductors, especially thio-based ones such as P3HT. This suggests that dihalogens could be ideal candidates for thio-based compounds containing functional groups like rhodanine.

Understanding the role of specific intermolecular interactions in crystal growth is of particular interest in the design of drugs, pigments, and materials for energy applications. The interaction between molecular iodine (I_2) and compounds containing chalcogen donors (such as sulfur, selenium, tellurium) plays a crucial role as it enables the development of biologically and pharmacologically active structures, as well as increasingly fundamental new materials with unique electrical properties based on chalcogens. In cases where the halogen is molecular iodine, the formation of charge transfer adducts is quite common. It is well-known that in the aforementioned structures, the interaction between a lone pair of electrons located on the donor atom and the I_2 molecule leads to an elongation of the I-I distance.

A simplified description according to molecular orbital theory shows that the interaction involves an electronic charge transfer from the donor's HOMO to the iodine's LUMO σ*. Since the latter is an antibonding molecular orbital, the interaction results in an elongation of the I–I bond. Thus, the stronger the interaction between the donor and acceptor, the greater the amount of charge transferred from the HOMO to the LUMO.

In 1999, Prof. Devillanova's group conducted a systematic study on a series of chalcogen donors with molecular iodine in 1:1 charge transfer adducts. This study revealed that thiocarbonyl groups interact with molecular iodine more efficiently compared to sulfides (R-S-R) and selenides (R-Se-R). Several examples of complex self-assembled infinite polyiodide network have been reported by Aragoni et al.[111] showing the fundamental role of halogens-chalcogen bonds in the structural and spatial organization in different types of materials. This example illustrates how the presence of sulfur can influence a complex network in the three-dimensional structure of a given material.

To explore the possibility of using dihalogens as additives for the formation of adducts with oligothiophenes functionalized with rhodanine, two model compounds were prepared. These compounds feature a π-conjugated system consisting of two thiophene units. The choice to use a single bithiophene segment offers several advantages, including synthetic simplicity, the absence of the need for solubilizing groups, and the ability to study dedicated interactions between the dihalogens and the electron-attracting groups.

With the aim of developing efficient procedures for controlling the molecular organization of thiophene-based semiconductors, a series of experiments were planned and conducted to determine whether dihalogens can form adducts with rhodanine and whether these adducts induce a different molecular order compared to that achievable without dihalogens.

In our pursuit of optimizing these charge transfer adducts, an extensive exploration of synthetic methodologies was undertaken, with a particular emphasis on the interaction dynamics between the organic frameworks and dihalogen molecules. The goal was to achieve stable complexes that demonstrate an ideal blend of structural coherence and electronic attributes. To this end, various crystallization parameters, including solvent choice, temperature, and methodology, were meticulously examined to influence the adducts' morphology and electronic interactions beneficially.

Additionally, the crystals thus obtained were subjected to preliminary electrical conductivity tests, aiming to assess their potential in electronic applications. These evaluations are crucial for understanding the materials' behavior under practical conditions and further tailoring their properties for specific uses in organic electronic devices.

3.3.2. Results and Discussion

3.3.2.1. Design and Synthesis of Bithiophene-Rhodanine Based Compounds

The exploration of charge transfer interactions between organic semiconductors and dihalogens necessitates a detailed understanding of the underlying chemistry that governs these processes. A critical aspect of this research lies in the molecular design, specifically targeting the functionalization of bithiophene building blocks with electron-withdrawing groups such as rhodanine. This design strategy is motivated by several key factors that underpin the efficiency and effectiveness of charge transfer within these compounds.

The choice of the bithiophene segment as the core unit is rooted in its well-documented electronic properties, primarily its capacity to facilitate π-conjugation and thereby support efficient charge delocalization. Bithiophene's structural flexibility and electronic versatility make it an ideal candidate for modification with electron-donating moieties, aiming to enhance its interaction with dihalogens, particularly iodine.

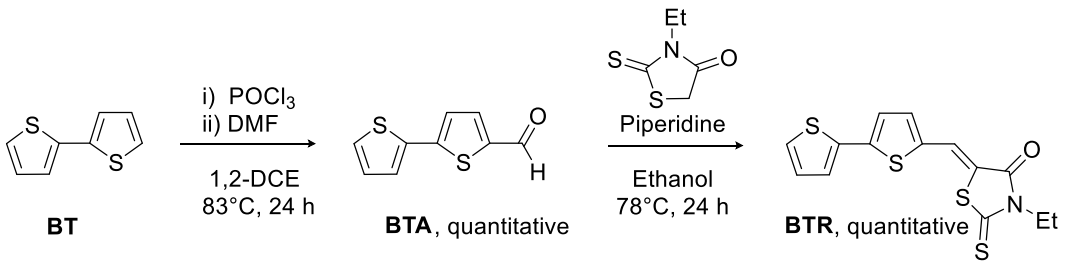
The incorporation of rhodanine, distinguished by its potent electron-withdrawing ability, enriches the design not only by facilitating the formation of stable charge transfer adducts with dihalogens but also by adding crucial coordination sites. These sites are essential for delving into the characteristics of dihalogens-thiocarbonyl interactions, highlighting rhodanine's versatile role in the molecular architecture. This approach is anticipated to shed light on the formation of charge transfer complexes, offering insights into their potential application in organic electronic devices. Rhodanine, known for its potent electron-withdrawing capabilities, plays a crucial role in modulating the energy levels of these semiconductors, thus influencing their charge transport behaviors and overall performance in electronic applications. The addition of rhodanine enhances this architecture by lowering the LUMO (Lowest Unoccupied Molecular Orbital) energy levels, thereby improving electron affinity and facilitating stronger interactions with dihalogens like iodine.

The investigation into compounds with single and double coordination sites, specifically Bithiophene-Rhodanine (Compound **BTR**) and Bithiophene-Rhodanine Disulphur (Compound **BTR-2S**), is designed to elucidate the impact of these interactions on the material's electronic properties.

The synthetic approach toward these functionalized bithiophene compounds involved exploring a variety of methodologies to optimize the integration of rhodanine, aiming for an efficient and effective synthesis process. Initial attempts at direct formylation started with the exploration of metallation using butyllithium. This initial step aimed to activate the thiophene ring, facilitating the introduction of formyl groups. Despite the theoretical advantages offered by butyllithium for the direct formylation of the active position of thiophene, the reaction yields were notably low, not exceeding 15%. This outcome necessitated a reevaluation of the synthetic strategy to achieve the desired functionalization more effectively.

Transitioning from the metallation approach, attention was directed towards palladium-catalyzed reactions, specifically the Suzuki coupling, as a more promising method for constructing the bithiophene backbone. The reaction between 2-thiophene boronic acid and 2-bromo-5-formyl-thiophene, catalyzed by palladium tetrakis in a tetrahydrofuran (THF) solvent, represented a strategic approach in the synthetic process. This method successfully produced the target compound with a significantly improved yield of about 42%, highlighting the Suzuki coupling's efficacy in facilitating the desired bond formation.

Building upon the foundation laid by the Suzuki coupling, the synthesis progressed to the final stage of functionalization using Vilsmeier's reagent for the monoformylation of the bithiophene core. The preparation of Vilsmeier's reagent, involving the combination of phosphoryl chloride and dimethylformamide, was conducted under an inert atmosphere, with 1,2-dichloroethane serving as the solvent. This step was critical for introducing the formyl group, which is essential for the subsequent attachment of the rhodanine moiety. Initial attempts yielded approximately 63% of the desired product; however, through the optimization of reaction conditions, including the use of excess Vilsmeier reagent, the process was refined to achieve a quantitative yield, marking a significant advancement in the synthesis of Compound 2,2'-bithiophene-5-carbaldehyde (**BTA**).



Scheme 5. Synthetic scheme for the preparation of **BTR** (**20**).

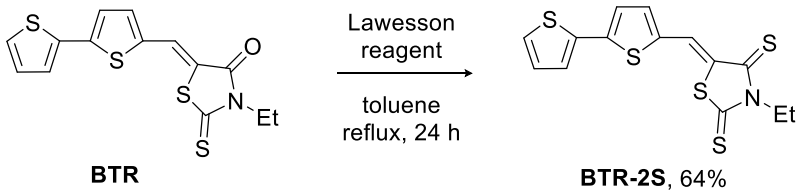
The strategic synthesis of bithiophene compounds, transitioning from butyllithium metallation through palladium-catalyzed Suzuki coupling to Vilsmeier's reagent formylation, exemplifies the intricate and adaptive nature of organic synthesis in constructing complex molecular architectures. This journey not only reflects the challenges encountered in synthesizing thiophene-based building blocks but also underscores the importance of selecting appropriate synthetic methodologies to achieve high-yield and high-purity compounds.

Addressing the design objective of incorporating a double coordination site, the transformation of the carbonyl oxygen in rhodanine to an additional sulfur atom was pursued. Lawesson's reagent emerged as the reagent of choice for this sulfurization step, although the optimization of reaction conditions proved challenging (Table 7).

Table 7. Trials conditions for Lawesson reaction.

Conditions	Solvent	Time	Desired product
1	1,4-dioxane	1.5 h	No
2	Toluene	1.5 h	No
3	Toluene	24 h	Yes

Referring to a synthesis reported in the literature on a similar substrate, Compound 2 was reacted with Lawesson's reagent in 1,4-dioxane for 1.5 h. Subsequent to the work-up, ^{1}H-NMR analysis and mass spectrometry showed a perfect overlap of the spectrum of the initial reagent with the crude reaction product, thus suggesting us to evaluate other reaction conditions. The reaction was then repeated using anhydrous toluene as a solvent and keeping the reaction time unchanged. Also in this case, unfortunately, the desired disulphurized product was not obtained. Trials across different solvents and durations finally identified toluene over 24 hours as the optimal setting for achieving the desired Bithiophene-Rhodanine Disulphur, **BTR-2S** (**21**) with satisfactory yield (64%).



Scheme 6. Synthetic scheme for the preparation of **BTR-2S** (**21**).

Comparison of the proton spectra of Compound 2 (**BTR**) and Compound 3 (**BTR-2S**) is shown in Figure 27-28.

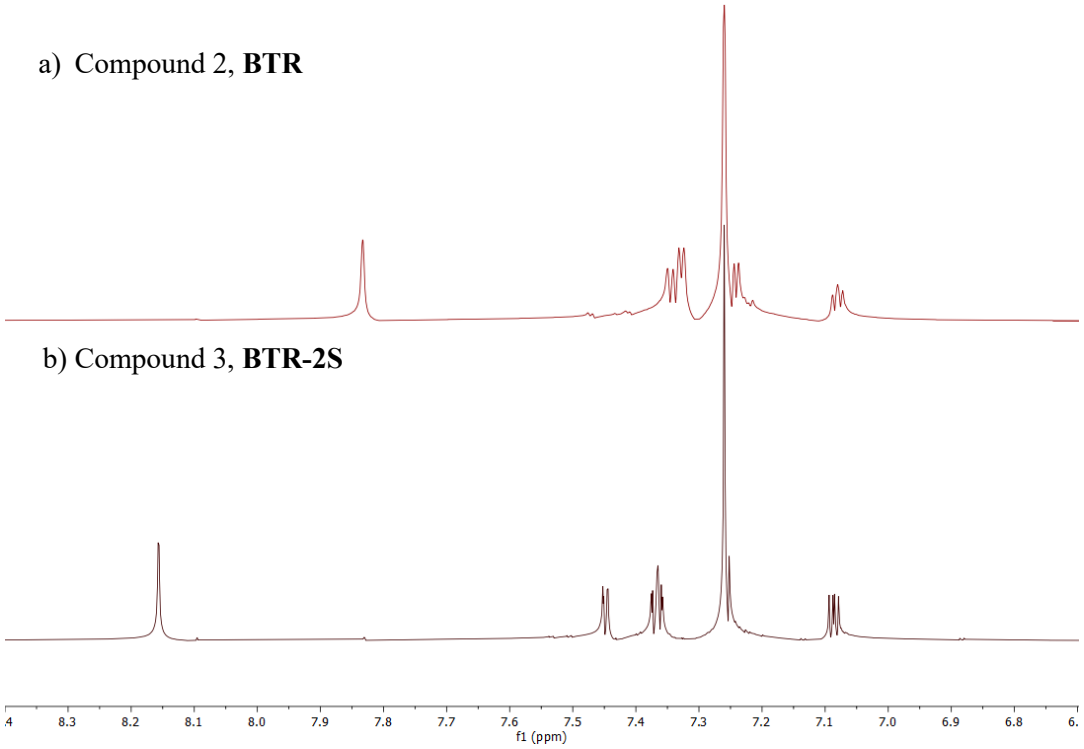


Figure 27. [1]H-NMR of aromatic region for **BTR** and **BTR-2S**.

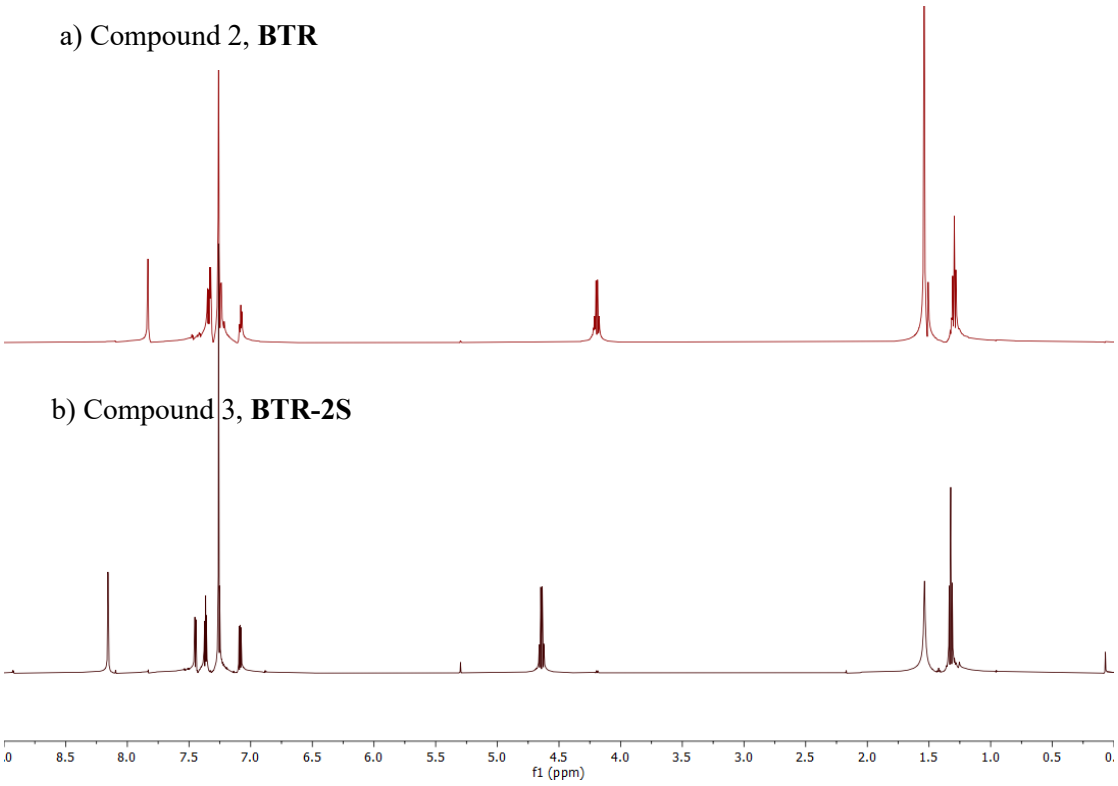


Figure 28. [1]H-NMR of aromatic region for **BTR** and **BTR-2S**.

In the context of nuclear magnetic resonance (NMR) spectroscopy, the behavior of proton shifts provides valuable insights into the structural and electronic nuances of molecules.

Upon the sulfurization of the carbonyl functionality, a marked downfield shift in the proton signal associated with the double bond is observed. This shift towards lower fields is indicative of an increased deshielding effect. The downfield shift in this proton signals could be driven by a combination of electronic, steric, and delocalization effects. The introduction of sulfur affects the π electron density and the molecular conformation, which in turn influences the electron distribution and the shielding of nearby protons. This leads to a change in the electron delocalization within the π system, potentially increasing the deshielding of adjacent protons and causing their signals to shift downfield. Collectively, these factors complexly impact the NMR chemical shifts of protons adjacent to the double bond.

The spectral data, as illustrated in Figure 28, also reveals notable variations in the signals corresponding to the protons of the alkyl chain termination (CH_2). This variation can be attributed to the modified electronic distribution along the molecular backbone post-sulfurization, affecting the electronic environment of the CH_2 protons and, consequently, their chemical shift. The influence of sulfurization extends, modifying the inductive and resonance effects within the molecule, leading to observable changes in the NMR spectrum.

Conversely, the signal of the terminal methyl group protons (CH_3) remains essentially unchanged between the two cases. The constancy of the CH_3 signal suggests that the electronic impact of sulfurization does not significantly extend to the far end of the alkyl chain, indicating that the direct electronic perturbation induced by the introduction of sulfur is localized near the modification site.

The continuation of this section would delve into the specific crystallization methodologies employed, the challenges encountered and how they were overcome, and the preliminary testing of the synthesized compounds, particularly focusing on electrical conductivity measurements to assess their potential in electronic applications.

3.3.2.2. Crystallization Experiments and X-Rays Analysis

BTR crystals were grown through the slow evaporation of an ethanol solution. The structural unit is almost entirely planar aside from the ethyl group on the rhodanine component (Figure 29a). Significantly, the sulfur atom within the rhodanine segment is aligned periplanar to the central thiophene structure, while the terminal thiophene varies in orientation, being periplanar (64%) and antiperiplanar (36%) to the main thiophene. The **BTR** units, with a minor angular difference of 1.70° between their planes, are organized in a parallel, head-to-tail manner due to offset π-π stacking bonds between the rhodanine and terminal thiophene structures (intercentroid distance = 3.68 Å for the major component), thereby constructing a column that extends along the [001] direction (Figure 29b). Parallel piles pack are orderly arranged in the [010] direction via interactions involving the ethyl groups as well as the thiophene and rhodanine structures.

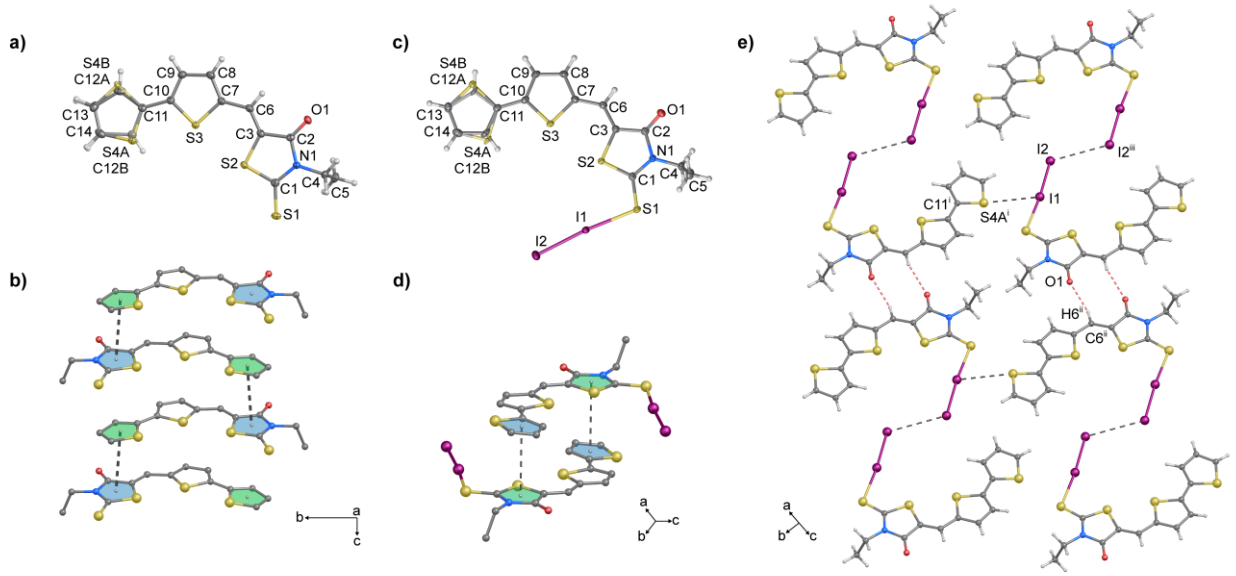


Figure 29. (a) Ellipsoid view and atom labelling scheme of compound **BTR**. The terminal thiophene ring is disordered over two positions with fractional occupancies 64:36. (b) Intermolecular interactions in the crystal packing of compound **BTR**. Hydrogen atoms and the minor component of the disordered moiety were omitted for clarity. (c) Ellipsoid view and atom labelling scheme of compound **BTR•I₂**. The terminal thiophene ring is disordered over two positions with fractional occupancies 85:15. (d) π-π Stacking interactions between **BTR•I₂** units featuring intercentroids distance of 3.67 Å when considering the most abundant position of the disordered terminal thiophenyl moiety. (e) View along the [101] direction of a portion of a ribbon motif found in the crystal structure of BTR·I_2. Ellipsoids are drawn at the 50% probability level. Hydrogen atoms were omitted for clarity in all drawings with the exception of (f). Symmetry operations: [i] = 1+*x*, 1+*y*, +*z*; [ii] = 1−*x*, 2−*y*, 2−*z*; [iii] = 1–*x*, 1–*y*, –*z*.

By diffusion of diiodine vapors into a **BTR** hexane solution or the direct combination of hexane solutions of **BTR** and I_2, only one kind of product was obtained, determined as **BTR•I₂** through single-crystal X-ray diffraction. The **BTR•I₂** crystal consist in a charge transfer "spoke" adduct with a linear (C=)S···I–I structure [S1···I1, 2.7576(5); I1–I2, 2.8067(4) Å; S1–I1–I2, 164.70(1)°; (Figure

29c). Reflecting the crystal architecture of **BTR**, the terminal thiophene is disordered and it has been modeled across two locations, with site occupancy ratios of 85:15, with a dominance of the antiperiplanar conformation. Fascinatingly, the planarity noted for the **BTR** entities within its crystal form is preserved in the CT adduct with diiodine. As is characteristic of CT interactions, the transfer of electron density from the thiocarbonyl donor to I_2 leads to a modest elongation of the C=S bond [C1–S1 = 1.632(2) and 1.666(1) Å in **BTR** and **BTR•I₂**, respectively]. Consequently, the I–I bond in **BTR•I₂** is significantly stretched compared to isolated I2 [I1–I2 = 2.806(1) and 2.715(6) Å in **BTR•I₂** and in the unbound I2,38 respectively], resulting from the CT to the diiodine antibonding σ* MO: the I–I bond length in **BTR•I₂** equates to a Pauling bond order of 0.691.39 The intensity of the CT interaction in **BTR•I₂** is less than the average of comparable CT adducts recorded in the Cambridge Structural Database (CSD) involving thiocarbonyl donors within five-membered rings and diiodine with a S···I–I component [angle exceeding 170°, 44 instances; S···I and I–I average distances = 2.695(7) and 2.879(5) Å, respectively]. The mildness of the interaction is due to the presence of the electron withdrawing carbonyl group in the rhodanine ring. The configuration of bond distances and angles in **BTR•I₂** closely mirrors those in the adduct (mdth)·I_2 (mdth = 1,5,5-trimethyl-2-thiohydantoin) [S···I 2.818(2), I–I 2.795(1) Å, S···I–I 178.03(3)°].[112]

Significantly, the S···I and I–I bond lengths within the S···I–I component align with the correlation described by Devillanova for linear triatomic systems A–B–C that include either halogens, X−X−X (X = Br, I), or combinations of halogen(s) and chalcogen(s) atoms, Ch−X−Y, X−Ch−Y, and Ch−X−Ch (Ch = S, Se; X = Y = Cl, Br, I; X = I, Y = Cl, Br, I). This correlation links the relative extensions δ1 and δ2 of the two interatomic distances to the sum of their respective covalent radii. Pairs of planar adduct units exhibit π−π stacking interactions between the rhodanine ring of one unit and the terminal thiophene ring of a symmetry-related unit (intercentroid distance 3.67 Å; Figure 29d), reminiscent of the π-π interactions observed in BTR (Figure 29b). Neighboring pairs are connected via C–S···I, C–S···S, and C–H···O weak interactions, the latter forming a $R_2^2(10)$ hydrogen bonding pattern as a result of two interacting symmetry-related rhodanine groups [C11i–S4 = 1.721(2); S4Ai···I1 = 3.660(1) Å; C11i–S4Ai···I1 = 172.66(8); C1–S1 = 1.666(2); S1···S4Ai = 3.504(2) Å; C1–S1···S4Ai =174.65(8) °; C6–H2 = 0.95 Å; H2ii···O1 = 2.34; C6ii···O1 =3.210(3) Å; C6ii–H2ii ···O1 = 151 °; i = 1+x, 1+y, +z; ii = 1−x, 2−y, 2−z. Moreover, the terminal I2 units display very weak I···I interactions, approaching the sum of their van der Waals radii (4.20 Å), reflecting a topology typical of bent type-I halogen bonds (XB) [I2···I2iii = 4.1267(5) Å; I1–I2···I2iii = 124.57(1)°; iii = 1–x, 1–y, –z; Figure 29e.

The introduction of a second thiocarbonyl unit introduces a second point of interaction as well as an increase in the electron-donating character towards the iodine molecule. Modified thiorhodanine featuring two thiocarbonyl units promotes the formation of an infinite polyiodine network. The structure shows each thiocarbonyl sulfur in the rhodanine ring [S1-C3 = 1.653(9) and S3-C5 = 1.659(8) Å, respectively] interacting with a molecule of diiodine producing a linear S–I–I arrangement [S1-I1-I2, 171.86(6)°], typical charge-transfer dihalogen adducts. The distances S1–I1 [2.874(2) Å] and I1–I2 [2.7739(9) Å] indicate that the interaction determine an elongation of the dihalogen unit as compared to the I_2 molecule [2.715(6) Å in the solid state, respectively]. The terminal iodine atom I2 of each S–I–I moiety interacts with an additional molecule of diiodine I4–$I4^{i}$ (^{i} = -x, 2-y, 2-z), which acts as bridges between the aforementioned S–I–I fragments and other S-I-I fragments belonging to another moiety. The I2···I4 contact [3.428(1) Å] is remarkably shorter than the sum of van der Waals radii (4.2 Å) and shorter than 3.6 Å, which can be considered as a threshold distance between a bonded and a non-bonded model of interactions. The I–I bond lengths of the bridging diiodine molecules [I4-$I4^{i}$, 2.730(1) Å] is shorter than that of the I1–I2 diiiodine unit, testifying for a lower extent of perturbation. The interacting molecules I1–I2, I4–$I4^{i}$, and $I2^{i}$–$I1^{i}$ form a rare example of Z-shaped neutral polyiodine sequence.

Additionally, a molecule of iodine is intercalated between two sulfur atoms S3 of molecules in adjacent planes. An angle of S3-I3-$I3^{ii}$ of 175.43(6)° is recorded (^{ii} = -x, 1-y, -z), and the distances S3-I3 and I3-$I3^{ii}$ are, respectively, 3.076(3) and 2.800(1) Å.

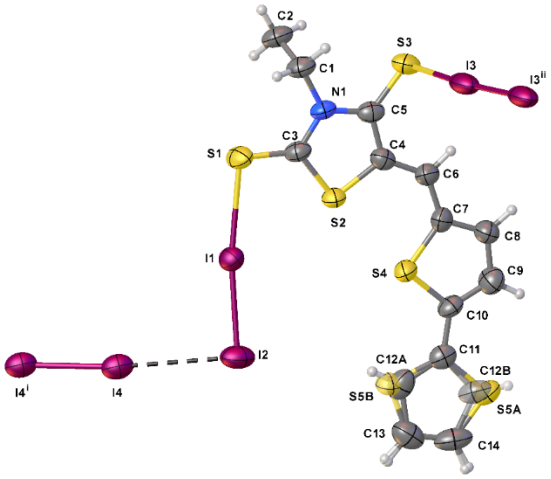


Figure 30. Crystal structure of **BTR_2S**. The terminal thiophenyl ring is disordered over two sites with fractional occupancies 53:47.

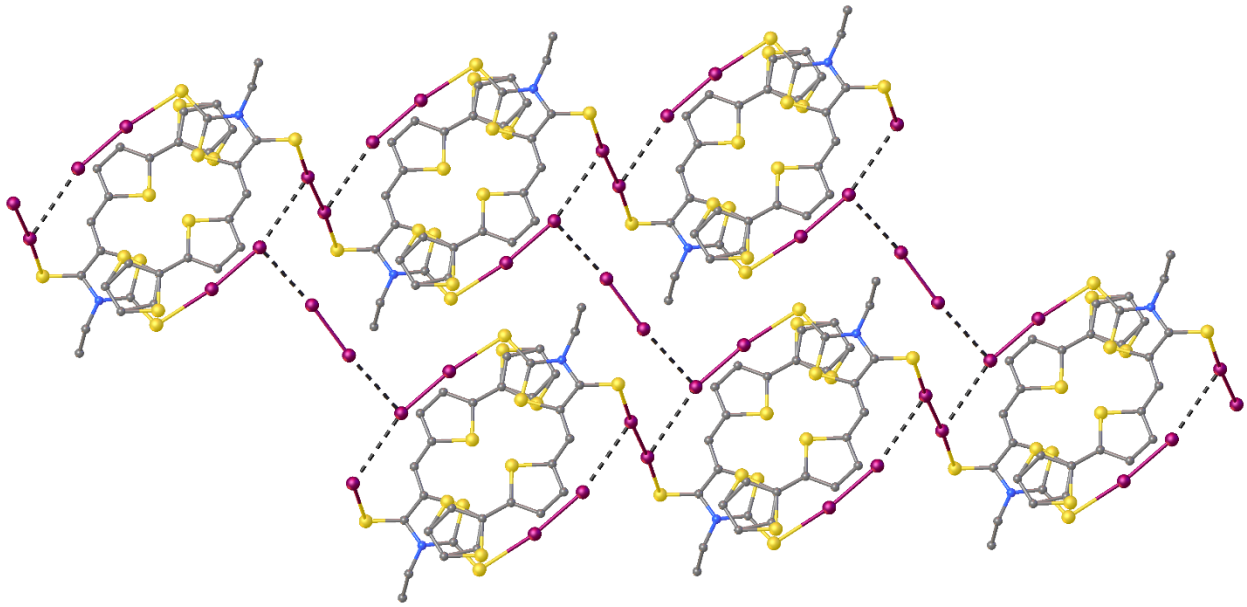


Figure 31. Portion of the crystal packing viewed along the *a*-axis.

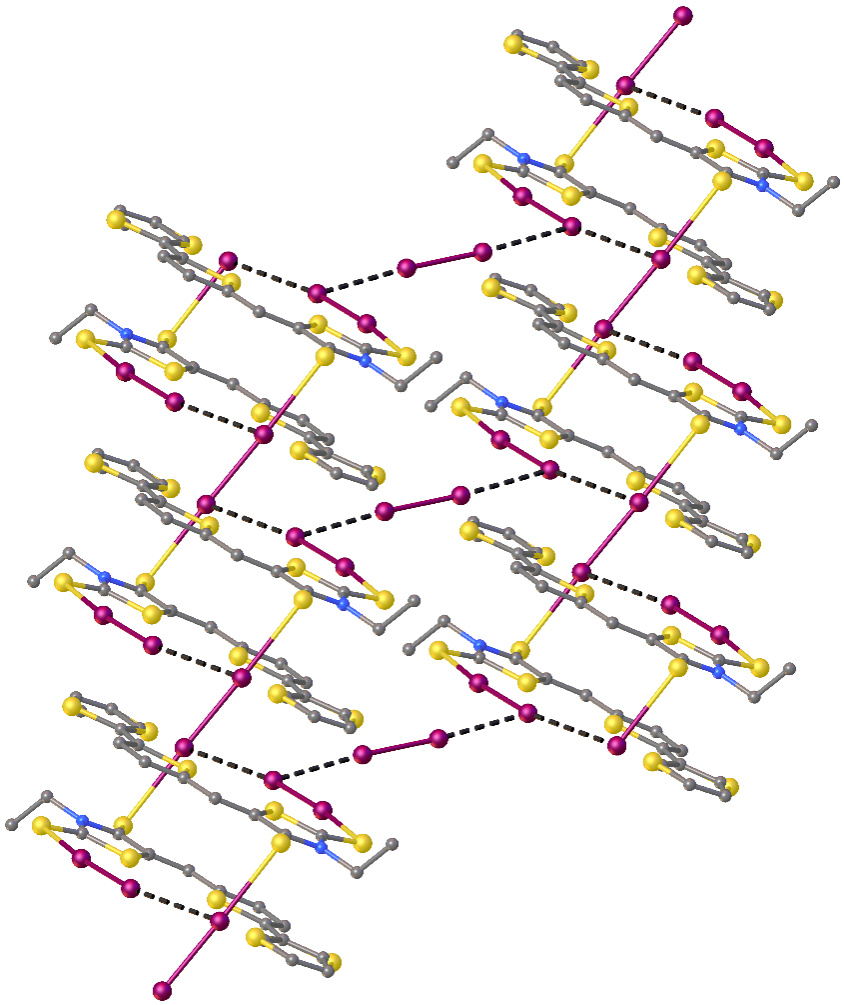


Figure 32. Supramolecular structure of **BTR-2S** illustrating the arrangement of iodine atoms through adjacent planes. The crystal packing is shown along the *c*-axis.

3.3.2.3. Raman Spectroscopy

Raman spectroscopy is a delicate method that yields insights into dihalogens, interhalogens, and (inter)polyhalides.[113] Specifically, in "spoke" I_2-adducts, the extension of the disrupted diiodine unit manifests in the reduced Raman peak associated with the I–I σg stretching vibration. Molecular iodine (bond order nI–I = 1) displays a distinctive peak at 214.5 cm^{-1} in the gas phase, attributed to the I–I stretching vibration.[114] This same vibration is observed in the range of 203–211 cm^{-1} in low-polarity organic solvents. Additionally, nearly monomeric I_2 confined in solid Kr exhibits a clear Raman band at 210.8 cm^{-1} at 32 K. Within crystalline I_2, where two molecular entities are incorporated in the unit cell, two vibrations are noted, designated to the synchronous (Ag, 180 cm^{-1}) and asynchronous (B3g, 189 cm^{-1}) stretching modes. In solid-state I_2 at ambient temperature, typically only the former band is detected, indicating that I_2 is characterized by a singular Raman band. In molecular assemblies containing altered diiodine (nI–I < 1), the attenuation of the I–I bond results in a proportionally related shift of the Raman Ag band toward lower wavenumbers. Consequently, the Raman spectrum of **BTR•I_2** presents a sole peak at 155 cm^{-1}. The Raman shift (greater than 140 cm–1), coupled with the mild elongation of the I–I bond, categorizes **BTR•I_2** as a weak CT adduct (nI–I > 0.6; nS–I < 0.4).[115]

3.3.2.4. Computational Study

In order to better understand the reactivity of **BTR** towards diiiodine, a set of theoretical calculations were carried out involving both **BTR** and its 1:1 diiodine CT adduct. Based on comparative investigations reported previously,[116] the hybrid mPW1PW[117] functional was paralleled by Schäfer, Horn and Ahlrichs split valence basis set including polarization functions (SVP),[118] in the formulation by Weigend (Def2SVP)[119] for all atoms but iodine, for which the LANL08(d)[120] basis set including relativistic effective core potentials (RECPs) was adopted. During the past decades, the interaction of chalcogen donors towards diiodine has been described by using two apparently opposite descriptions. Traditionally, this interaction was interpreted based on an orbital-mixing model as a charge-transfer (CT) interaction between the Lewis base **L**, featuring a lone pair of electrons (LP) on the donor atom, and the diiodine Lewis acid, featuring a s* antibonding molecular orbital disposed along the I–I bond, so that the CT results in a lowering of the I–I bond order and an elongation of the bond as compared to that of unperturbed I_2. More recently, the same type of interactions has been considered governed by the anisotropy of electrostatic potential on the interacting halogen atom, whose charge depletion area (s-holes), disposed opposite to the I–I bond in I_2 would

orient the halogen towards more nucleophilic sites in the organic molecule, i.e. those displaying a more negative electrostatic potential. In this context, spoke adduct **L**·I_2 have been considered as the result of a halogen bond (XB)[121,122] interaction between the I_2 XB donor and the **L** acceptor.[123] Recent theoretical studies carried out often at DFT level have agreed that s-hole interactions result from different contributions. Energy decomposition analyses (EDAs) shown that the energy of σ-hole interactions can be decomposed into an electrostatic term and an MO-mixing term,[124,125] in addition to dispersion.[126]

Table 8. Selected natural charges Q (|e|) calculated at the optimized geometry for BTR and BTR•I2. Atom labelling scheme as in Figures 2a and 2b. Values are referred to the conformer with the thiophene rings in the periplanar conformation.

Q	BTR	BTR•I_2
O1	-0.591	-0.581
N1	-0.502	-0.491
S1	-0.064	-0.020
S2	0.374	0.417
S3	0.430	0.445
S4	0.430	0.439
I1	–	-0.028
I2	–	-0.183

The relative weigh of each contribution depends largely on the nature of the involved groups, so that the nature of σ-hole interactions spans from almost purely ionic, especially at longer distances, to largely covalent, in which case a three-body system, featuring complementary bond orders, can be envisaged.

With the aim to get an insight into the interaction between **BTR** and diiodine, DFT calculations were carried out on the isolated **BTR** and I_2 molecules, and the **BTR•I_2** "spoke" adduct. As described above, the crystal structure of **BTR** shows the terminal thiophene ring disordered over the two possible planar and antiperiplanar conformations. Both planar conformers were optimized in the gas phase showing a negligible total electronic energy difference (0.8 kcal·mol^{-1}), thus justifying the presence of both conformers in the crystal structure. In Table 8, a selection of the natural charges[127-129] *Q* calculated for **BTR** at the optimized geometry is reported. As expected, the oxygen atom features the most natural negative charge. While thiophene and the rhodanine endocyclic S-atoms are positively charged, the thiocarboxylic rhodanine sulfur atom features a small negative charge. Kohn-Sham (KS) HOMO and HOMO-1 calculated for **BTR**, very close in energy to each other (e = –6.344 and –6.542 eV, respectively) show a relevant contribution from the exocyclic S-atom. In particular, HOMO-1 is a 3*p* lone pair of electrons laying on the molecular plane. Therefore, the frontier MO composition and the Natural Population Analysis (NPA)[127-129] indicate the

exocyclic sulfur atom of the rhodanine ring as the preferred donor site towards I_2 in a CT approach. On the other hand, in Figure 35 the electrostatic potential calculated for **BTR**, mapped on the electron density, is depicted, clearly showing that the most negative electrostatic potential regions on the sulfur electron density are disposed on the molecular plane, in accordance with the structural data collected for **BTR•I₂**. Thus, the two limit views of MO interpretation and electrostatic potential map converge to the same result. Indeed, the regions on the sulfur atom showing the largest negative electrostatic potential coincide with those where the lobes of KS-HOMO-1 isosurfaces are located.

The geometry of the 1:1 "spoke" adduct **BTR•I₂** was successfully optimized, displaying the diiodine unit laying on the molecular plane, in agreement to the structural data discussed above. A very good agreement was found between calculated and experimental bond lengths and angles. In particular, the interaction between the thiocarbonyl rhodanine group and diiodine shows metric parameters (C=S, 1.661; S···I, 2.951; I–I, 2.780 Å; S···I–I, 173.2 °), close to those determined by single crystal X-ray diffraction analysis (see above). This notwithstanding, the optimized I–I bond distance is slightly longer than the experimental value (by 0.027 Å), suggesting a modest underestimation of the CT interaction. The moderate elongation of the I–I bond distance $d_{I–I}$ in the adduct as compared with that optimized at the same level of theory for I_2 ($\Delta d_{I–I}$ = 0.114 Å) indicates a weak nature of the interaction. The interaction energy in the "spoke" adduct associated with the orbital mixing and CT can be evaluated by means of a second order perturbation theory analysis of the Fock matrix in the Natural Bond Orbital basis calculated for BTR at the optimized geometry. This is achieved by examining all possible interactions between occupied (donor) NBOs and virtual (acceptor) non-Lewis NBOs and evaluating their interaction energy by means of the second order perturbation theory.[129] For each donor NBO (i) and acceptor NBO (j), the stabilization energy E_{CT} associated can be estimated as

$$E_{CT} = q_i \cdot F(I,j)/(e_j - e_i) \quad (4)$$

where q_i is the donor orbital occupancy, e_j and e_i are diagonal elements and $F(i,j)$ is the off-diagonal NBO Fock matrix element. In the case of **BTR•I₂**, the donor orbital is represented by the filled bonding NBO almost entirely (96.2%) localized on the exocyclic sulfur (i = 6) and the acceptor orbital by the antibonding NBO (j = 350), localized on the atoms I1 and I2 (54.10% and 45.90%, respectively) and antibonding with respect to the I–I bond. This interaction is calculated to be relatively small [E_{CT} = 31.4 kcal·mol^{-1}; $F(6,350) = 7.2 \cdot 10^{-2}$ a.u.; De = 0.20 a.u.). Accordingly, a NPA carried out on **BTR•I₂** at the optimized geometry (Table 1) reveals that the interaction led to a charge-transfer ΔQ_{CT} = 0.192 |e| from the organic donor

to the diiodine unit. The additional charge on I_2 is transferred in particular to the terminal iodine atom, which shows a remarkably negative natural charge (Q_I = –0.183 |e|). As a consequence of the CT, the I–I Wiberg bond[130] index in the I_2 unit is lowered to 0.793, i.e. slightly larger than the value calculated from structural data by means of Pauling's equation. This is in agreement with the weak adduct nature of the **BTR•I₂** adduct, evidenced by the optimized metric parameters (see above) and testified experimentally by Raman spectroscopy. The molecular electron density mapped on the density surface in **BTR•I₂** clearly shows, in accordance with the NPA, the most negative potential on the most electronegative oxygen atoms. Worthy of note, the terminal iodine atom in the adduct displays a distribution of the electrostatic potential pointing to a s-hole topology, in perfect agreement with the long XB interactions connecting the stacks of **BTR•I₂** in the solid state, responsible for the 3D lattice dimensionality.

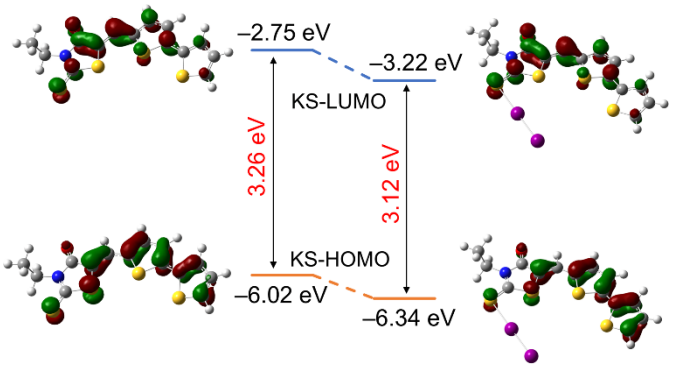


Figure 33. Kohn-Sham frontier orbitals energy levels for BTR (left) and BTR•I2 (right). Color: carbon, gray; nitrogen, blue; oxygen, red; sulfur, yellow; hydrogen, white. Cutoff value = 0.05 |e|.

Although theorem cannot be applied to Density Functional Theory, the Kohn-Sham eigenvalues can be considered useful parameters[131] in evaluating the variations in the HOMO-LUMO energy gap induced by the interaction of **BTR** with I_2. In fact, the gas-phase De_{HL} HOMO-LUMO energy gap is in good agreement with the band gap of a small π-conjugated compounds.[122,132] the case of **BTR** and **BTR•I₂** De_{HL} values of 3.26 and 3.12 eV are calculated (Figure 33), falling within the range -2.5 – -4.0 eV, typical of an small organic semiconductor.[132] It is noteworthy that the case of **BTR** clearly demonstrates how I_2-adduct formation can efficiently reduce the HOMO-LUMO energy gap in the resulting adducts compared to the pristine substrates. The case of study shows that this strategy holds not only when Lewis donors with a large Mulliken hardness are considered, as in the case of N-donors, but also when softer S-donors are considered, as in the case of **BTR**. Finally, a vibrational

analysis carried out on **BTR•I_2** confirms the attribution of the Raman peak at 155 cm^{-1} as due to the stretching of the perturbed I_2 unit. By adopting a scaling factor of 0.958,[133] a scaled wavenumber of 161 cm^{-1} is calculated, very close to the experimental value (see above).

The computational investigation on **BTR** and **BTR•I_2** was carried out at the DFT level by adopting the Gaussian 16 suite of programs. A preliminary validation of the computational setup was carried out by comparing selected optimised distances for **BTR** with the corresponding structural data. The mPW1PW functional[7] was adopted in combination with LANL08(d) basis sets (BSs) with Relativistic Effective Core Potentials (RECPs) on the heavier iodine species, and by adopting Def2-SVP BSs on the lighter elements (C, H, N, O, and S). Basis sets were obtained from Basis Set Exchange and Basis Set EMSL Library. The memory required for each calculation was evaluated by the GaussMem cross-platform (Linux, macOS, Windows) program as a function of the number of shared processors, the total number of basis set functions, and a memory threshold depending on the highest angular momentum basis function. The molecular geometry optimizations were performed starting from the available structural data (Table 9-14). The nature of the minima of each optimized geometry was verified by harmonic frequency calculations. In the case of **BTR**, two different geometries were optimised, corresponding to the periplanar and antiperiplanar conformation of the bithiophene moiety. Charge distributions and Wiberg bond indices were evaluated at the NBO level at the optimized geometries. The program GaussView 6.0.16 was used to investigate the optimised structures, the isosurfaces of Kohn–Sham molecular orbitals, and the MEP maps.

Table 9. Optimized geometry calculated for compound **BTR** at DFT level [mPW1PW//def2-SVP/LANL08(d)] in the gas phase in orthogonal Cartesian coordinate format (periplanar conformer).

Center Number	Atomic Number	Atomic Type	Coordinates (Angstroms) X	Y	Z
1	16	0	2.231022	6.973133	5.825206
2	16	0	3.952281	9.399969	5.630503
3	16	0	0.637490	4.244181	5.151760
4	16	0	0.893183	2.232430	2.544005
5	8	0	1.331941	7.647986	9.489364
6	7	0	2.591033	8.585239	7.808853
7	6	0	2.965571	8.429262	6.502965
8	6	0	1.423349	6.595333	7.330976
9	6	0	1.734828	7.619398	8.350494
10	6	0	3.030283	9.709028	8.626250
11	1	0	4.059166	9.941342	8.320635
12	1	0	3.033337	9.345292	9.661839
13	6	0	0.613568	5.548801	7.630289
14	1	0	0.238133	5.554225	8.658489
15	6	0	-0.263365	2.771605	5.017522
16	6	0	2.133889	10.926569	8.483017
17	1	0	2.125135	11.286284	7.445311
18	1	0	2.507768	11.738785	9.121827
19	1	0	1.104998	10.697392	8.792341
20	6	0	0.183800	4.457092	6.817784
21	6	0	-0.307574	2.023798	3.780289
22	6	0	0.145127	1.068413	1.531631
23	1	0	0.573500	0.840303	0.557985
24	6	0	-0.972926	0.529917	2.114553
25	1	0	-1.592683	-0.226898	1.635191
26	6	0	-0.647319	3.420178	7.221417
27	1	0	-1.047987	3.358633	8.232991
28	6	0	-0.896144	2.473490	6.214438
29	1	0	-1.501763	1.579499	6.353885
30	6	0	-1.234747	1.074208	3.396066
31	1	0	-2.089361	0.797919	4.012158

Table 10. Optimized geometry calculated for compound **BTR** at DFT level [mPW1PW//def2-SVP/LANL08(d)] in the gas phase in orthogonal Cartesian coordinate format (antiperiplanar conformer).

Center Number	Atomic Number	Coordinates (Angstroms) X	Y	Z
1	16	2.544743	5.652302	1.103449
2	16	2.951428	8.488095	1.929296
3	16	3.009963	2.530037	0.426965
4	16	4.295246	-1.598879	-0.311517
5	8	-1.183354	6.175199	0.385523
6	7	0.631982	7.385036	1.112933
7	6	1.967298	7.295936	1.392825
8	6	0.958124	5.107306	0.605136
9	6	-0.009190	6.223140	0.666850
10	6	-0.119901	8.626668	1.243528
11	1	0.293908	9.159208	2.110214
12	1	-1.154478	8.330921	1.460190
13	6	0.562421	3.872683	0.204795
14	1	-0.499071	3.805687	-0.053880
15	6	3.038139	0.849342	0.009377
16	6	-0.053731	9.488669	-0.005070
17	1	0.982273	9.778826	-0.226019
18	1	-0.639229	10.406069	0.146982
19	1	-0.471157	8.959235	-0.872406
20	6	1.311516	2.665656	0.072550
21	6	4.263119	0.089128	0.097327
22	6	5.970654	-1.716066	0.035683
23	1	6.483964	-2.667819	-0.083743
24	6	6.491152	-0.517160	0.448530
25	1	7.537346	-0.378363	0.717913
26	6	0.812698	1.440640	-0.349877
27	1	-0.232988	1.302641	-0.623505
28	6	1.779484	0.422853	-0.385722
29	1	1.573353	-0.602545	-0.691626
30	6	5.519698	0.513350	0.484242
31	1	5.732249	1.539526	0.784586

Table 11. Optimized geometry calculated for compound **BTR•I_2** at DFT level [mPW1PW//def2-SVP/LANL08(d)] in the gas phase in orthogonal Cartesian coordinate format.

Center Number	Atomic Number	Coordinates (Angstroms) X	Y	Z
1	53	4.252388	8.044883	3.083485
2	53	4.449911	6.783650	0.614151
3	16	2.248162	6.936160	5.869865
4	16	4.020507	9.359673	5.715268
5	16	0.643274	4.249703	5.170463
6	16	0.885422	2.310456	2.531065
7	8	1.288938	7.676148	9.512090
8	7	2.596167	8.565132	7.837842
9	6	2.979674	8.371574	6.552016
10	6	1.402712	6.594279	7.368067
11	6	1.705412	7.615394	8.381308
12	6	3.038200	9.692848	8.652506
13	1	4.086654	9.889932	8.390567
14	1	2.991333	9.342568	9.691530
15	6	0.570352	5.555482	7.644862
16	1	0.167216	5.567028	8.662707
17	6	-0.268366	2.787904	5.017386
18	6	2.179932	10.930985	8.460804
19	1	2.209402	11.278259	7.419282
20	1	2.556849	11.741401	9.099629
21	1	1.136925	10.733664	8.742911
22	6	0.150866	4.470786	6.824927
23	6	-0.286725	2.039073	3.782268
24	6	0.183972	1.111949	1.529332
25	1	0.612501	0.906552	0.550609
26	6	-0.899832	0.516496	2.123913
27	1	-1.485891	-0.270063	1.650377
28	6	-0.701468	3.441231	7.210612
29	1	-1.128030	3.385418	8.211975
30	6	-0.934928	2.497456	6.201117
31	1	-1.555340	1.611827	6.326416
32	6	-1.171500	1.043937	3.408737
33	1	-2.001547	0.720916	4.035568

Table 12. Natural population analysis for compound **BTR** at the DFT-optimized geometry [mPW1PW//def2-SVP/LANL08(d)] in the gas phase (periplanar conformation).

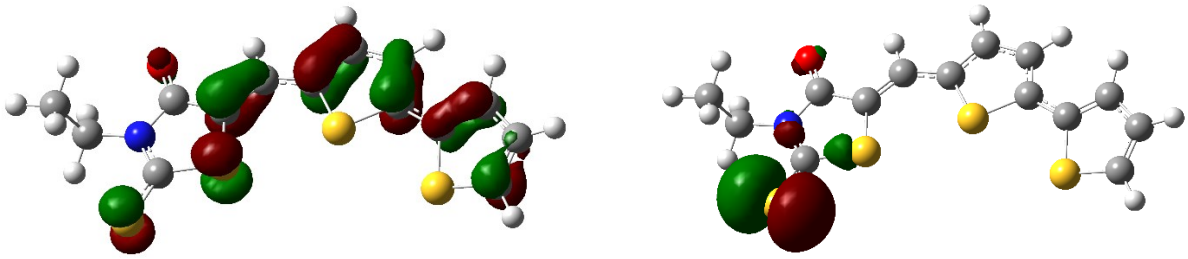
		Natural				
Atom	No	Charge	Core	Valence	Rydberg	Total
S	1	0.37430	9.99880	5.58953	0.03736	15.62570
S	2	-0.06373	9.99898	6.03426	0.03049	16.06373
S	3	0.43049	9.99875	5.53564	0.03511	15.56951
S	4	0.43011	9.99880	5.53357	0.03751	15.56989
O	5	-0.59126	1.99972	6.58148	0.01006	8.59126
N	6	-0.50180	1.99891	5.48861	0.01428	7.50180
C	7	-0.08982	1.99929	4.04850	0.04202	6.08982
C	8	-0.30131	1.99887	4.28054	0.02190	6.30131
C	9	0.71454	1.99911	3.23654	0.04982	5.28546
C	10	-0.22573	1.99918	4.20651	0.02004	6.22573
H	11	0.24301	0.00000	0.75203	0.00495	0.75699
H	12	0.24526	0.00000	0.75027	0.00447	0.75474
C	13	-0.18033	1.99885	4.15717	0.02431	6.18033
H	14	0.26710	0.00000	0.72828	0.00462	0.73290
C	15	-0.19710	1.99891	4.17306	0.02512	6.19710
C	16	-0.65046	1.99925	4.64377	0.00745	6.65046
H	17	0.22925	0.00000	0.76744	0.00331	0.77075
H	18	0.23016	0.00000	0.76771	0.00213	0.76984
H	19	0.22534	0.00000	0.77201	0.00265	0.77466
C	20	-0.23455	1.99892	4.21464	0.02100	6.23455
C	21	-0.23794	1.99890	4.21399	0.02506	6.23794
C	22	-0.39950	1.99903	4.38164	0.01884	6.39950
H	23	0.25646	0.00000	0.74172	0.00183	0.74354
C	24	-0.26476	1.99890	4.25003	0.01583	6.26476
H	25	0.24467	0.00000	0.75293	0.00239	0.75533
C	26	-0.20730	1.99885	4.19206	0.01639	6.20730
H	27	0.24677	0.00000	0.75091	0.00233	0.75323
C	28	-0.24554	1.99884	4.23052	0.01618	6.24554
H	29	0.24609	0.00000	0.75152	0.00240	0.75391
C	30	-0.23449	1.99885	4.21967	0.01598	6.23449
H	31	0.24208	0.00000	0.75551	0.00241	0.75792

Table 13. Natural population analysis for compound **BTR** at the DFT-optimized geometry [mPW1PW//def2-SVP/LANL08(d)] in the gas phase (antiperiplanar conformation).

		Natural				
Atom	No	Charge	Core	Valence	Rydberg	Total
S	1	0.37268	9.99880	5.59117	0.03735	15.62732
S	2	-0.06479	9.99898	6.03533	0.03048	16.06479
S	3	0.42754	9.99876	5.53884	0.03486	15.57246
S	4	0.42348	9.99880	5.54044	0.03727	15.57652
O	5	-0.59105	1.99972	6.58126	0.01006	8.59105
N	6	-0.50171	1.99891	5.48851	0.01428	7.50171
C	7	-0.08951	1.99929	4.04821	0.04200	6.08951
C	8	-0.30142	1.99887	4.28067	0.02189	6.30142
C	9	0.71432	1.99911	3.23677	0.04981	5.28568
C	10	-0.22573	1.99918	4.20652	0.02004	6.22573
H	11	0.24299	0.00000	0.75206	0.00495	0.75701
H	12	0.24536	0.00000	0.75016	0.00447	0.75464
C	13	-0.18026	1.99885	4.15713	0.02428	6.18026
H	14	0.26731	0.00000	0.72808	0.00461	0.73269
C	15	-0.19489	1.99890	4.17124	0.02474	6.19489
C	16	-0.65048	1.99925	4.64378	0.00745	6.65048
H	17	0.22921	0.00000	0.76749	0.00331	0.77079
H	18	0.23023	0.00000	0.76764	0.00213	0.76977
H	19	0.22539	0.00000	0.77196	0.00265	0.77461
C	20	-0.23268	1.99891	4.21286	0.02091	6.23268
C	21	-0.23514	1.99889	4.21154	0.02471	6.23514
C	22	-0.39722	1.99903	4.37956	0.01863	6.39722
H	23	0.25617	0.00000	0.74200	0.00184	0.74383
C	24	-0.26327	1.99890	4.24831	0.01605	6.26327
H	25	0.24571	0.00000	0.75192	0.00237	0.75429
C	26	-0.20623	1.99886	4.19076	0.01661	6.20623
H	27	0.24719	0.00000	0.75049	0.00232	0.75281
C	28	-0.25034	1.99885	4.23580	0.01568	6.25034
H	29	0.24816	0.00000	0.74931	0.00253	0.75184
C	30	-0.23715	1.99885	4.22275	0.01555	6.23715
H	31	0.24612	0.00000	0.75138	0.00251	0.75388

Table 14. Natural population analysis for compound **BTR•I_2** at the DFT-optimized geometry [mPW1PW//def2-SVP/LANL08(d)] in the gas phase.

		Natural				
Atom	No	Charge	Core	Valence	Rydberg	Total
I	1	-0.02827	46.00000	7.00783	0.02044	53.02827
I	2	-0.18357	46.00000	7.16704	0.01653	53.18357
S	3	0.41732	9.99877	5.54593	0.03798	15.58268
S	4	-0.01991	9.99895	5.98685	0.03411	16.01991
S	5	0.43943	9.99875	5.52671	0.03512	15.56057
S	6	0.44506	9.99880	5.51843	0.03771	15.55494
O	7	-0.58101	1.99972	6.57116	0.01013	8.58101
N	8	-0.49155	1.99891	5.47842	0.01422	7.49155
C	9	-0.05883	1.99926	4.02185	0.03772	6.05883
C	10	-0.31447	1.99886	4.29356	0.02204	6.31447
C	11	0.71211	1.99910	3.23881	0.04999	5.28789
C	12	-0.22863	1.99918	4.20974	0.01972	6.22863
H	13	0.24304	0.00000	0.75279	0.00417	0.75696
H	14	0.25118	0.00000	0.74432	0.00450	0.74882
C	15	-0.15853	1.99885	4.13544	0.02424	6.15853
H	16	0.26894	0.00000	0.72655	0.00452	0.73106
C	17	-0.18308	1.99892	4.15898	0.02518	6.18308
C	18	-0.65200	1.99925	4.64516	0.00760	6.65200
H	19	0.23036	0.00000	0.76666	0.00298	0.76964
H	20	0.23469	0.00000	0.76321	0.00210	0.76531
H	21	0.22827	0.00000	0.76913	0.00260	0.77173
C	22	-0.24429	1.99892	4.22447	0.02091	6.24429
C	23	-0.24484	1.99890	4.22077	0.02518	6.24484
C	24	-0.39133	1.99903	4.37337	0.01893	6.39133
H	25	0.25949	0.00000	0.73869	0.00182	0.74051
C	26	-0.26543	1.99890	4.25068	0.01584	6.26543
H	27	0.24638	0.00000	0.75124	0.00238	0.75362
C	28	-0.19445	1.99886	4.17915	0.01644	6.19445
H	29	0.24835	0.00000	0.74933	0.00232	0.75165
C	30	-0.24790	1.99885	4.23286	0.01619	6.24790
H	31	0.24805	0.00000	0.74957	0.00238	0.75195
C	32	-0.22658	1.99885	4.21176	0.01596	6.22658
H	33	0.24200	0.00000	0.75558	0.00241	0.75800



(a) (b)

Figure 34. Isosurfaces of KS-HOMO (a) and KS-HOMO-1 calculated for **BTR** at DFT level (periplanar conformer). Color: carbon, gray; nitrogen, blue; oxygen, red; sulfur, yellow; hydrogen, white. Cutoff value 0.05 |e|.

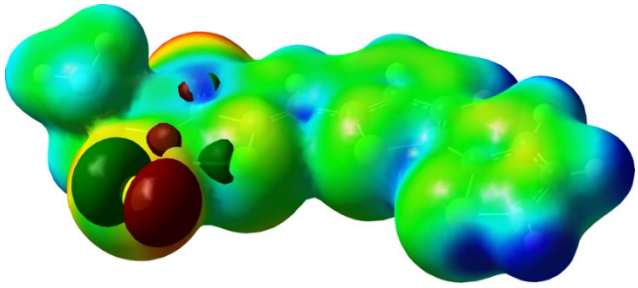


Figure 35. Superimposed molecular electrostatic potential mapped on the electron density ($5 \cdot 10^{-3}$ |e|·Bohr^{-3}) for the periplanar conformer of compound BTR [a; range –0.05 (red) to +0.06 (blue) a.u.] and KS-HOMO-1 isosurface (cutoff value = 0.05 |e|).

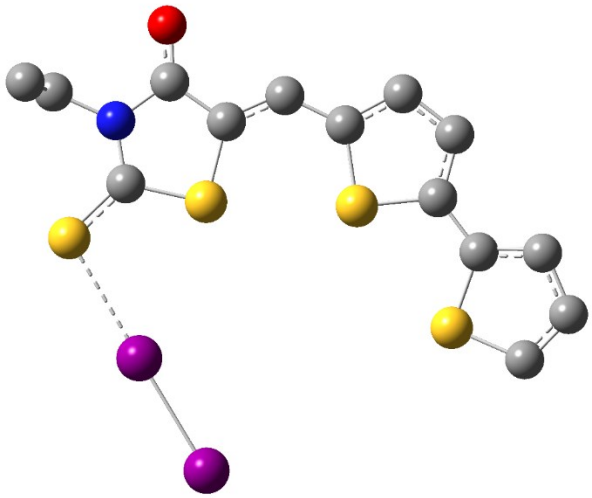


Figure 36. Ball and stick representation of the 1:1 "spoke" adduct BTR·I_2 optimized at DFT level in the periplanar conformation. Color: carbon, gray; nitrogen, blue; oxygen, red; sulfur, yellow; hydrogen, white. Hydrogen atoms were omitted for clarity.

3.3.2.5. Single Crystal Electrical Characterization

To investigate the influence of molecular arrangement, triggered by thiocarbonyl-diiodine bonds, on the electrical transport capabilities of the bulk substance, we constructed single crystal junction device. Crystals of **BTR•I_2** and **BTR** were meticulously positioned atop a glass base coated with a pair of gold contacts. Each crystal was arranged to span the two contacts, and a spot of conductive silver adhesive was utilized at each crystal-conductor interface, ensuring enhanced stability of the electrical linkage (Figure 37). The outcomes of the electrical evaluations are depicted in Figure 5b. The depicted graphs distinctly show that the **BTR•I_2** complex exhibits improved conductivity compared to the unmodified **BTR** crystals. It is critical to highlight that the gap between the two contacts remained unchanged across both device variants, and that the crystals were selectively chosen to match in geometric proportions, namely width and depth. The enhanced electric flow in the complexes could indicate that the molecules have adopted a more favorable alignment for charge movement, while simultaneously diiodine may have contributed to the generation of charge carriers within the crystal. It is significant to note that diiodine remained stationary during the application of electric flow, as the conductivity measure remains constant over duration.

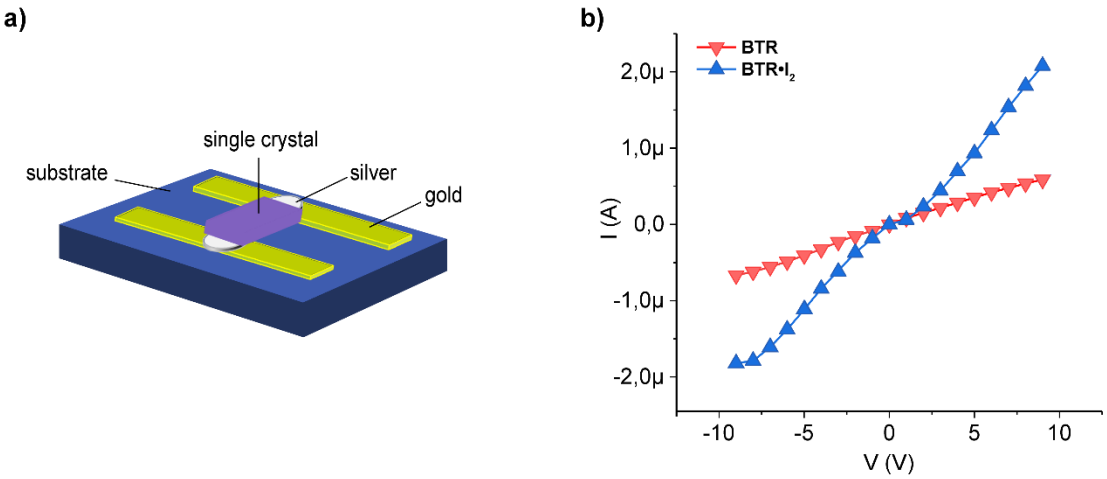


Figure 37. (a) Device architecture for single-crystal electrical characterization. (b) Current-voltage plot of **BTR** (blue) and of **BTR•I_2** (red).

3.3.3. Experimental Details

3.3.3.1. Crystal Growth and Characterization

The crystals adduct were obtained using two methods.

Method A: Sublimation of iodine vapour in solvent containing **BTR** led to the obtainment of Compound **BTR·I_2** and **BTR-2S·I_2** using hexane as a solvent.

Method B: A solution of diiodine in hexane was added dropwise to a solution of the **BTR** in hexane. **BTR** and dihalogen solutions were combined in 5:1 molar ratios **[X_2]:[BTR]**. Subsequently, crystals were grown for 4-5 days at room temperature. The obtained crystals were separated from the solvent and analyzed.

Compound **BTR·I_2** was obtained by both **Method A** and **Method B**. M.p. 154 °C. IR (2000–400 cm^{-1}): 509, 796, 1116, 1229, 1318, 1507, 1698, 1867, 2348.

Compound **BTR-2S·I_2.** M.p. 133 °C. IR (2000–400 cm^{-1}): 706, 791, 874, 1160, 1307, 1425, 1512, 1549.

Crystals of Compound **BTR** were obtained through crystallization in ethanol.

Crystal data parameters for compounds **BTR**, **BTR·I_2** and **BTR_2S·I_2** are reported in the following tables.

Table 15. Crystals data parameters for **BTR**, **BTR·I_2** and **BTR_2S·I_2.**

Compound	**BTR**	**BTR·I_2**	**BTR-2S·I_2**
Empirical formula	$C_{14}H_{11}NOS_4$	$C_{14}H_{11}I_2NOS_4$	$C_{14}H_{11}I_4NS_5$
Formula weight/g mol^{-1}	337.48	591.28	861.18
Crystal system	monoclinic	Triclinic	triclinic
Space group	$P2_1/c$	$P\bar{1}$	$P\bar{1}$
a/Å	6.1277(5)	8.9908(9)	7.6598(7)
b/Å	29.436(2)	10.5236(10)	11.7936(12)
c/Å	7.9018(7)	11.0589(11)	12.9268(13)
α/°	90	108.366(3)	88.217(4)
β/°	93.267(3)	106.358(4)	80.121(4)
γ/°	90	98.198(4)	84.695(4)
V/$Å^3$	1423.0(2)	921.59(16)	1145.38

Table 16. Bond lengths (Å) for compound **BRT**.

S5–C11	1.656(7)	C15–C11	1.410(11)
S5–C13	1.567(6)	C15–C14	1.577(15)
S3–C7	1.734(2)	C7–C8	1.372(3)
S3–C10	1.726(2)	C7–C6	1.426(3)
S2–C3	1.748(2)	C2–C3	1.470(3)
S2–C1	1.746(2)	C3–C6	1.349(3)
S1–C1	1.632(2)	C9–C8	1.398(3)
S4–C11	1.695(3)	C9–C10	1.373(3)
S4–C14	1.632(3)	C11–C12	1.399(12)
O1–C2	1.210(2)	C11–C10	1.442(3)
N1–C2	1.398(2)	C4–C5	1.510(3)
N1–C1	1.365(3)	C14–C13	1.347(3)
N1–C4	1.464(2)	C13–C12	1.469(14)

Table 17. Bond angles (°) for compound **BRT**.

C13–S5–C11	94.6(4)	N1–C1–S2	110.67(14)
C10–S3–C7	92.24(10)	N1–C1–S1	127.18(16)
C1–S2–C3	92.40(10)	C15–C11–S5	112.0(6)
C14–S4–C11	93.47(14)	C15–C11–C10	125.7(6)
C2–N1–C4	120.57(16)	C12–C11–S4	110.2(6)
C1–N1–C2	116.90(17)	C12–C11–C10	128.0(6)
C1–N1–C4	122.52(16)	C10–C11–S5	122.3(2)
C11–C15–C14	108.3(8)	C10–C11–S4	121.76(16)
C8–C7–S3	110.12(15)	C7–C8–C9	113.73(18)
C8–C7–C6	127.10(19)	N1–C4–C5	111.68(17)
C6–C7–S3	122.78(15)	C13–C14–S4	115.73(18)
O1–C2–N1	123.10(19)	C13–C14–C15	105.0(4)
O1–C2–C3	127.00(18)	C14–C13–S5	119.9(3)
N1–C2–C3	109.90(17)	C14–C13–C12	109.2(5)
C2–C3–S2	110.09(14)	C11–C12–C13	111.3(9)
C6–C3–S2	128.15(16)	C3–C6–C7	128.70(19)
C6–C3–C2	121.76(18)	C9–C10–S3	110.59(15)
C10–C9–C8	113.31(19)	C9–C10–C11	129.51(19)
S1–C1–S2	122.15(12)	C11–C10–S3	119.85(15)

Table 18. Bond lengths (Å) for compound **BRT·I_2**.

I1–I2	2.8057(3)	C3–C6	1.354(2)
I1–S1	2.7576(5)	C4–C5	1.521(3)
S2–C1	1.7305(17)	C6–C7	1.424(2)
S2–C3	1.7510(17)	C10–C11	1.447(2)
S1–C1	1.6657(17)	C10–C9	1.374(2)
S3–C10	1.7270(17)	C7–C8	1.382(2)
S3–C7	1.7333(17)	C11–S4A	1.7215(19)
S4B–C11	1.675(12)	C11–C12A	1.381(9)
S4B–C13	1.542(13)	C11–C12B	1.43(2)
O1–C2	1.210(2)	C13–C14	1.361(3)
N1–C1	1.349(2)	C13–C12A	1.402(11)
N1–C2	1.410(2)	C14–S4A	1.688(2)
N1–C4	1.471(2)	C14–C12B	1.54(3)
C3–C2	1.463(2)	C8–C9	1.400(3)

Table 19. Bond angles (°) for compound **BRT·I_2**.

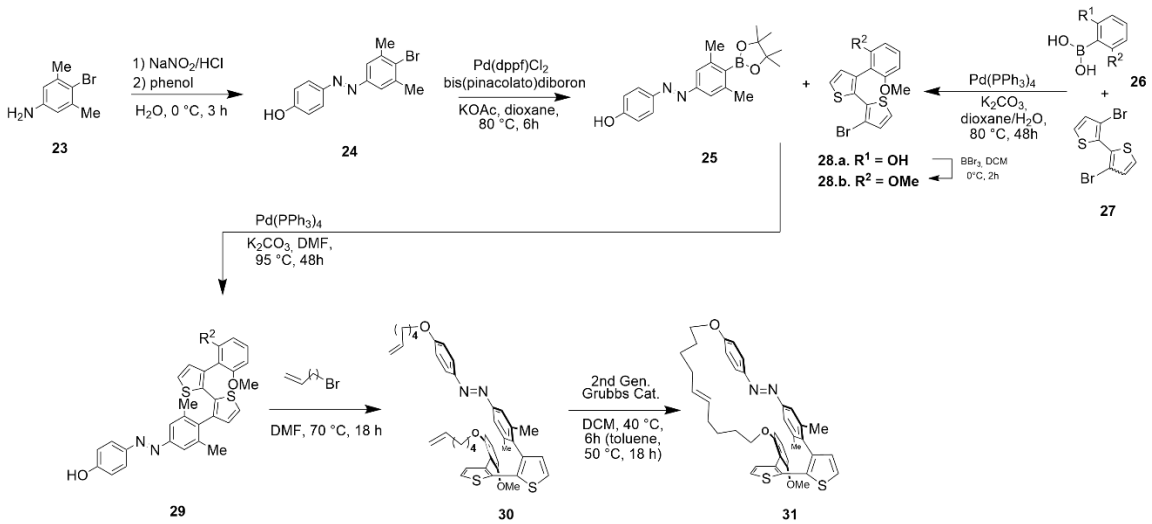
S1–I1–I2	174.695(10)	C9–C10–S3	110.86(13)
C1–S2–C3	91.66(8)	C9–C10–C11	129.06(16)
C1–S1–I1	104.27(6)	C6–C7–S3	124.14(13)
C10–S3–C7	92.13(8)	C8–C7–S3	110.32(13)
C13–S4B–C11	93.1(5)	C8–C7–C6	125.53(16)
C1–N1–C2	115.98(14)	C10–C11–S4B	122.8(4)
C1–N1–C4	123.31(14)	C10–C11–S4A	119.50(13)
C2–N1–C4	120.70(14)	C12A–C11–C10	130.9(4)
S1–C1–S2	123.68(10)	C12A–C11–S4A	109.6(4)
N1–C1–S2	112.32(12)	C12B–C11–S4B	109.9(12)
N1–C1–S1	124.00(13)	C12B–C11–C10	127.3(10)
C2–C3–S2	110.44(12)	C14–C13–S4B	123.9(4)
C6–C3–S2	127.85(14)	C14–C13–C12A	110.8(3)
C6–C3–C2	121.70(16)	C13–C14–S4A	113.48(14)
O1–C2–N1	122.45(16)	C13–C14–C12B	101.8(7)
O1–C2–C3	127.97(16)	C7–C8–C9	113.36(16)
N1–C2–C3	109.58(14)	C10–C9–C8	113.34(16)
N1–C4–C5	111.59(15)	C14–S4A–C11	91.91(9)
C3–C6–C7	129.27(16)	C11–C12A–C13	114.2(5)
C11–C10–S3	120.08(13)	C11–C12B–C14	111.3(14)

Reproduced from Sanna A.L., Acca S., Podda E., Pintus A., Aragoni M.C., Lippolis V., Ricci P.C., Cosseddu P., Arca M., Sforazzini G., Unveiling the significance of adduct formation between thiocarbonyl Lewis donors and diiodine for the structural organization of rhodanine-based small molecule semiconductors, *J. Mater. Chem. C*, 2024, Advance Article with permission from the Royal Society of Chemistry.

Link to the published article https://doi.org/10.1039/D4TC01791A.

4. Photochromic Torsional Switch

In the previous chapters, strategies for optimal tuning were discussed, both through intramolecular units in the macromolecule PTS and through the use of supramolecular interactions to facilitate precise molecular arrangements in the solid state. In this section, the synthetic pathway for obtaining PTS, shown in Scheme 7, will be presented. The synthesis of photo-switches involved an azo-coupling between the diazonium salts of an aniline derivative and phenol to obtain hydroxyazobenzene and subsequent introduction of a pinacol-boronic ester group. Significant quantities of the thiophene precursor were synthesized starting from palladium-catalyzed coupling between commercial dibromobithiophene and dimethoxyphenylboronic acid. The product of the coupling reaction was then selectively dealkylated in one of the two ethers to yield the corresponding hydroxide. The coupling reaction between this last compound and the hydroxyazobenzene with the pinacolic ester provided the base unit of the PTS molecule, consisting of the union of bithiophenic and azobenzene precursors. Through subsequent alkylation reactions, the two hydroxides present in the molecule were selectively functionalized with alkyl chains consisting of 5 and 6 carbon atoms. This macromolecule was subjected to a cyclization between the olefinic group anchored on the bithiophene dimer and that present on the azobenzene via Grubbs metathesis reactions.



Scheme 7. PTS Synthetic path.

5. Conclusions

In the present thesis work, two possible approaches aimed at tuning the properties of the final organic semiconductor have been investigated.

On one hand, the choice was made to investigate the insertion of intramolecular photosensitive units - specifically azobenzene - evaluating the structure-property relationships as the substituent groups vary. In this regard, our study rationally designed azobenzene derivatives functionalized at their meta positions with electron-directing substituents, unveiling the influence of these groups on the azobenzene's spectroscopic characteristics and isomerization kinetics. We observed that both electron-donating and electron-withdrawing groups situated at these strategic locations significantly modulate the absorption spectra of the *E* and *Z* isomers of azobenzene. In comparison to a reference azobenzene, which includes two methyl groups at its meta positions, the presence of methoxy (**OMe**) groups results in only modest modifications to the spectral profiles, mirroring those of the methylated compound. Conversely, the incorporation of electron-withdrawing groups (**CO_2Me**) leads to a notable bathochromic shift in the high-energy π-π* band of the *E* isomer by 11 nm and an even more pronounced 21 nm shift in the π-π* band of its *Z* counterpart.

Furthermore, our findings elucidate that the thermal relaxation process *Z* → *E* isomer is marginally influenced by methoxy groups, necessitating slightly longer durations for back-isomerization compared to methyl-substituted azobenzenes. In contrast, azobenzenes functionalized with carbonyl groups require significantly extended periods - exceeding an additional day - for this transition, which underscores the pronounced effect of electron-withdrawing functionalities. Despite these variations, the half-life ($\tau_{1/2}$) of the thermal relaxation for all studied azobenzenes occurs within a relatively narrow timeframe, with approximately 1 hour of difference, ranging from 8.5 to 9.5 hours.

The integration of computational and experimental methodologies in our investigation not only corroborates the impact of meta-positioned substituents on the azobenzene's electronic structure but also enhances our comprehension of their role in stabilizing the *Z* and *E* isomers, especially for those derivatives bearing electron-withdrawing carbonyl groups. This approach has afforded valuable insights into the structure-property relationship of *meta*-substituted azobenzenes, particularly underscoring the ability to carefully modulate the optical and thermal characteristics of azobenzene through targeted functionalization.

Our research significantly enriches the toolkit for designing functional materials, offering avenues to precisely control and predict the photoresponsive properties of molecular switches. This advancement in understanding the nuanced effects of electron-directing substituents at the *meta* position on

azobenzene's behavior opens new possibilities for the development of efficient and versatile molecular switches, providing to the intricate requirements of next-generation functional materials.

The second approach centered on the use of supramolecular interactions to control the solid-state packing interactions within thiophene-based materials.

Regarding hydrogen-bond interactions, our study outlines a synthetic strategy specifically designed to achieve a hydrogen-bond-driven supramolecular structure. We successfully synthesized a modified P3EHT polymer, which incorporates hydrogen-bonding sites, enabling precise supramolecular interactions. This achievement marks a significant step towards harnessing the structural properties necessary for enhanced material performance. Looking forward, further investigations will be pivotal to characterize the properties of the synthesized material and to confirm its potential applications. These efforts will extend our understanding of hydrogen-bonding interactions in polymeric systems and could lead to novel applications in organic electronics and beyond. Such exploration remains essential for advancing the field and optimizing the functional attributes of these complex molecular architectures.

Additionally, we have introduced a novel method to control the molecular arrangement of rhodanine-containing π-conjugated molecules. Our research indicates that diiodine can establish a stable adduct through interaction with the rhodanine thiocarbonyl group. Preliminary investigations into the electrical conductivity of single crystals imply that the molecular configuration in **BTR•I_2** contributes to an increased electrical current flow. Thus, we can draw the following conclusions: i) The diiodine adduct shows a decrease in the HOMO-LUMO energy gap relative to the unmodified compound. ii) FT-Raman spectroscopy serves as an efficient and rapid non-invasive technique to identify the coordination of diiodine and is therefore applicable in semiconductors to confirm adduct formation in the absence of single crystal X-ray diffraction analysis, especially when dealing with amorphous materials.
The case study of **BTR/BTR•I_2** illustrates the impact of integrating chalcocarbonyl groups into π-conjugated derivatives to create supramolecular structures based on XB/ChB interactions that enhance the dimensionality of their lattice, decrease the HOMO-LUMO energy gap, and ultimately augment their semiconducting properties.
These findings lay the groundwork for the development of novel processing techniques that can be directly applied to SM semiconductors, aiding in the production of optoelectronic devices.

6. Synthetic Procedures and NMR Spectra

Materials and Methods

All solvents and reagents were used as commercially supplied, without further purification. All the solvents (dichloromethane, ethyl acetate, chloroform, methanol, acetic acid, petroleum ether 40-60 °C, 1,2-dichloroethane, THF) were purchased from Carlo Erba Reagents. Iodomethane, $POCl_3$ (99%), 2-ethylhexylbromide, magnesium turnings, 3-bromothiophene, N-bromosuccinimide, LiCl, *t*-BuMgCl, $Ni(dppp)Cl_2$, *n*BuLi (1.6M in hexane), $NaBH_4$, Glycine tertbutylester hydrochloride, diisopropylethylamine, acetylalanylalanine, trifluoroacetic acid (TFA) were purchased from Sigma Aldrich; dimethylformamide (DMF, 99.0%), 3,5-Dimethylaniline, PyBOP, Lawesson reagent were purchased from Fluorchem; concentrated hydrochloric acid 37%, phenol, $NaNO_2$, NaOH, K_2CO_3, 2,2'-bithiophene (99%), sodium acetate (99.0%); piperidine (99+%) and sodium sulfate (99+%, anhydrous), magnesium sulfate anhydrous were purchased from Carlo Erba Reagents; 3,5-Dimethoxylaniline was purchased from ABCR and dimethyl 5-aminoisophthalate, 3-ethylrhodanine (98.0%) and I_2 were purchased from TCI.

Reactions were monitored by thin-layer chromatography (TLC) performed on alugram precoated silica sheets, 0.2 mm plates, and compounds were visualized under UV light (254 nm or 365 nm), depending on the substrate. Column chromatography was performed on silica gel 60A (particle size 40 – 63 μm, Carlo Erba) using positive air pressure. ^{1}H and ^{13}C liquid NMR spectra were recorded on a Bruker Advance III HD 600 MHz NMR spectrometer at 298 K. Deuterated chloroform-*d* ($CDCl_3$), deuterated tetrachloroethane-d_2 (TCE-d_2) and deuterated dimethylsulfoxide-*d6* (DMSO-*d6*) were used for preparing the NMR sample. $CDCl_3$ was purchased from Carlo Erba Reagents, TCE-d_2 and DMSO-*d6* were purchased from TCI . Chemical shifts (δH and δC) are expressed in parts per million (ppm) relative to the residual solvent peak and, for proton NMR, shown as follows: chemical shift, multiplicity (s = singlet, d = doublet, t = triplet, q = quartet, m = multiplet, bs = broad singlet), coupling constant (J, Hz) and integration. Mass analyses were performed using a Exploris 240 LC/GC-Orbitrap FTMS mass spectrometer. IR measurements were recorded using a JASCO FTIR-4XLE spectrometer (ATR mode). Melting points were determined in capillaries on a FALC apparatus mod. C (up to 290 °C) melting point apparatus. Elemental analyses were performed with a CHN PE 2400 series II elemental analyzer (T = 925 °C).

X-ray Diffraction Measurements

X-ray single-crystal diffraction data for **BTR**, **BTR•I_2** and **BTR-2S•I_2** were collected at 100 K on a Bruker D8 Venture diffractometer equipped with a PHOTON II detector. The structures were solved with the ShelXT[3] solution program using dual methods, and the models were refined with ShelXL 2018/3[4] using full-matrix least-squares minimization on F^2. Olex2 1.5[5] was used as the graphical interface. Hydrogen atom positions were calculated geometrically and refined using the riding model.

Raman Spectroscopy

FT-Raman spectra were recorded at room temperature in the 80–2600 cm^{-1} range on spectrometer SolInstrument MS750 series fitted with a laser CoherentOndaX LMseries and operating with an excitation frequency of 785 nm.

Synthetic procedures of Compounds in Chapter 2

Compound AB-OH.Me, (E)-4-((3,5-dimethylphenyl)diazenyl)phenol (1)

This compound was synthesized as reported in literature. Concentrated hydrochloric acid (2.0 mL) was added to a suspension of 3,5-dimethylaniline **Ph-NH$_2$.Me** (0.606 g, 5.00 mmol, 1.0 eq) in water (20.0 mL). The mixture was cooled to 0 °C in an ice bath and stirred vigorously. A solution of $NaNO_2$ (0.380 g, 5.50 mmol, 1.1 eq) in water (3.0 ml) was then added dropwise to the cooled suspension, and the mixture was stirred for 1h. In a separate flask, NaOH 5.0 M (0.999 g, 25.0 mmol, 5.0 eq) was added to a solution of phenol (0.565 g, 6.00 mmol, 1.2 eq) in water (2.0 mL), and cooled to 0 °C. The former mixture was then slowly transferred to the solution of phenol and vigorously stirred for 1h at 0 °C. The resultant precipitate was filtered with vacuo and purified by silica chromatography (dichloromethane / ethyl acetate 9.5:0.5) to give an orange powder (0.404 g, 35.7 %). ^{1}H NMR (600 MHz, $CDCl_3$): δ = 7.86 (d, *J* = 8.8 Hz, 2H), 7.49 (s, 2H), 7.09 (s, 1H), 6.94 (d, *J* = 8.8 Hz, 2H), 5.08 (s, 1H, OH), 2.41 (s, 6H). ^{13}C NMR (151 MHz, $CDCl_3$): δ = 158.2, 153.1, 147.5, 138.8, 132.3, 125.0, 120.5, 115.9, 21.5. HRMS (ESI, positive mode) *m*/*z* calculated for $C_{14}H_{15}N_2O$ $[M + H]^+$: 227.1174; found: 227.1179.[61]

Compound AB-OH.OMe, (E)-4-((3,5-dimethoxyphenyl)diazenyl)phenol (2)

Concentrated hydrochloric acid (1.3 mL) was added to a suspension of 3,5-dimethoxyanline **Ph-NH$_2$.OMe** (0.500 g, 3.26 mmol, 1.0 eq) in tetrahydrofuran (5.0 mL). The mixture was cooled to 0 °C in an ice bath and stirred vigorously. A solution of $NaNO_2$ (0.247 g, 3.59 mmol, 1.1 eq) in 1.9 mL of water was then added dropwise to the cooled suspension, and the mixture was stirred for 1h. In a separate flask, NaOH 5M (0.652 g, 16.3 mmol, 5.0 eq) was added to a solution of phenol (0.368 g, 3.91 mmol, 1.2 eq) in 2.6 mL of water, and cooled to 0 °C. The former mixture was then slowly transferred to the solution of phenol and vigorously stirred for 1h at 0 °C. The reaction mixture was extracted with dichloromethane, the organic layers collected, dried over Na_2SO_4, filtered and solvent removed with vacuo. The crude product was purified by silica chromatography using a gradient eluent (dichloromethane 100 % → ethyl acetate 100 %) to obtain the desired product as a red dark powder (0.377 g, 44.8 %). ^{1}H NMR (600 MHz, $CDCl_3$) δ 7.88 (d, *J* = 8.8 Hz, 2H), 7.08 (s, 2H), 6.95 (d, *J* = 8.8 Hz, 2H), 6.57 (s, 1H), 5.17 (s, 1H, OH), 3.87 (s, 6H). ^{13}C NMR (151 MHz, $CDCl_3$) δ 161.2, 158.5, 154.7, 147.2, 125.2, 116.0, 103.6, 100.8, 55.7. HRMS (ESI, positive mode) *m*/*z* calculated for $C_{14}H_{15}N_2O_3$ $[M + H]^+$: 259.1083; found: 259.1082.[76]

Compound AB-OH.CO_2Me, (E)-dimethyl 5-((4-hydroxyphenyl)diazenyl)isophthalate (3)

This compound was synthesized adapting a literature procedure.[43] Concentrated hydrochloric acid (0.95 mL) was added to a suspension of dimethyl 5-aminoisophthalate **Ph-NH_2.CO_2Me** (0.500 g, 2.39 mmol, 1.0 eq) in tetrahydrofuran (5.0 mL). The mixture was cooled to 0 °C in an ice bath and stirred vigorously. A solution of $NaNO_2$ (0.182 g, 2.63 mmol, 1.1 eq) in 1.4 mL of water was then added dropwise to the cooled suspension, and the mixture was stirred for 1h. In a separate flask, NaOH 5M (0.476 g, 11.9 mmol, 5 eq) was added to a solution of phenol (0.270 g, 2.87 mmol, 1.2 eq) in 1.9 mL of water, and cooled to 0 °C. The former mixture was then slowly transferred to the solution of phenol and vigorously stirred for 1h at 0 °C . The reaction mixture was extracted with ethyl acetate, the organic layers collected, dried over Na_2SO_4, filtered and solvent removed with vacuo. The crude product was purified by silica chromatography using dichloromethane / ethyl acetate (9.5:0.5) as a eluent, to obtain the desired product as bright orange powder (0.515 g, 68.6 %). ^{1}H NMR (600 MHz, $CDCl_3$) δ = 8.75 (s, 1H), 8.70 (s, 2H), 7.94 (d, *J* = 8.5 Hz, 2H), 6.98 (d, *J* = 8.5 Hz, 2H), 5.32 (s, 1 H, OH), 4.00 (s, 6H). ^{13}C NMR (151 MHz, $CDCl_3$) δ = 166.1, 159.1, 153.0, 147.1, 131.9, 131.8, 127.7, 125.7, 116.1, 52.7. HRMS (ESI, positive mode) *m*/*z* calculated for $C_{16}H_{15}N_2O_5$ $[M + H]^+$: 315.0981; found: 315.0983. [76]

Compound AB.Me, (E)-1-(3,5-dimethylphenyl)-2-(4-methoxyphenyl)diazene (4)

A solution of compound **AB-OH.Me** (0.100 g, 0.442 mmol, 1.0 eq), iodomethane (0.033 mL, 0.530 mmol, 1.2 eq), K_2CO_3 (0.091 g, 0.663 mmol, 1.5 eq) and dimethylformamide (2.0 mL) was stirred at 70°C for 24 hrs. The mixture was allowed to reach room temperature, diluted with ethyl acetate, transferred in a separatory funnel, and washed with water. The organic layers were collected, dried over Na_2SO_4, filtered and concentrated in vacuo. The crude product was purified by silica chromatography (petroleum ether / ethyl acetate = 8:2) to obtain the desired product as a bright orange oil (0.088 g, 83.0 %). ^{1}H NMR (600 MHz, $CDCl_3$) δ 7.91 (d, *J* = 9.0 Hz, 2H), 7.50 (s, 2H), 7.09 (s, 1H), 7.02 (d, *J* = 9.0 Hz, 2H), 3.89 (s, 3H), 2.41 (s, 6H). ^{13}C NMR (151 MHz, $CDCl_3$) δ 162.1, 153.1, 147.2, 138.8, 132.2, 124.8, 120.5, 114.3, 55.7, 21.4. HRMS (ESI, positive mode) *m*/*z* calculated for $C_{15}H_{16}N_2O$ $[M + H]^+$: 241.1341; found: 241.1341.[76]

Compound AB.OMe, (E)-1-(3,5-dimethoxyphenyl)-2-(4-methoxyphenyl)diazene (5)

A solution of compound **AB-OH.OMe** (0.146 g, 0.566 mmol, 1.0 eq), iodomethane (0.042 mL, 0.680 mmol, 1.2 eq), K_2CO_3 (0.117 g, 0.849 mmol, 1.5 eq) and dimethylformamide (2.5 mL) was stirred at 70°C for 24 hrs. The mixture was allowed to reach room temperature, diluted with ethyl acetate, transferred in a separatory funnel, and washed with water. The organic layers were collected, dried over Na_2SO_4, filtered and concentrated in vacuo. The crude product was purified by silica chromatography (petroleum ether / ethyl acetate = 8:2) to obtain the desired product as a bright orange powder (0.084 g, 54.5 %). ^{1}H NMR (600 MHz, $CDCl_3$) δ 7.92 (d, *J* = 9.4 Hz, 2H), 7.09 (d, 2H), 7.03 (d, *J* = 9.4 Hz, 2H), 6.58 (s, 1H), 3.90 (s, 3H), 3.88 (s, 6H). ^{13}C NMR (151 MHz, $CDCl_3$) δ 162.3, 161.2, 154.8, 147.0, 125.0, 114.5, 103.5, 100.8, 55.7. HRMS (ESI, positive mode) *m*/*z* calculated for $C_{15}H_{16}N_2O_3$ $[M + H]^+$: 273.1239; found: 273.1238. [76]

Compound AB.CO_2Me, (E)-dimethyl 5-((4-methoxyphenyl)diazenyl)isophthalate (6)

A solution of compound **AB-OH.CO_2Me** (0.100 g, 0.318 mmol, 1.0 eq), iodomethane (0.024 mL, 0.382 mmol, 1.2 eq), K_2CO_3 (0.066 g, 0.477 mmol, 1.5 eq) and dimethylformamide (1.5 mL) was stirred at 70°C for 24 hrs. The mixture was allowed to reach room temperature, diluted with ethyl acetate, transferred in a separatory funnel, and washed with water. The organic layers were collected, dried over Na_2SO_4, filtered and concentrated in vacuo. The crude product was purified by silica chromatography (dichloromethane 100 %) to obtain the desired product as a bright yellow powder (0.033 g, 31.7 %). ^{1}H NMR (600 MHz, $CDCl_3$) δ = 8.75 (s, 1H), 8.70 (s, 1H), 7.98 (d, *J* = 8.7 Hz, 2H), 7.05 (d, *J* = 8.7 Hz, 2H), 3.99 (s, 6H), 3.91 (s, 3H). ^{13}C NMR (151 MHz, $CDCl_3$) δ = 166.0, 162.9, 153.0, 146.9, 131.8, 127.7, 125.4, 114.5, 55.8, 52.7. HRMS (ESI, positive mode) *m*/*z* calculated for $C_{17}H_{16}N_2O_5$ $[M + H]^+$: 329.1137; found: 329.1130. [76]

Synthetic procedures of Compounds in Chapter 3

Compound 3-ehtylhexylthiophene (8)

This compound was synthesized adapting a literature procedure.[134] To a mixture of magnesium turnings (4.011 g, 0.165 mol, 1.3 eq), anhydrous THF (15.75 mL), a solution of 2-ethylhexylbromide (32 g, 29.6 mL, 0.165 mol, 1.3 eq) in anhydrous THF (40.4 mL) was added slowly at 0 °C under N_2. After refluxing for 1 h, a solution of 3-bromothiophene (20 g, 11.5 mL, 0.122 mol) in anhydrous THF (40.0 mL) was added dropwise in the 250 mL flask through a dropping funnel. Then, Ni(dppp)Cl_2 (0.680 g, 1.25 mmol) was added at 0° C and the mixture stirred overnight at room temperature. The reaction was quenched by pouring cold HCl aq. (2.0 N) into the mixture. The product was extracted with $CHCl_3$ and dried over anhydrous $MgSO_4$. The crude product was further purified by column chromatography using hexane as the eluent to give a clear liquid (15.250 g, 63.7%). ^{1}H NMR (400 MHz, $CDCl_3$, 500 MHz): 7.23 (m, 1H), 6.91 (m, 2H), 2.57 (d, J = 6.7 Hz, 2H), 1.57 (m, 1H), 1.28 (m, 8H), 0.88 (m, 6H).

Compound 2,5-dibromo-3-(2-ethylhexyl)thiophene (9)

This compound was synthesized following a literature procedure.[135] NBS (13.56 g, 0.076 mol, 2.2 eq) was added portionwise to a stirring solution of 3-(2-ehtylhexyl)thiophene (6.8 g, 0.035 mol) in $CHCl_3$/acetic acid mixture (v/v:1/1, 200.0 mL) at 0° C. The solution was stirred for 24 hours and then quenched with water and sodium carbonate in order to remove succinimide. The mixture was extracted with $CHCl_3$, the organic layers collected and dried over $MgSO_4$, then filtered to obtain an orange liquid as the desired product (11.52 g, 93%). ^{1}H NMR (400 MHz, $CDCl_3$) δ 6.75 (s, 1H), 2.45 (m, 2H), 1.54 (m, 1H), 1.27 (m, 9H), 0.88 (m, 7H).

Compound P3EHT (10)

This compound was synthesized following a literature procedure.[136] All the glassware and the flask has been treated with 3 cycles of heatgun - vacuum - Ar before use. In a Schlenk flask LiCl was dried under vacuum at 150 °C overnight. 0.197 g of LiCl were poured into a 250 mL 3 neck flask in 10.0 mL of freshly distilled THF at room temperature. After complete solubilization of LiCl, 1.5 g of 2,5-dibromo-3-(2-ehtylhexyl)thiophene were added to the 3 neck flask through a syringe. Then, 4.66 ml of *t*-BuMgCl has been injected in the mixture through a syringe. After 4 h at 40 °C, 0.2 mL of the reacting mixture has been injected to the flask with Ni(dppp)Cl_2 (0.0174 g, 0.033 mmol) in 2.0 mL of distilled THF in order to active the catalyst. Then, 33.0 mL of THF were added to the 250 mL flask. Then, all the Ni mixture has been injected in the 250 mL flask and the mixture was stirred at room temperature for 3.5 days. The reaction was quenched with 23.0 mL of HCl 1.0 M and then precipitated

in methanol. A red solid powder was obtained at the bottom of the beaker. To further purify the crude mixture so obtained, a Soxhlet extraction was performed with subsequent cycles of MeOH, acetone and chloroform to obtain the polythiophene product (0.2169 g). ^{1}H NMR (400 MHz, $CDCl_3$) δ 7.68 (1 H in position 1 of the polythiophene at the termination of the polymer), 7.17 (1 H in position 5 of the polythiophene at the termination of the polymer), 6.94 (s, 1H), 2.73 (m, 2H), 1.70 (m, 1H), 1.36 – 1.24 (m, 8H), 0.89 (m, 6H). M_w = 10600, PDI = 1.59 (GPC relative to polystyrene standards). Characterization is consistent with literature data.

Compound H-P3EHT-H (11)

This compound was synthesized following a literature procedure.[137] Under Ar atmosphere dry THF (20.0 mL) was added to a flask with P3EHT **10** (0.2169 g). Then, excess of *t*-BuMgCl (3.0 mL) was added and the mixture stirred overnight at reflux. The reaction was quenched with water, acetic acid and sticky solid attached to the wall of the flask washed with methanol. Then the crude product was dissolved in DCM and solvent removed with rotavapor to obtain a sticky red solid (0.1575 g, 78%).

Compound CHO-P3EHT-CHO (12)

This compound was synthesized following a literature procedure.[138] To a solution of **Compound H-P3EHT-H 11** (0.1575 g, 0.017 mmol) in dry THF (10.0 mL) was added n-BuLi (1.6 M in hexane, 0.042 mL, 0.068 mmol, 4.0 eq) dropwise at -78 °C. After 2h, the mixture was removed from the cooling bath and DMF (0.0063 g, 0.086 mmol) was added and the reaction mixture stirred overnight at room temperature. The reaction was quenched with water and extracted with DCM, organic layer dried over $MgSO_4$ and filtered. Solvent was removed with rotavapor to obtain the desired product as an orange sticky solid (0.1256 g, 80%). ^{1}H NMR (400 MHz, TCE-d_2) δ 6.97 (s, 1H), 2.74 (s, 2H), 1.70 (m, 1H), 1.29 (m, 8H), 0.90 (m, 6H).

Compound OH-P3EHT-OH (13)

This compound was synthesized following a literature procedure.[139] **Compound CHO-P3EHT-CHO 12** (0.1256 g, 0.020 mmol), $NaBH_4$ (0.013 g, 0.052 mmol), THF (10.0 mL) were stirred at reflux overnight, under Ar atmosphere. Then, solvent was removed with rotavapor and the crude product washed with water. The mixture was extracted with DCM, organic layer dried over $MgSO_4$ and filtered. Solvent was removed with rotavapor to obtain the desired product as an orange sticky solid (0.120 g, 83%). ^{1}H NMR (400 MHz, TCE-d_2) δ 6.97 (s, 1H), 2.74 (m, 2H), 1.71 (m, 1H), 1.26 (m, 8H), 0.88 (m, 6H).

Compound tert-butyl acetylalanylalanylglycinate (16)

A solution of Glycine tertbutylester hydrochloride (0.829 g, 4.94 mmol), diisopropylammine (1.915 g, 14.82 mmol, 2.6 mL, 3.0 eq) were dissolved in 30.0 ml of THF at room temperature and stirred for 1h. After 1h, acetylalanylalanine (1.00 g, 4.94 mmol) and PyBOP (3.085 g, 5.93 mmol, 1.2 eq) were added and the mixture was stirred at room temperature overnight. The reaction was quenched with water to precipitate the product and then the water removed through a vacuum filtration to obtain the desired product a white powder (1.307 g, 92%). ^{1}H NMR (400 MHz, DMSO) δ 8.14 (bs, 1H), 8.03 (bs, 1H), 7.95 (bs, 1H), 4.28 (m, 2H), 3.72 (m, 2H), 1.40 (s, 9H), 1.20 (m, 9H).

Compound acetylalanylalanylglycine (17)

This compound was synthesized following a literature procedure.[140] A solution of **Compound 16** (1.200 g, 4.18 mmol) in $CHCl_3$ (25.0 mL) , trifluoroacetic acid (6.4 mL, 83.5 mmol, 20.0 eq) was stirred overnight at room temperature and then concentrated in vacuo to give the corresponding deprotected Compound 14 as a pale brown crystal solid in quantitative yield (1.658 g, 100%). ^{1}H NMR (400 MHz, $CDCl_3$) δ 10.90 (m, 1H), 7.67 (bs, 1H), 7.33 (bs, 1H), 7.22 (bs, 1H), 4.60 (m, 2H), 3.94 (m, 2H), 1.43 (m, 9H).

Compound tert-butyl (3,5-bis(isobutylcarbamoyl)benzoyl)glycinate (18)

A solution of Glycine tertbutylester hydrochloride (0.800 g, 4.77 mmol), diisopropyethyllammine (0.740 g, 5.73 mmol, 1.0 mL, 1.2 eq) were dissolved in 146 ml of THF at room temperature and stirred for 1h. After 1h, 3,5-bis(isobutylcarbamoyl)benzoic acid **15** (1.834 g, 5.73 mmol, 1.2 eq – previously synthetized in the hosting Laboratory at EPFL), PyBOP (4.22 g, 8.11 mmol, 1.7 eq) and diisopropyethylammine (0.801 g, 6.2 mmol, 1.1 mL) were added and the mixture was stirred at room temperature overnight. The reaction was quenched with water to precipitate the product and then the water removed through a vacuum filtration to obtain the desired product a white powder (1.905 g, 92%). %). ^{1}H NMR (400 MHz, $CDCl_3$) δ 8.29 (s, 3H), 7.03 (s, 1H), 6.39 (s, 2H), 4.15 (m, 2H), 3.50 (m, 4H), 1.69 (hept, J = 6.6 Hz, 2H), 1.51 (s, 9H), 0.97 (d, J = 6.6 Hz, 12H).

Compound (3,5-bis(isobutylcarbamoyl)benzoyl)glycine (19)

This compound was synthesized following a literature procedure.[140] A solution of **Compound 18** (1.905 g, 4.4 mmol) in $CHCl_3$ (10.0 mL) , trifluoroacetic acid (9.2 mL, 96.8 mmol, 22.0 eq) was stirred for 33 h at room temperature and then concentrated in vacuo to give the corresponding deprotected product as a pale brown crystal solid in quantitative yield (1.658 g, 100%). ^{1}H NMR (400

MHz, $CDCl_3$) δ 8.69 (s, 2H), 8.56 (s, 1H), 8.15 (bs, 1H), 7.15 (bs, 2H), 4.38 (m, 2H), 3.53 (m, 4H), 1.68 (m, 2H), 0.95 (m, 12H).

Compound 2,2'-bithiophene-5-carbaldehyde (BTA, 20)

This compound was synthesized adapting a literature procedure. A Vilsmeier reagent was prepared by stirring $POCl_3$ (0.5 mL, 6.02 mmol) and DMF (0.5 mL, 6.0 mmol) for 10 minutes and then added to an ice-cold solution of 2,2'-bithiophene (0.500 g, 3.01 mmol) in 1,2-dichloroethane (4.0 mL). The reaction mixture was heated to reflux for 24 h, hydrolyzed with saturated aqueous sodium acetate solution for 6 h, and extracted with dichloromethane (100 mL) three times. The organic layers were collected together, then dried over anhydrous sodium sulfate and filtered. The solvent was removed with vacuo to obtain the pure product as a yellow powder (0.580 g, 100 %). The product was used in the next step without further purification. ^{1}H NMR ($CDCl_3$) δ (ppm): 9.87 (s, 1 H), 7.67 (d, J = 3.9 Hz, 1 H), 7.36 (d, J = 4.4 Hz, 2 H), 7.25 (d, J = 3.9 Hz, 1 H), 7.08 (t, J = 4.4 Hz, 1 H). ^{13}C NMR (151 MHz, $CDCl_3$) δ (ppm) 182.6, 147.3, 141.8, 137.4, 136.1, 128.5, 127.2, 126.3, 124.4. The characterization of this compound is consistent with that found in the literature.

Compound (Z)-5-([2,2'-bithiophen]-5-ylmethylene)-3-ethyl-4-thioxothiazolidin-2-one (BTR, 21)

Piperidine (0.053 mL, 0.515 mmol) was added to a solution of compound **BTA** (0.200 g, 1.03 mmol) and 3-Ethyl-2-thioxo-1,3-thiazolidin-4-one (0.182 g, 2.00 mmol) in 20.0 mL of ethanol under Argon atmosphere. The reaction mixture was stirred at reflux for 24 h, then quenched with water and extracted with ethyl acetate (100 mL) three times. The organic layers were combined, dried with anhydrous sodium sulfate and filtered. The solvent was removed under reduced pressure and the crude product was purified by silica chromatography (DCM/Petroleum Ether = 6:4) to give a bright orange powder (0.346 g, 99.5 %). ^{1}H NMR (600 MHz, $CDCl_3$) δ (ppm): 7.83 (s, 1H), 7.34 (d, J = 4.9 Hz, 1H), 7.33 (d, J = 4.9 Hz, 2H), 7.24 (d, J = 3.9 Hz, 1H), 7.08 (t, J = 3.9 Hz, 1H), 4.18 (q, J = 7.1 Hz, 2H), 1.29 (t, J = 7.1 Hz, 3H). ^{13}C NMR (151 MHz, $CDCl_3$) δ (ppm): 192.1, 167.5, 145.6, 136.7, 136.3, 135.3, 128.5, 126.7, 125.6, 125.2, 125.2, 120.8, 40.1, 12.4. HRMS (ESI, positive mode) *m/z* calculated for $C_{14}H_{12}NOS_4$ [M + H]+ : 337.9802; found: 337.9788. Mp 164 °C. IR (2000–400 cm^{-1}): 507, 792, 1122, 1224, 1315, 1581, 1697, 1976, 2032, 2360.

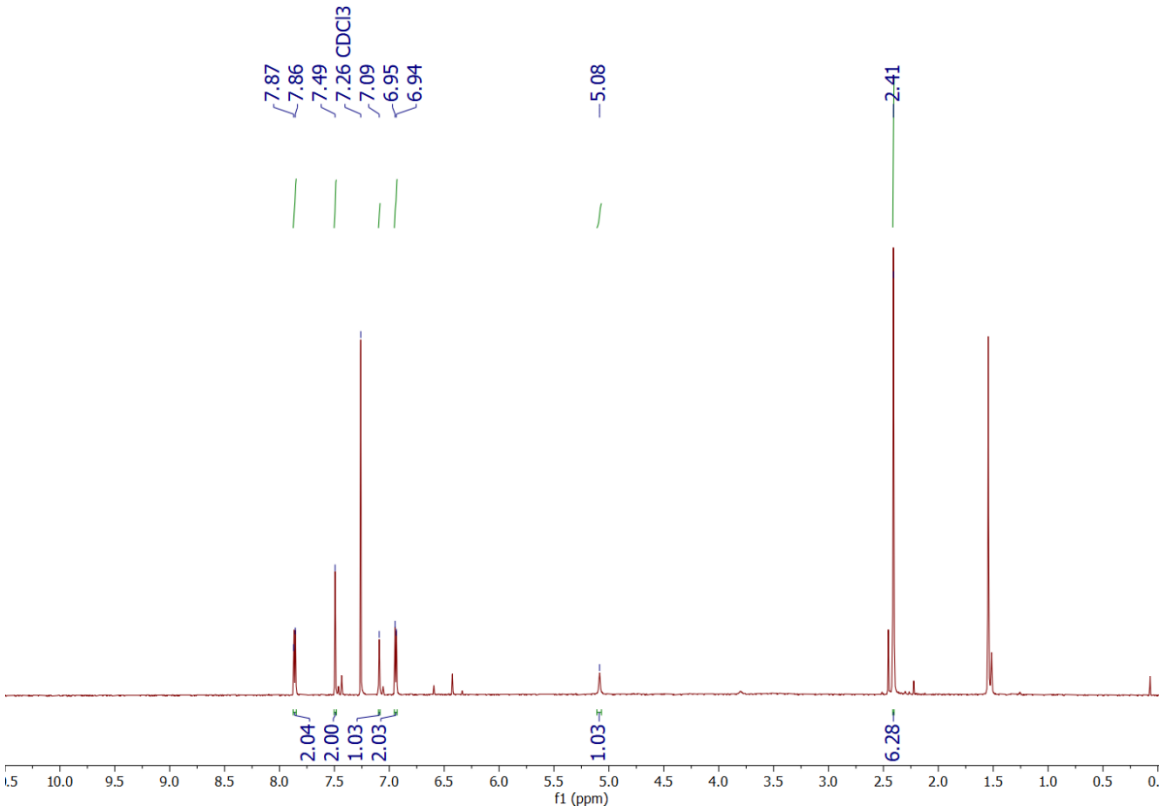
Compound (Z)-5-([2,2'-bithiophen]-5-ylmethylene)-3-ethylthiazolidine-2,4-dithione, (BTR-2S, 22)

A solution of Compound **BTR** (**20**) (0.100 g, 0.297 mmol) and Lawesson reagent (0.120 g, 0.296 mmol) in 6.0 mL of anhydrous toluene was stirred at reflux for 24 h under Argon atmosphere, then

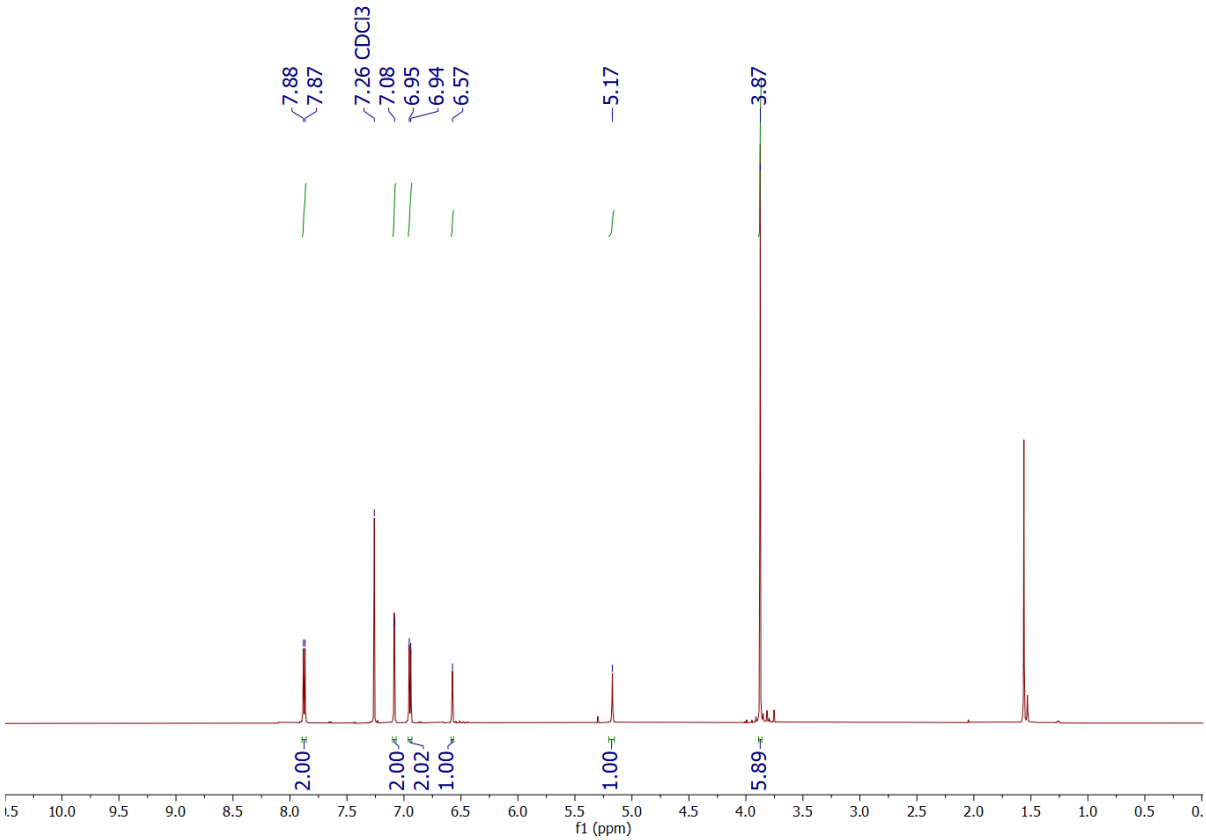
quenched with water and extracted with ethyl acetate (100 mL) three times. The organic layers were combined, dried with anhydrous sodium sulfate and filtered. The solvent was removed under reduced pressure and the crude product was purified by silica chromatography (DCM/Petroleum Ether = 6:4) to give a dark purple powder (0.068 g, 65 %). ^{1}H NMR (600 MHz, $CDCl_3$) δ (ppm): 8.16 (s, 1H), 7.45-7.44 (d, 1H), 7.38-7.36 (m, 2H), 7.25 (s, 1H), 7.09 (t, 1H), 4.66-4.62 (s, 2H), 1.34-1.31 (d, 3H). ^{13}C NMR (151 MHz, $CDCl_3$) δ (ppm): 194.4, 192.4, 146.3, 137.9, 137.0, 136.3, 130.1, 128.7, 128.2, 127.1, 125.9, 125.5, 44.6, 11.4. HRMS (ESI, positive mode) *m/z* calculated for $C_{14}H_{12}NS_5$ [M + H]+ : 353.9573; found: 353.9570. Mp 150 °C. IR (2000–50 cm^{-1}): 512, 698, 787, 1120, 1202, 1306, 1428, 1523, 1565.

^{1}H NMR Spectra in Chapter 2

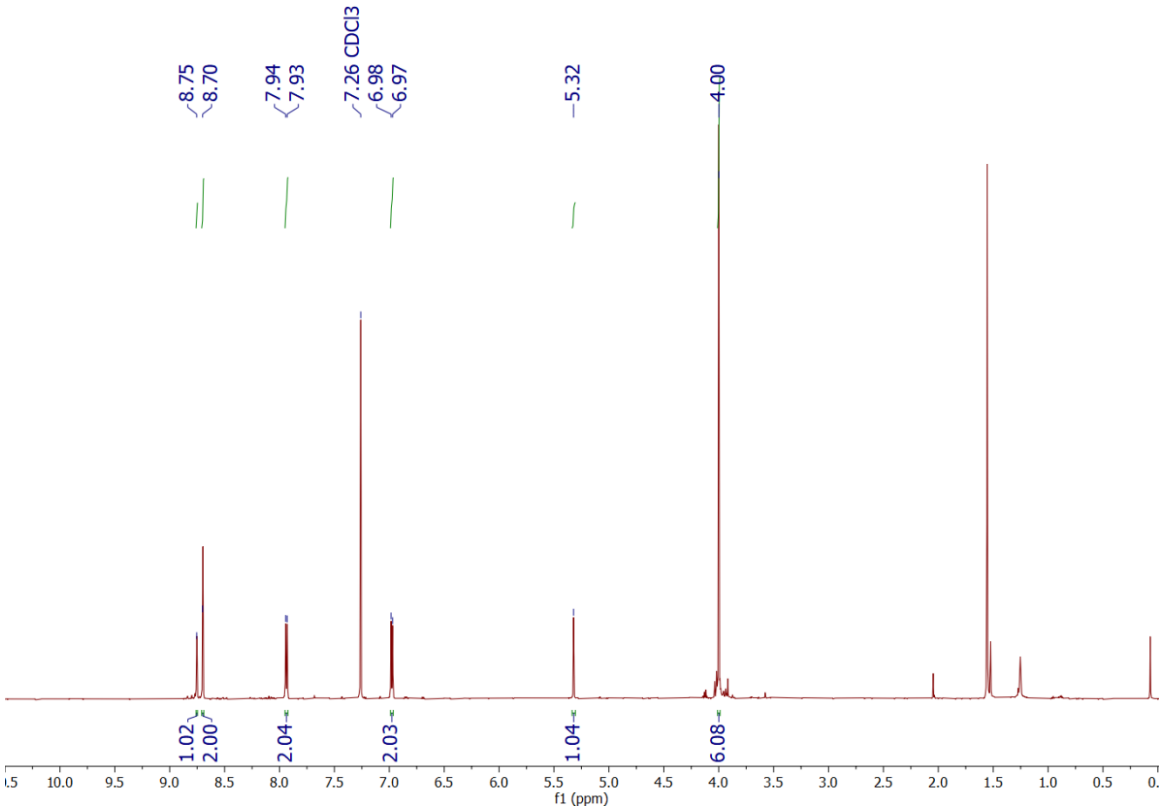
Compound AB-OH.Me



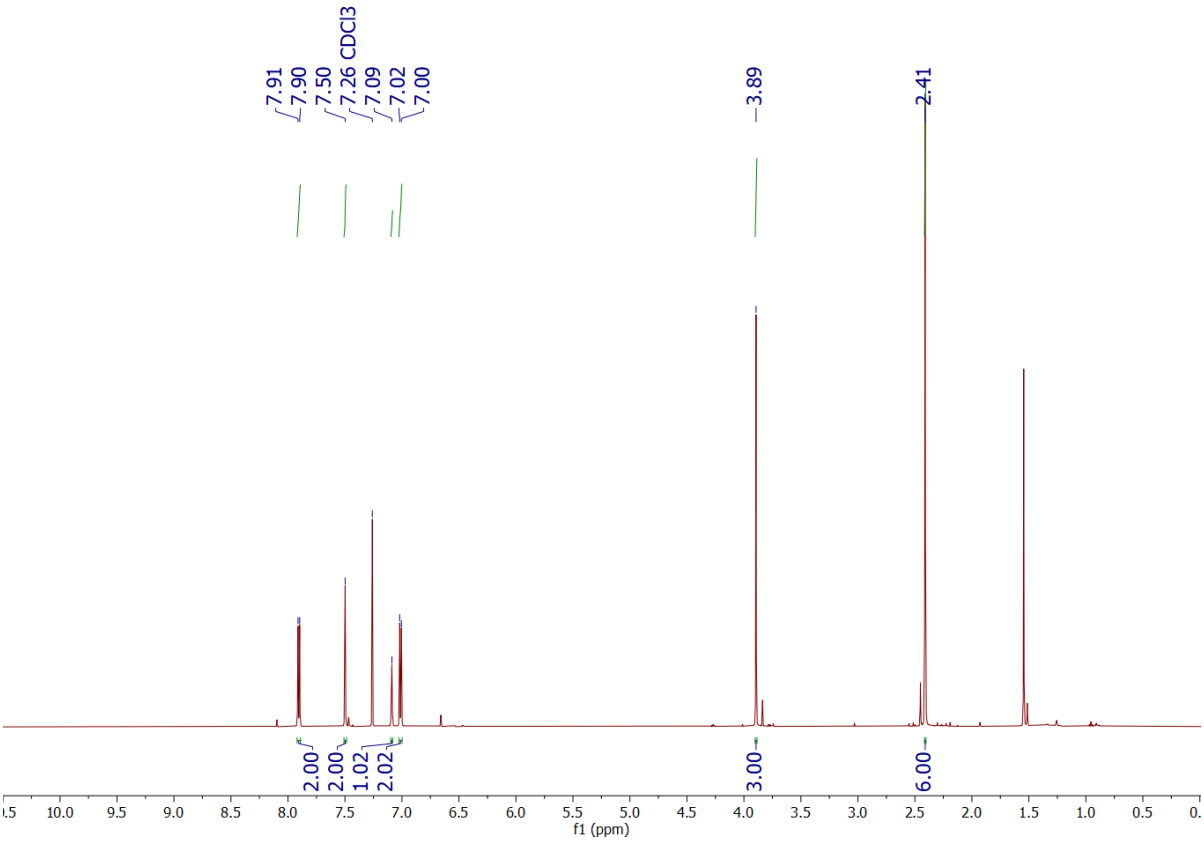
Compound AB-OH.OMe



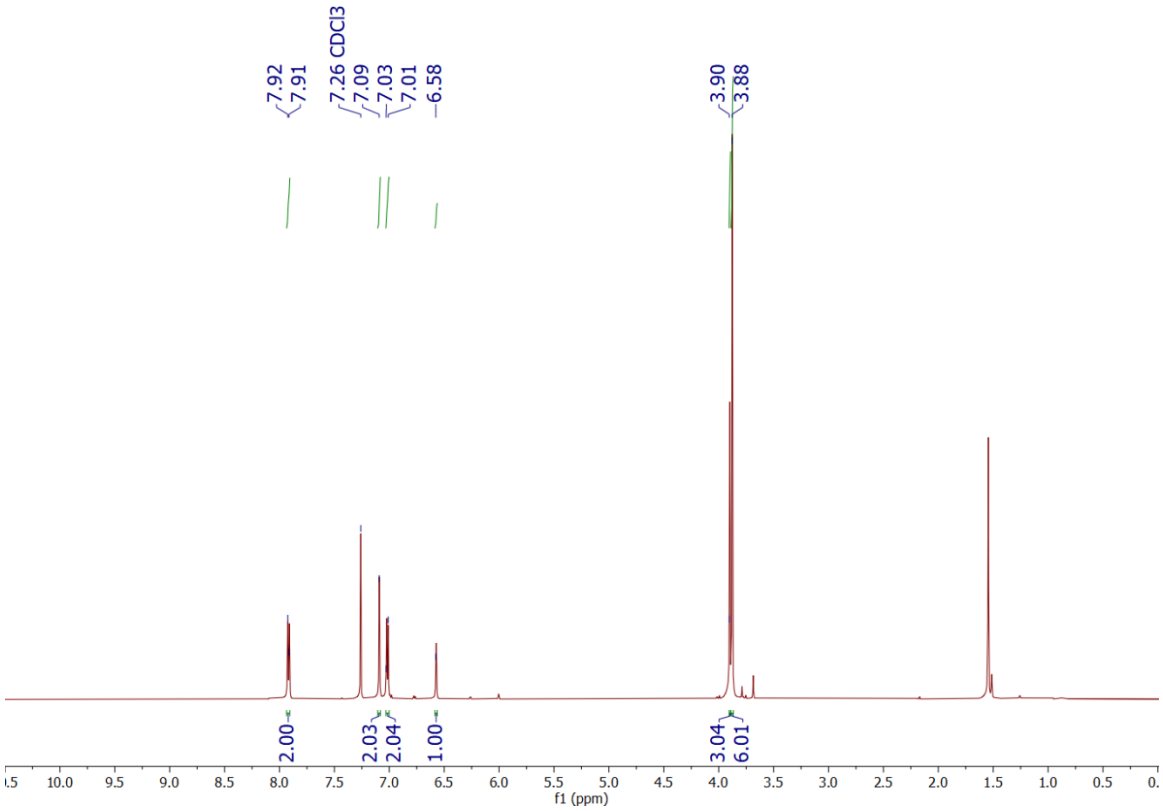
Compound AB-OH.CO_2Me



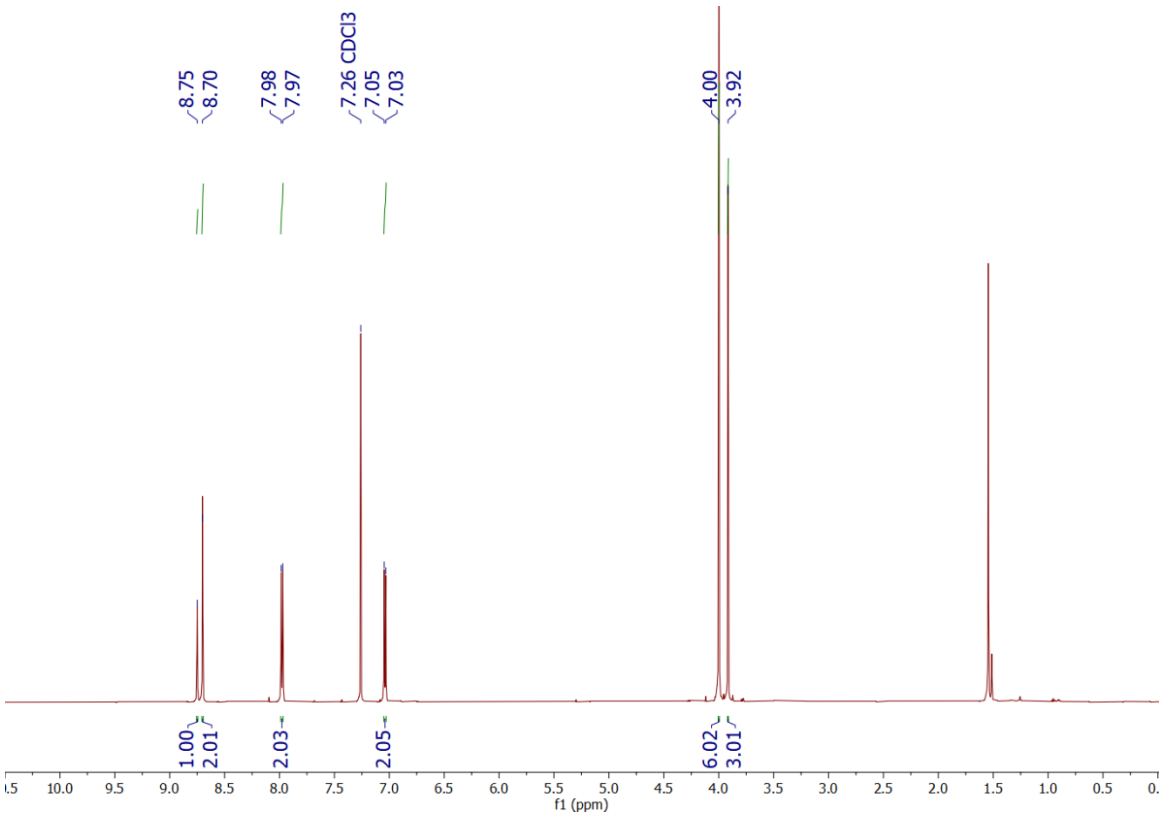
Compound AB.Me



Compound AB.OMe

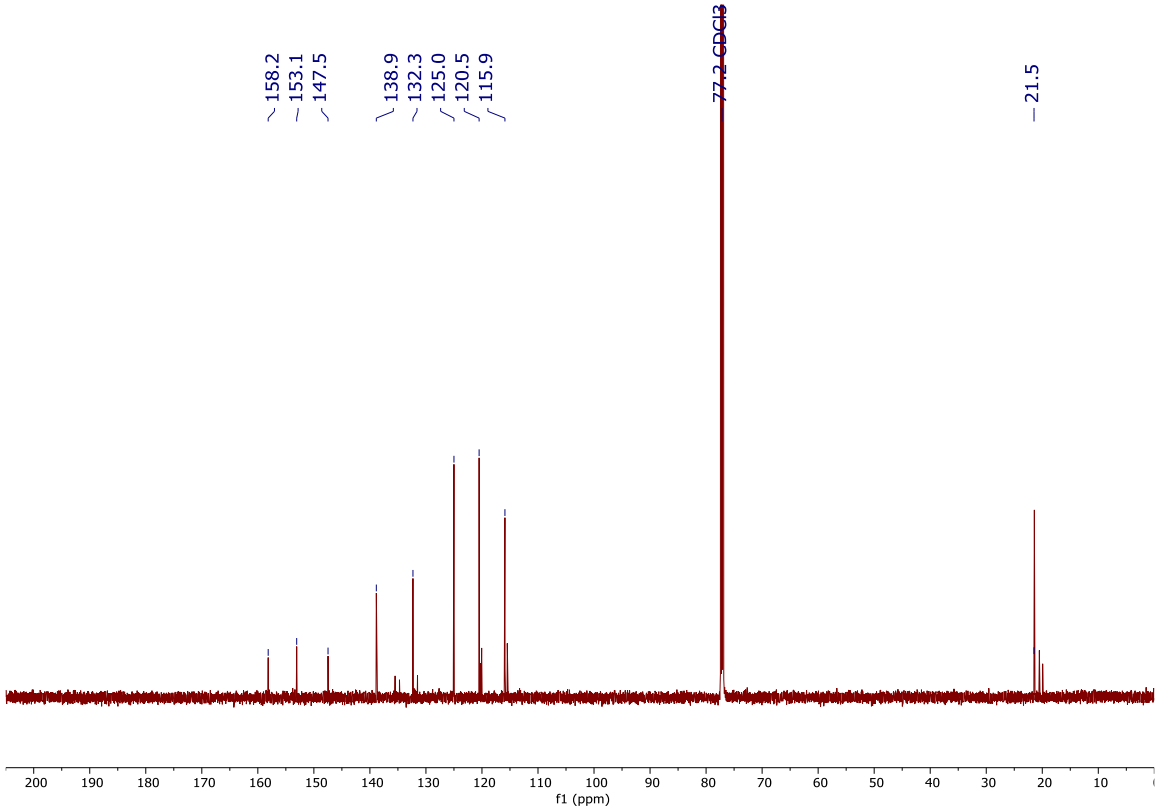


Compound AB.CO_2Me

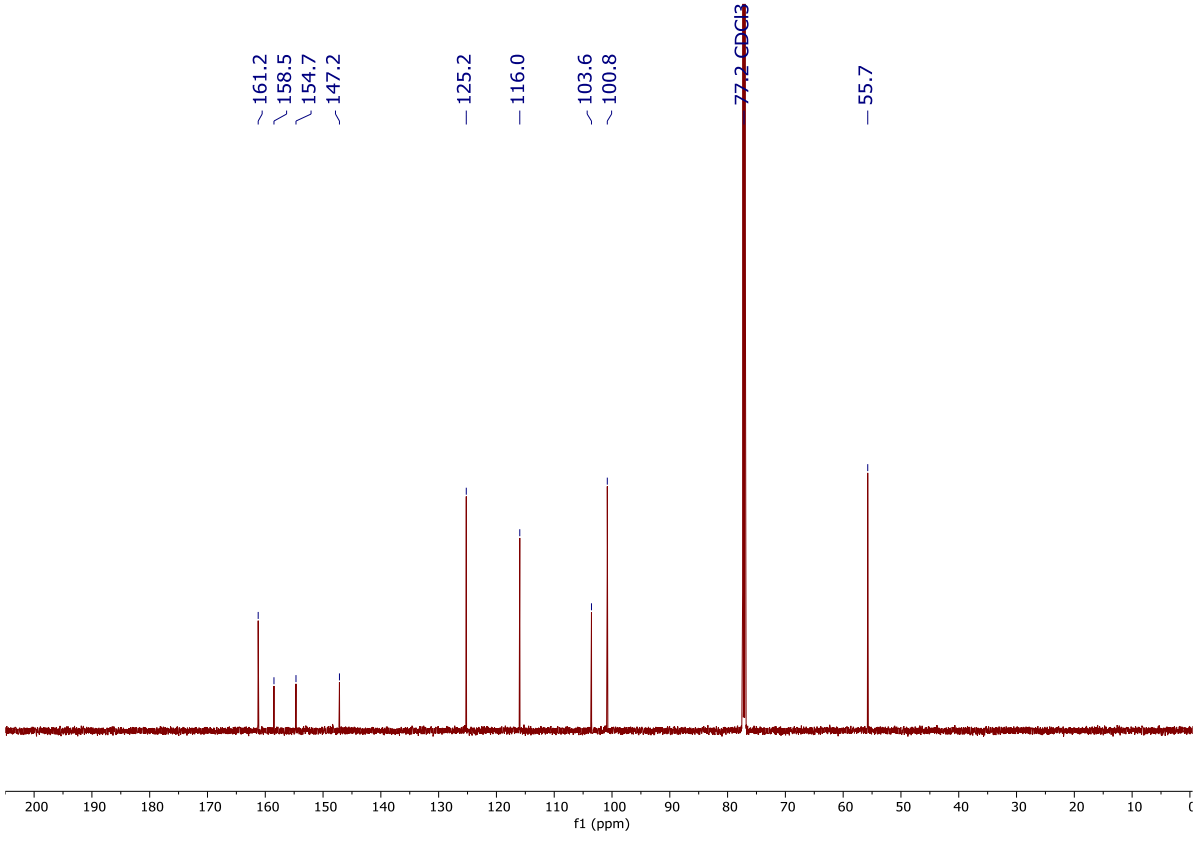


^{13}C NMR Spectra in Chapter 2

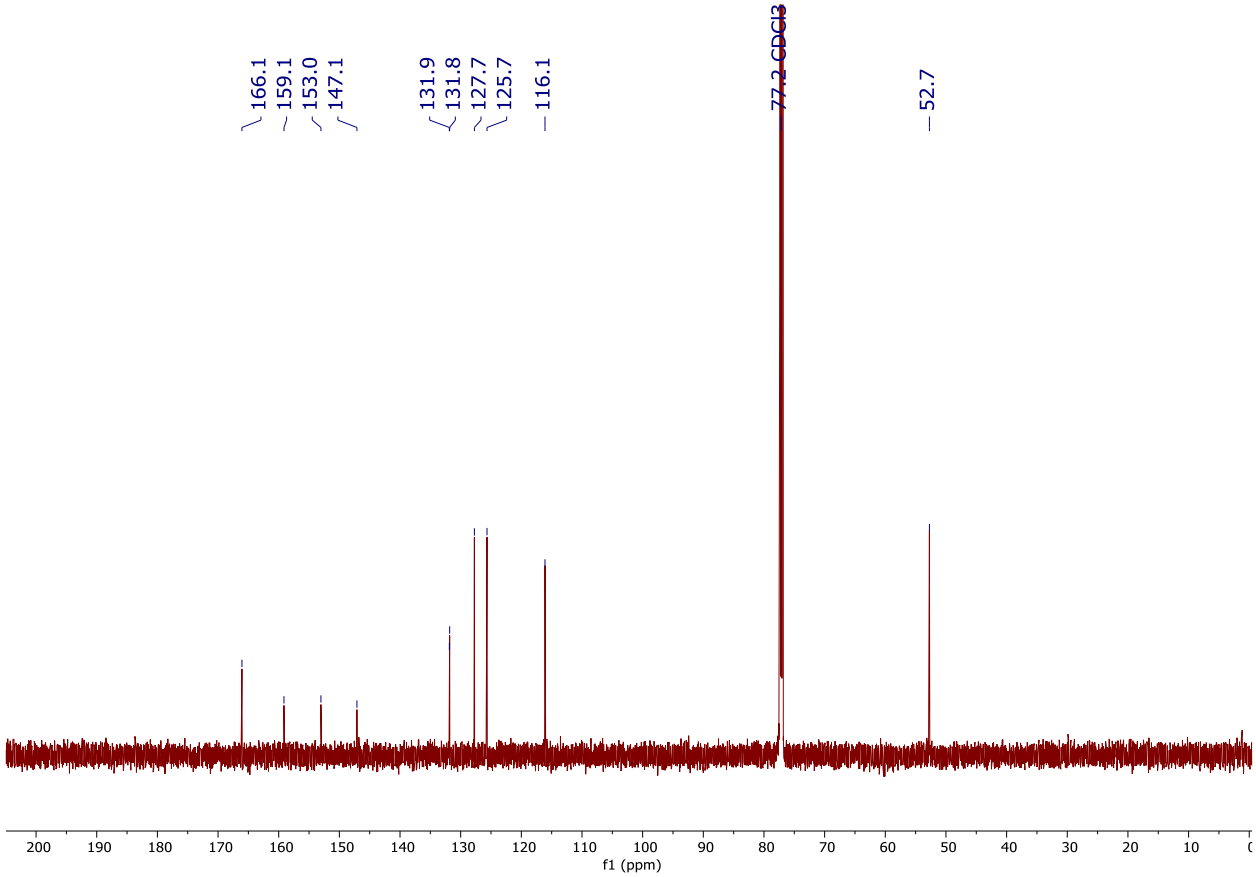
Compound AB-OH.Me



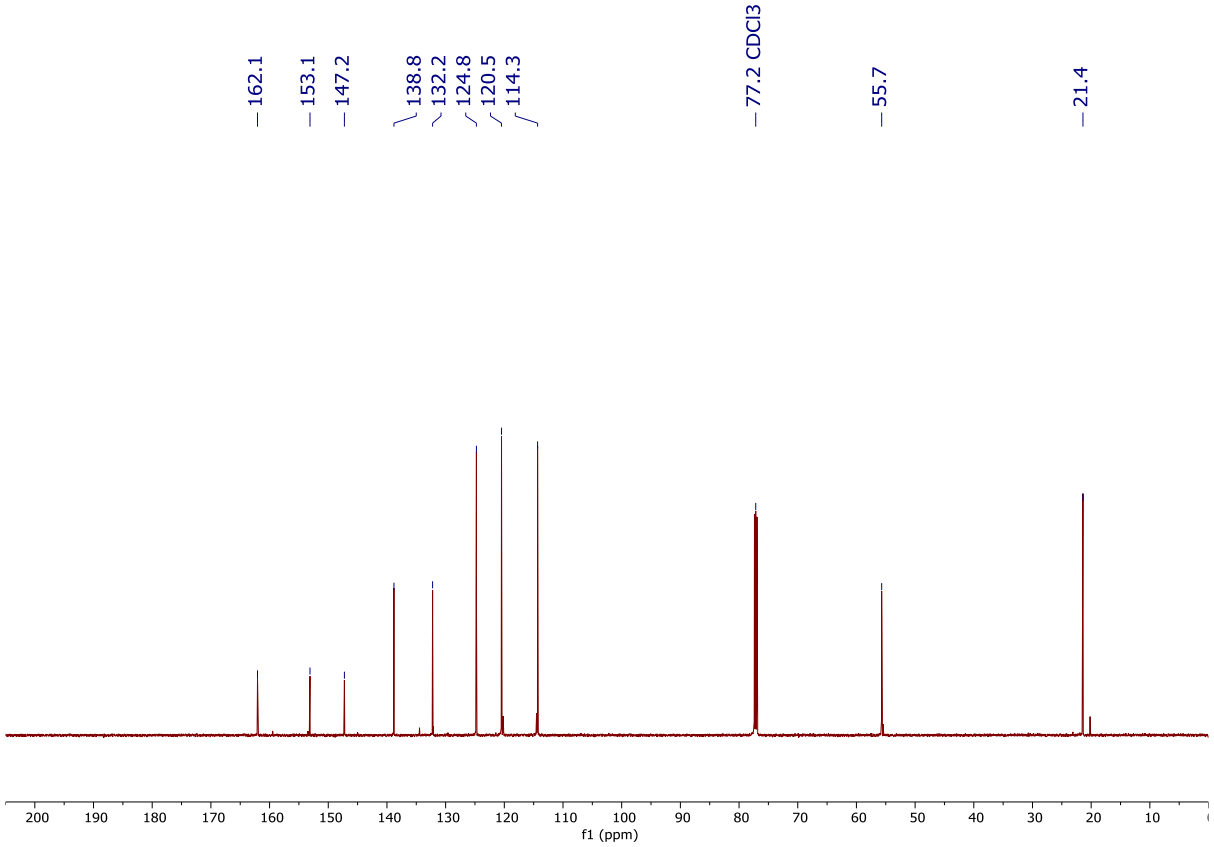
Compound AB-OH.OMe



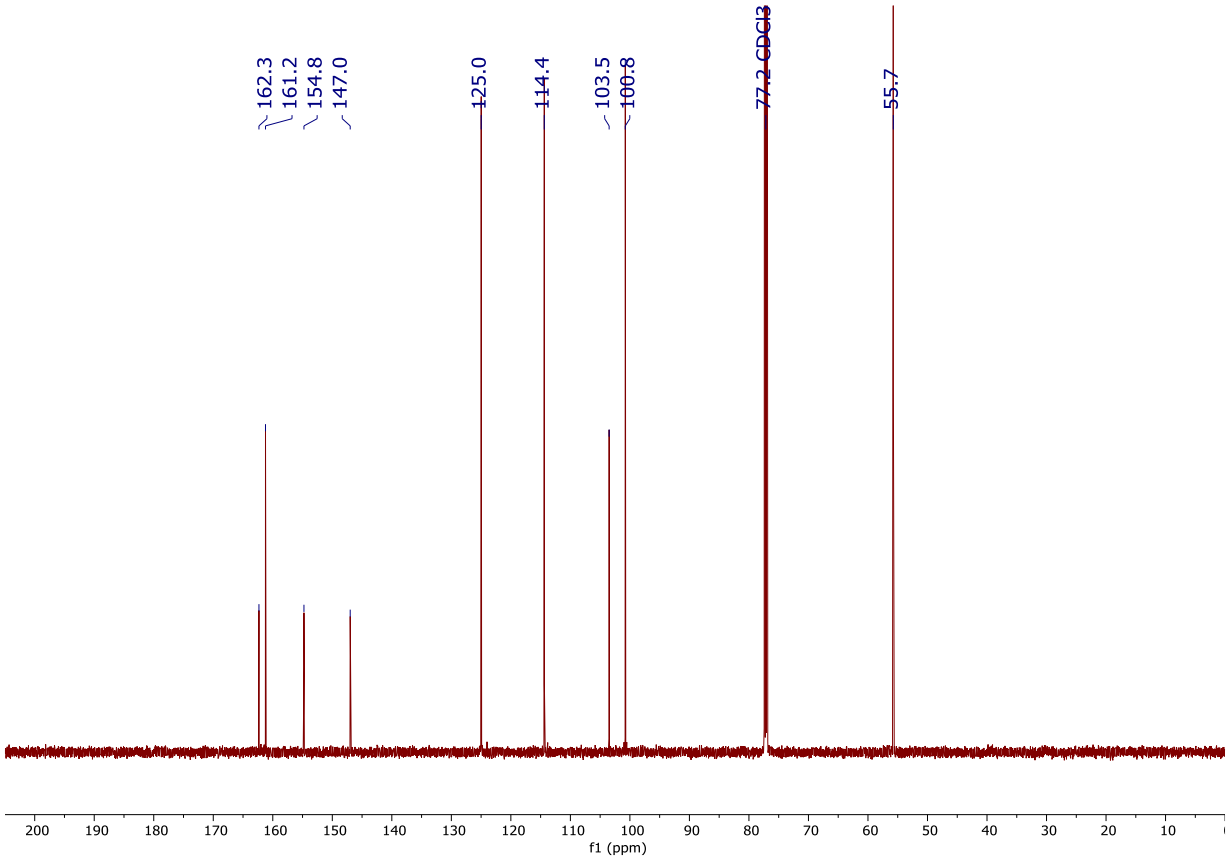
Compound AB-OH.CO_2Me



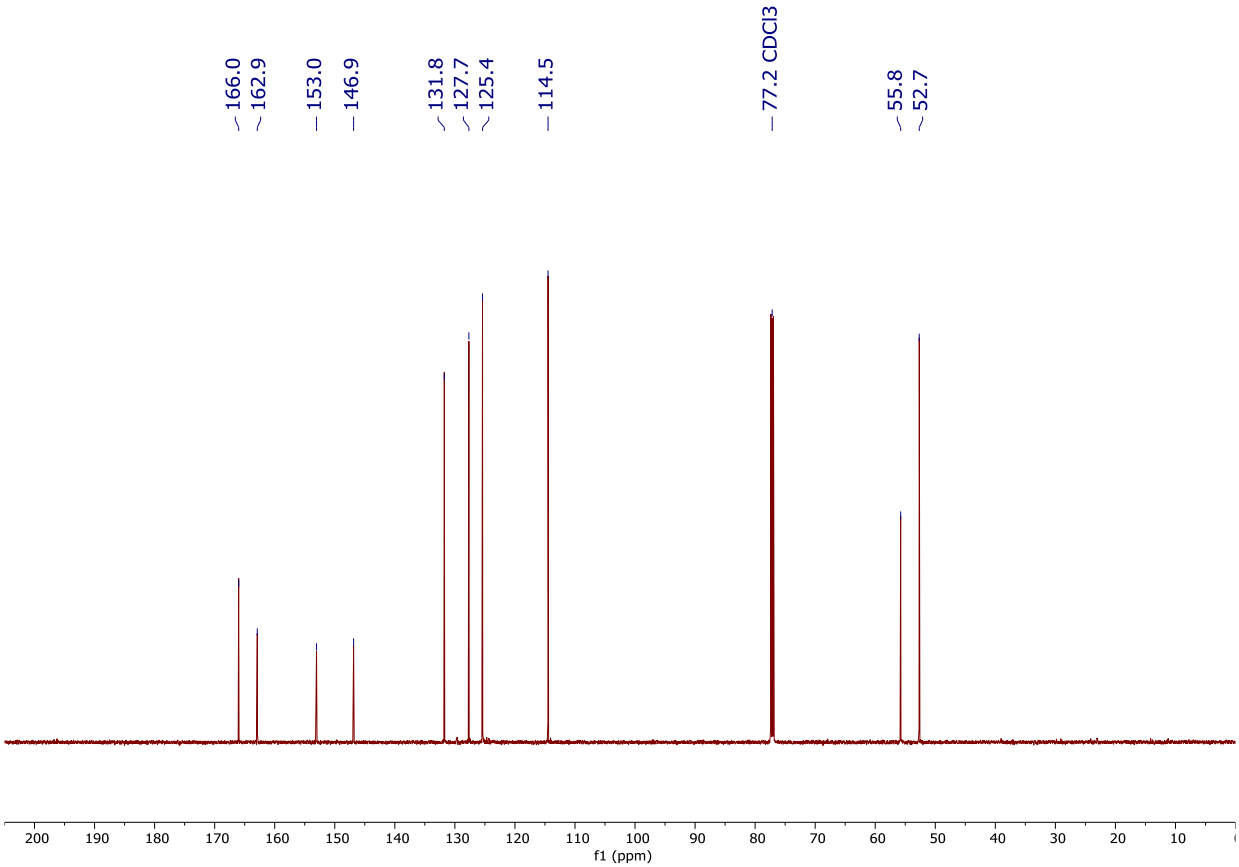
Compound AB.Me



Compound AB.OMe

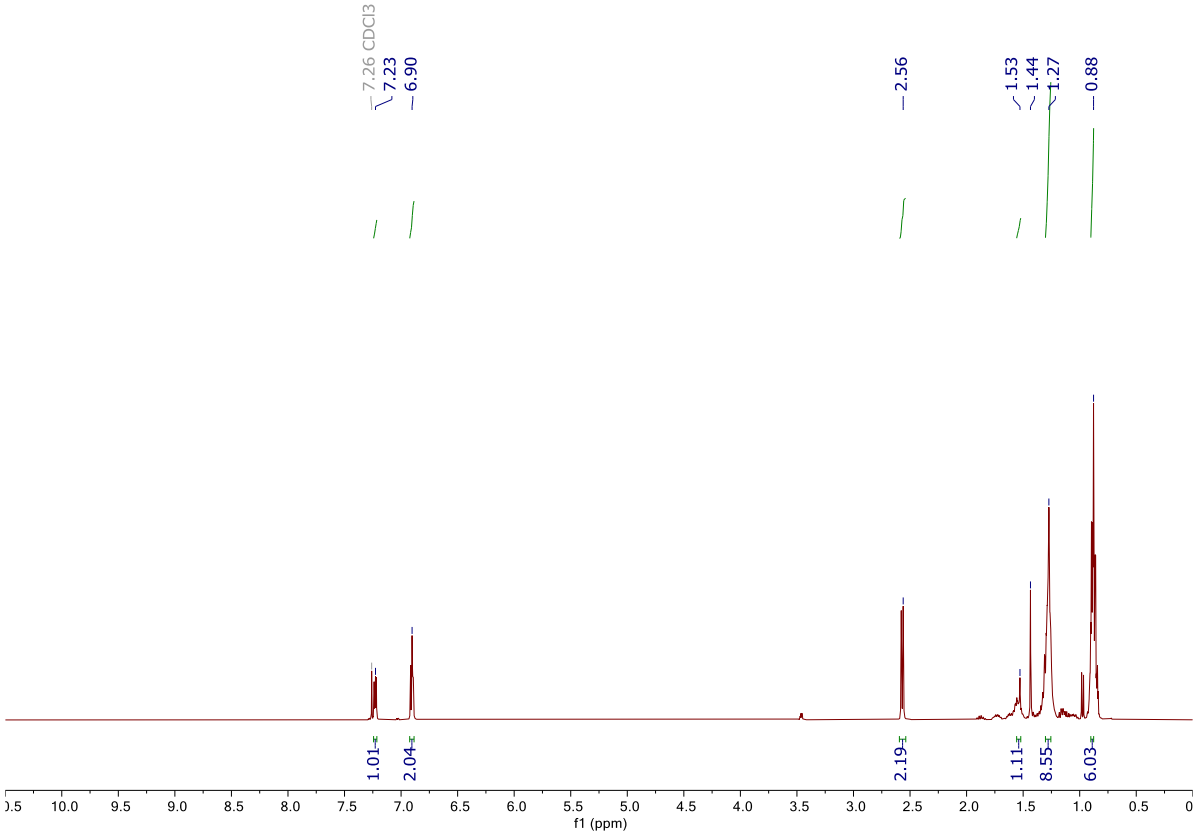


Compound AB.CO_2Me

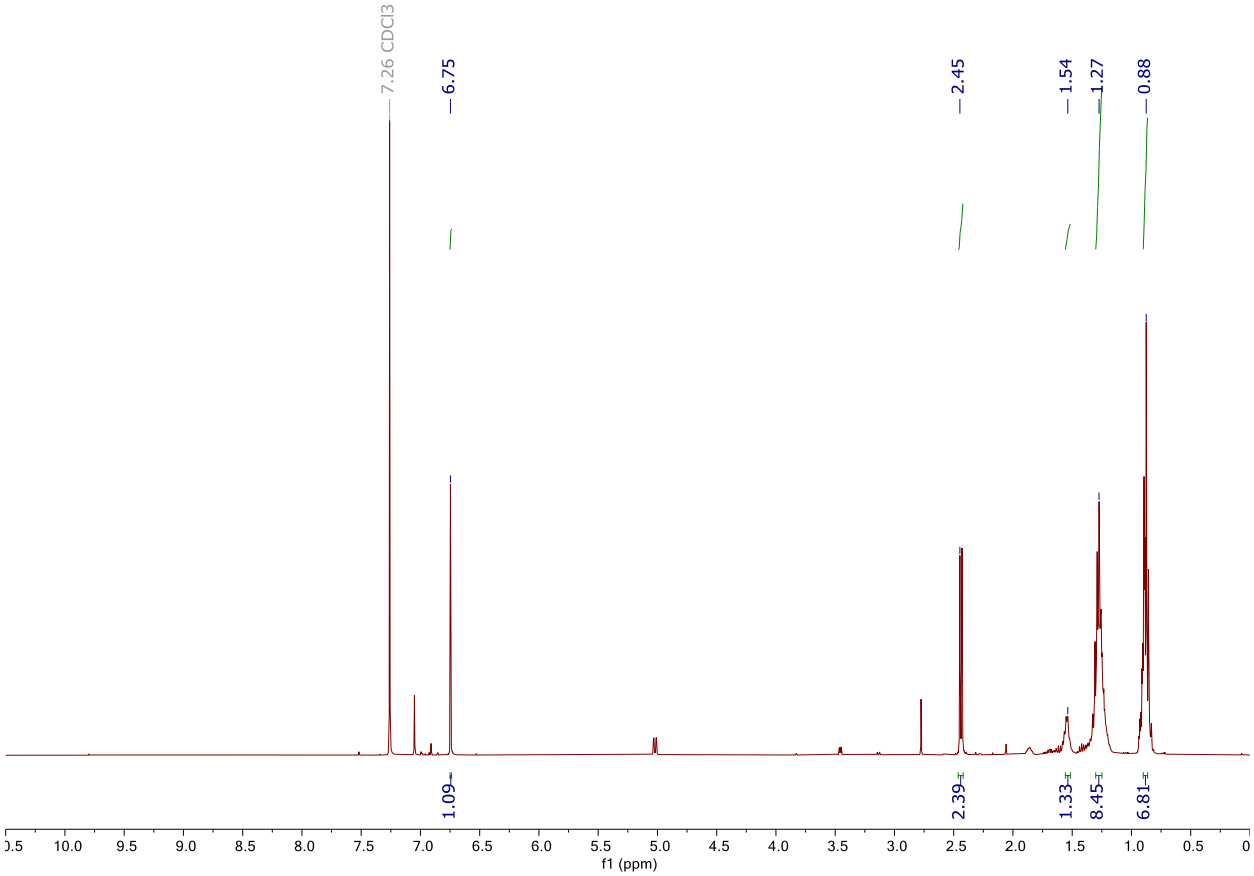


[1]H NMR Spectra of Compounds in Chapter 3

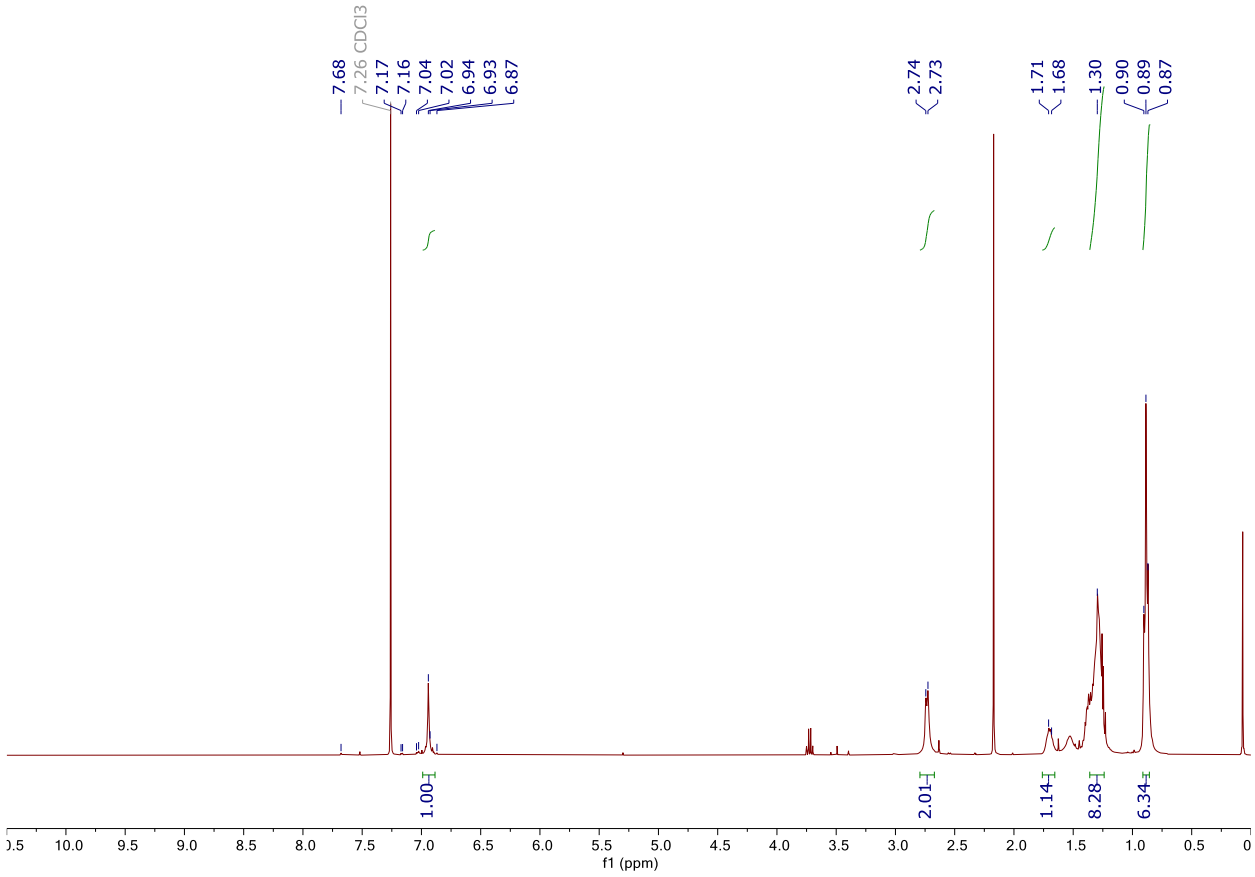
Compound 3-ehtylhexylhiophene (7)



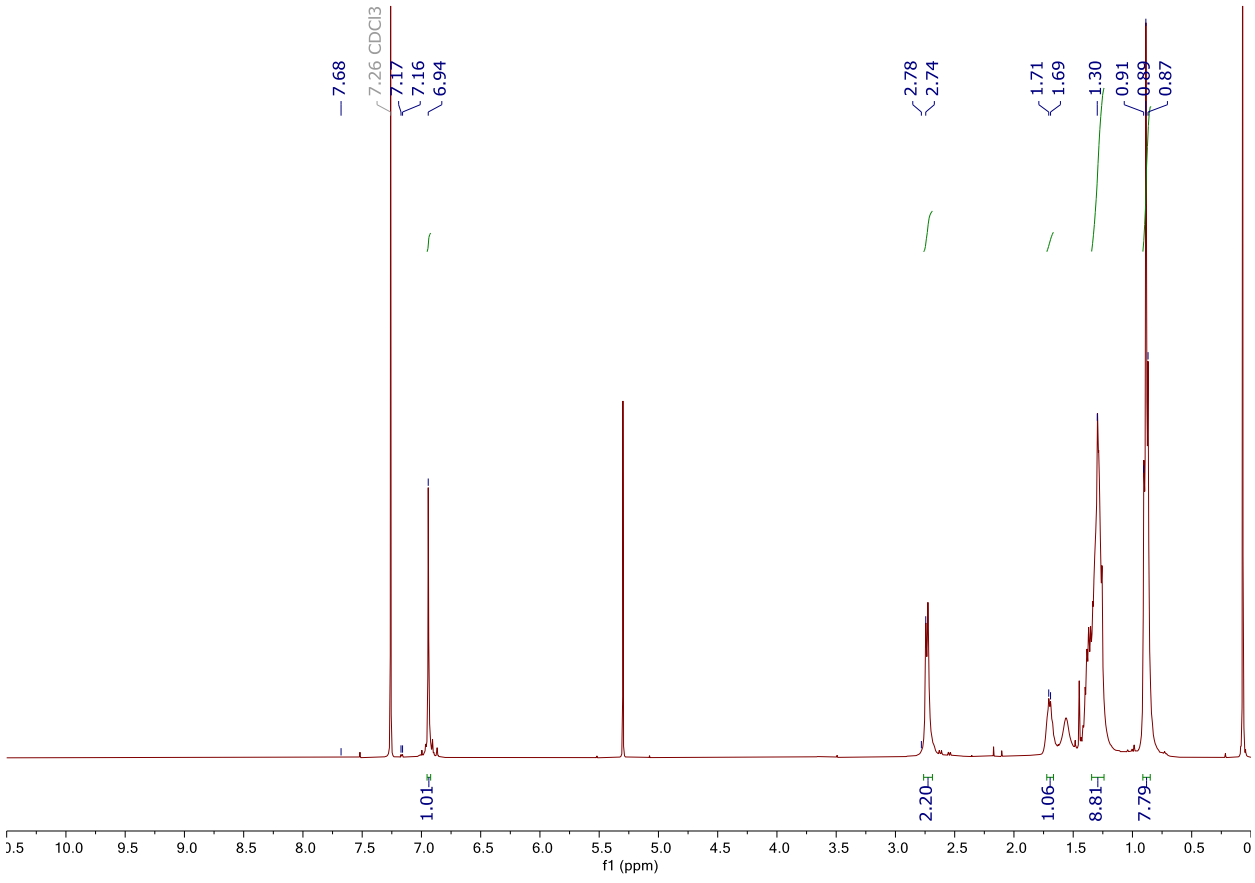
Compound 2,5-dibromo-3-(2-ethylhexyl)thiophene (8)



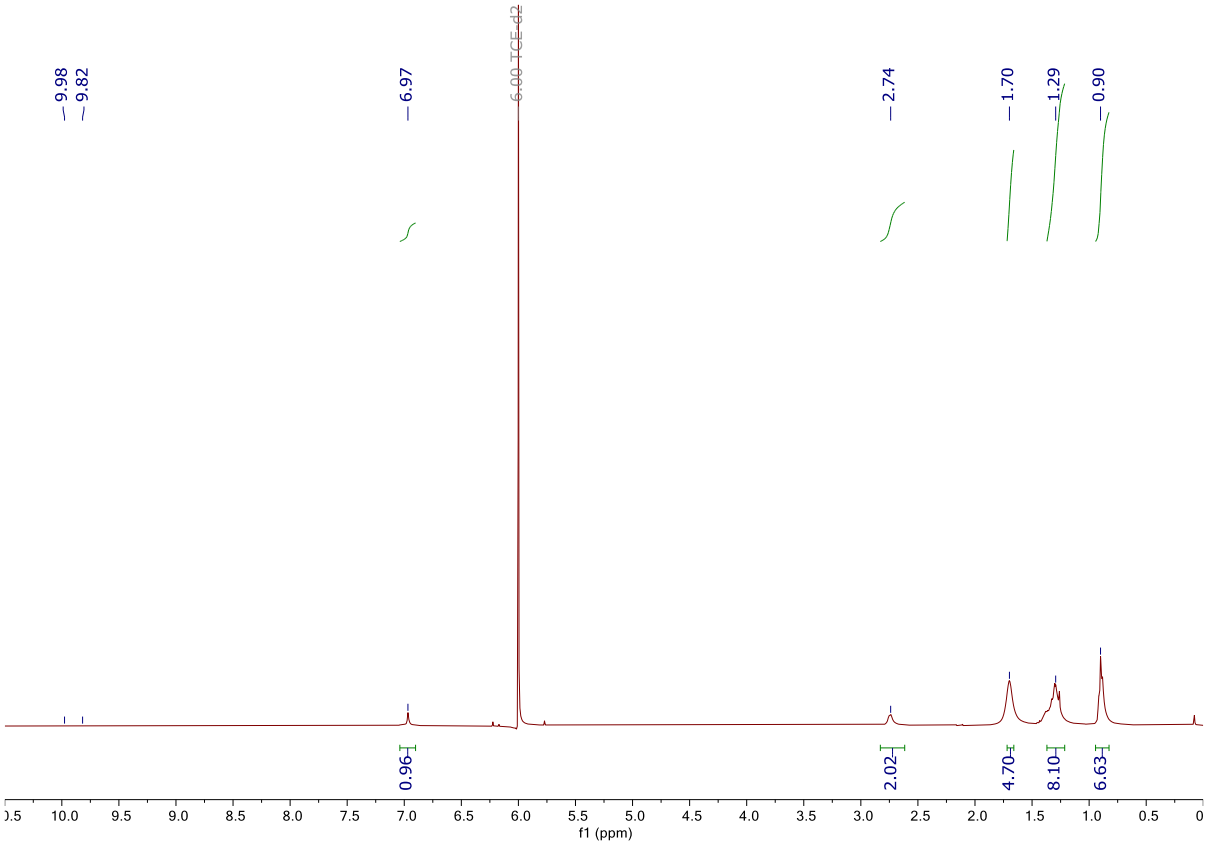
Compound P3EHT (11)



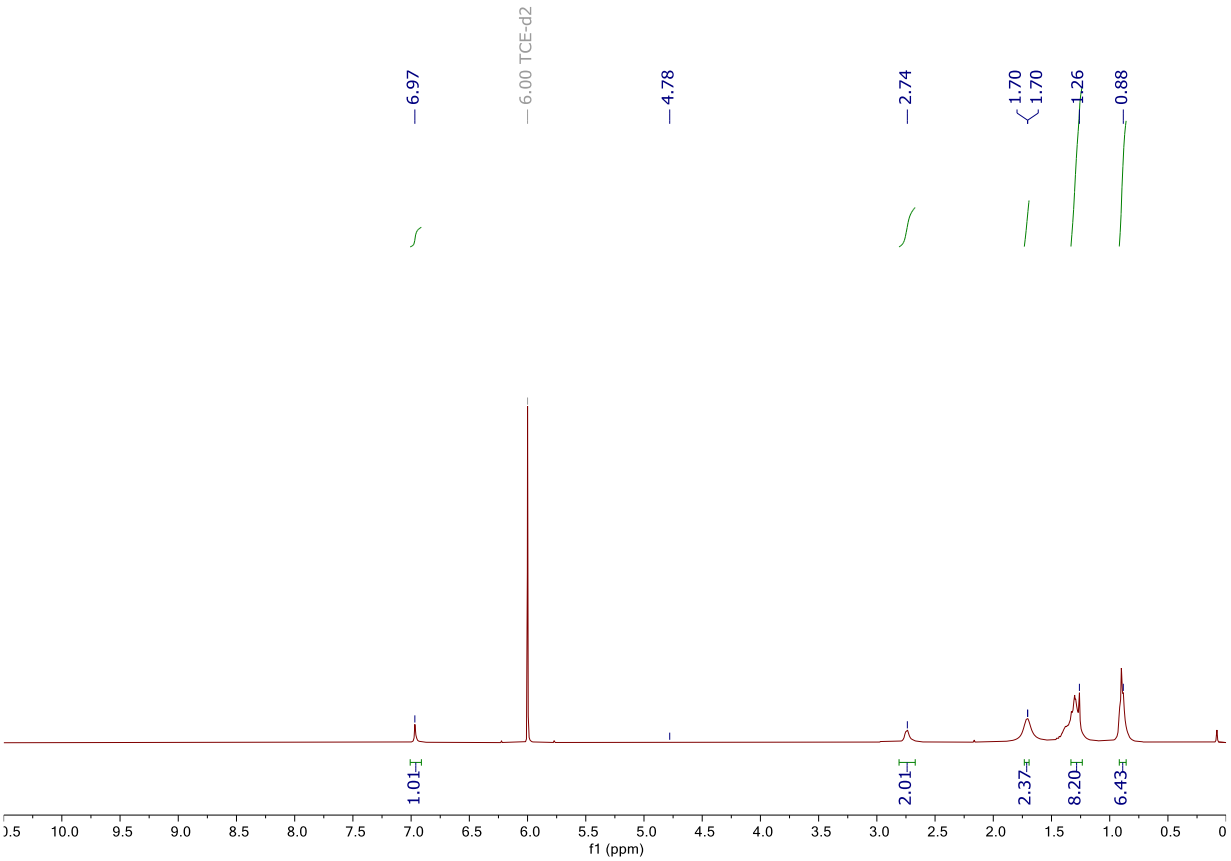
Compound H-P3EHT-H (11)



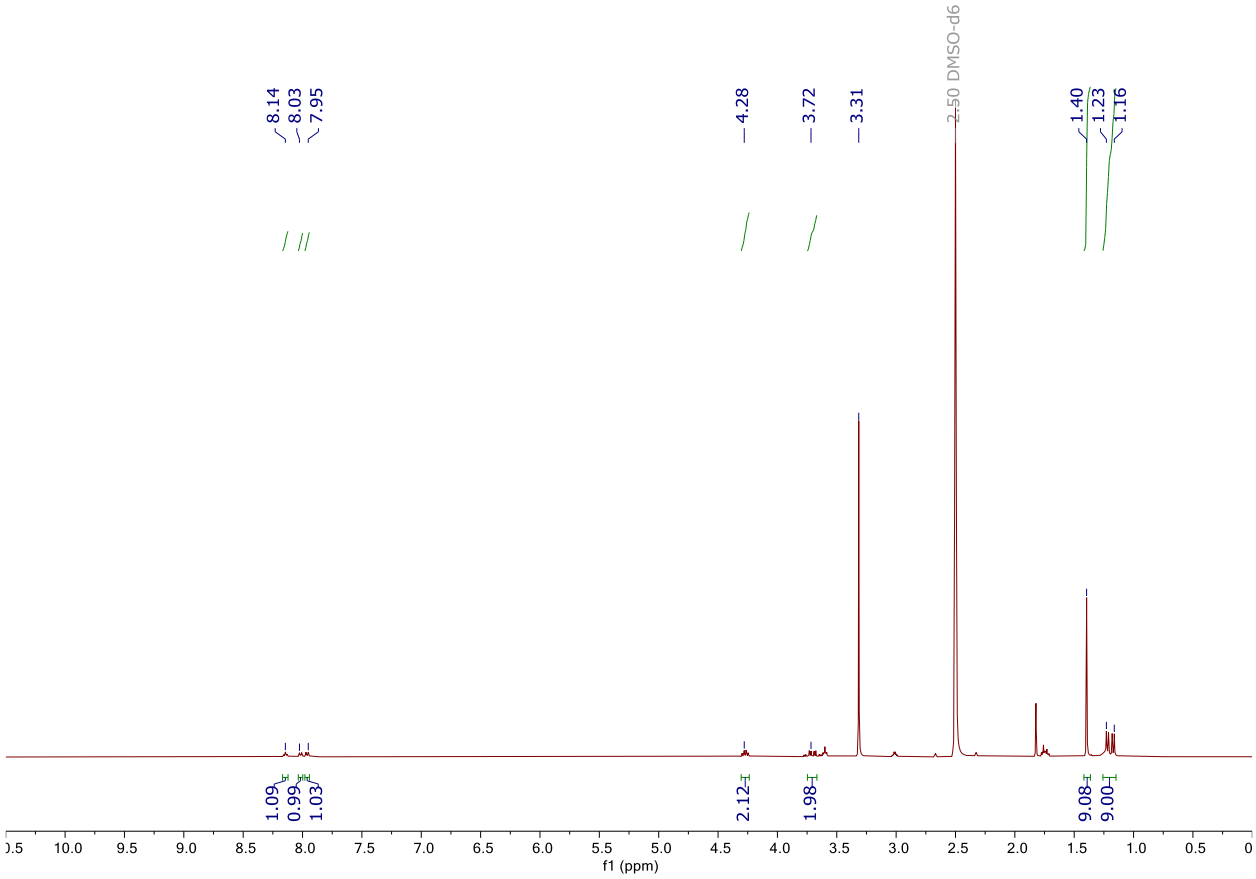
Compound CHO-P3EHT-CHO (11)



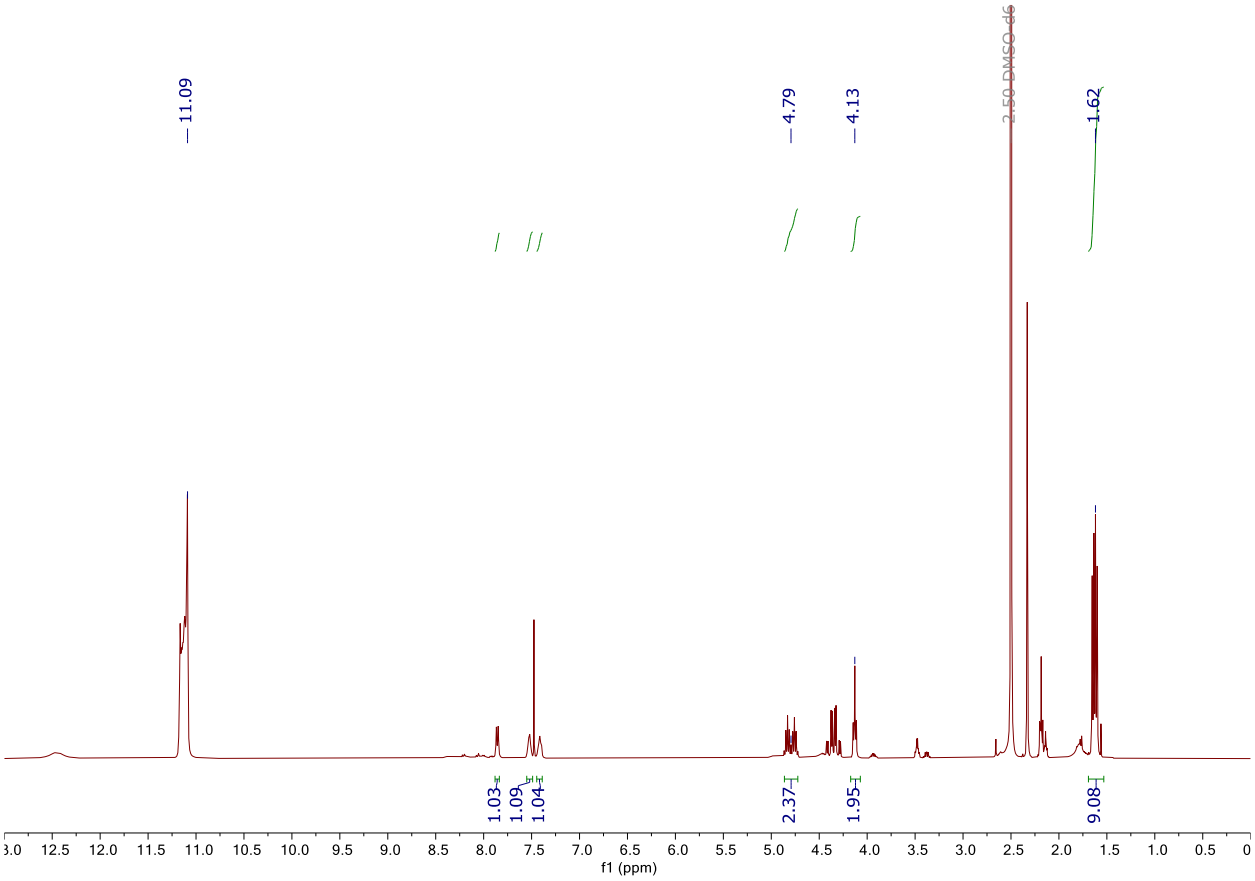
Compound OH-P3EHT-OH (11)



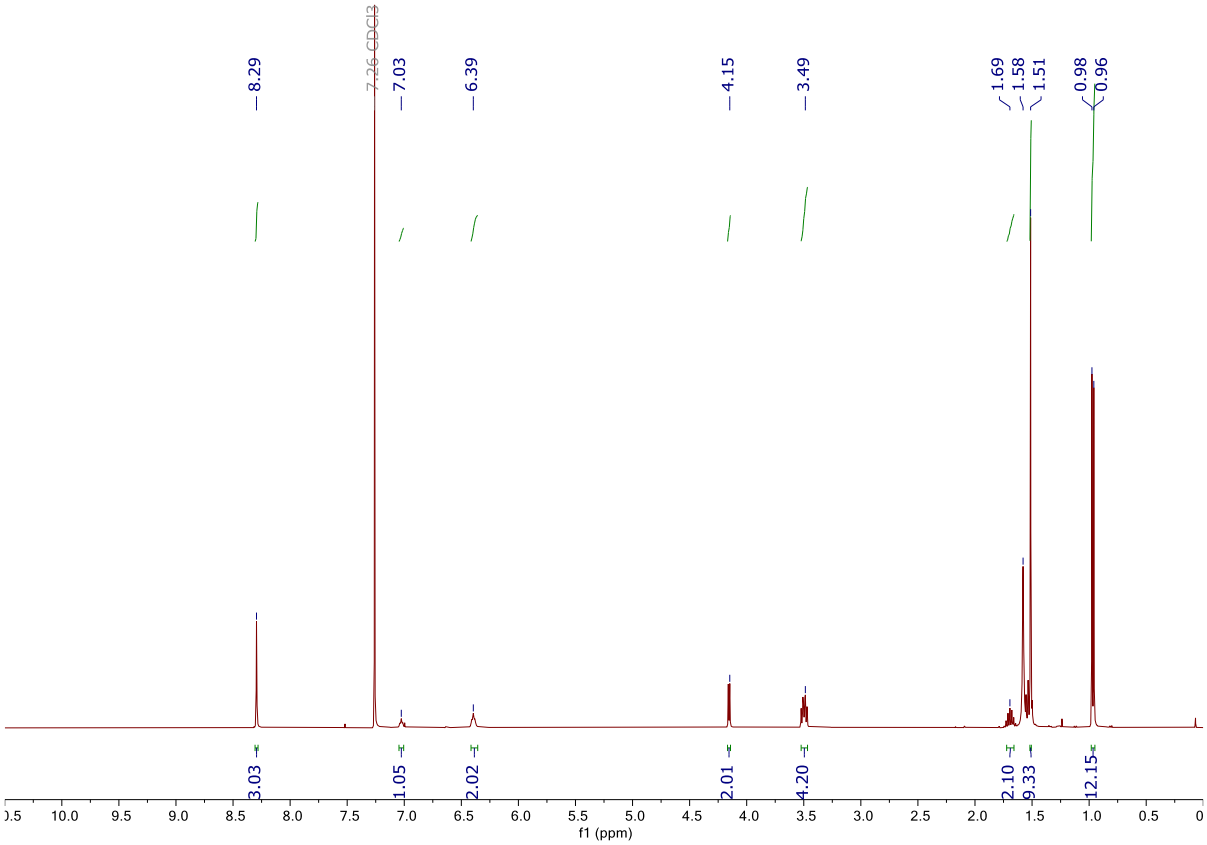
Compound tert-butyl acetylalanylalanylglycinate (16)



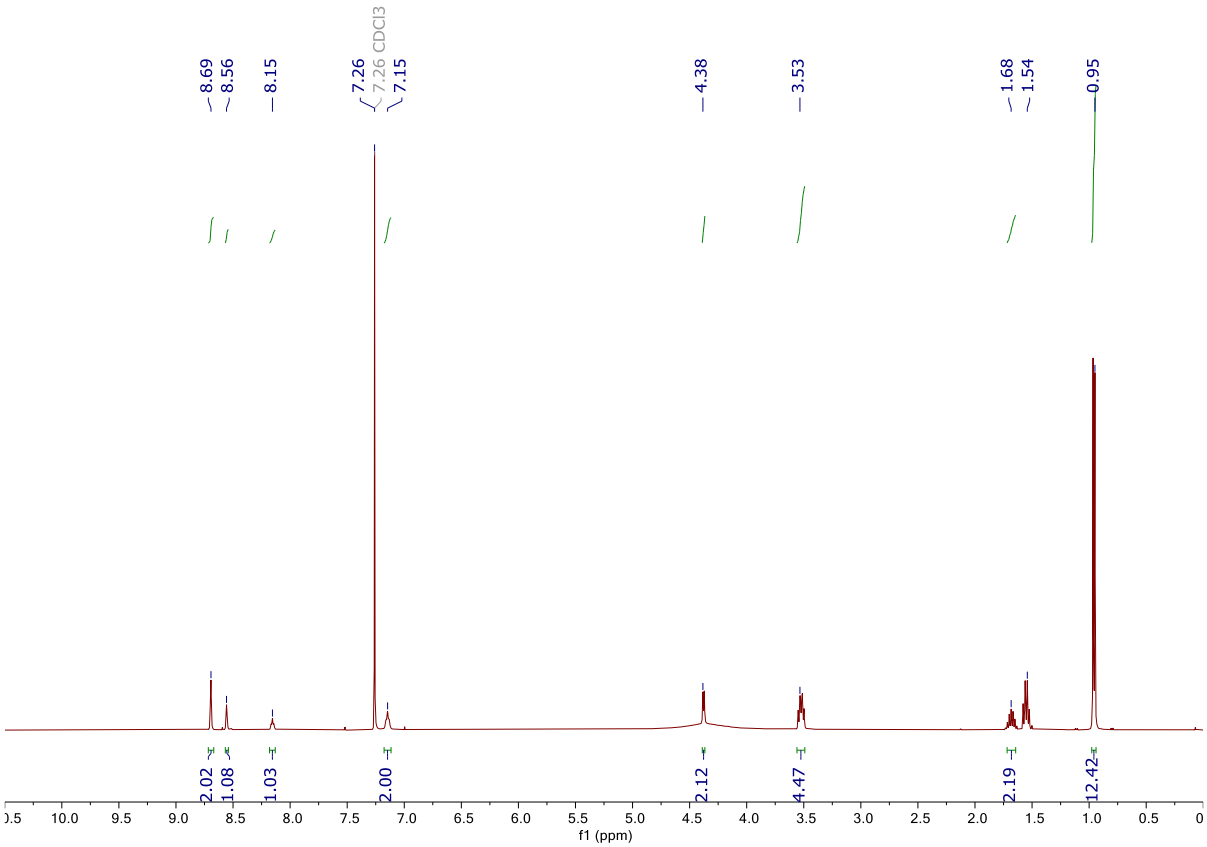
Compound acetylalanylalanylglycine (17)



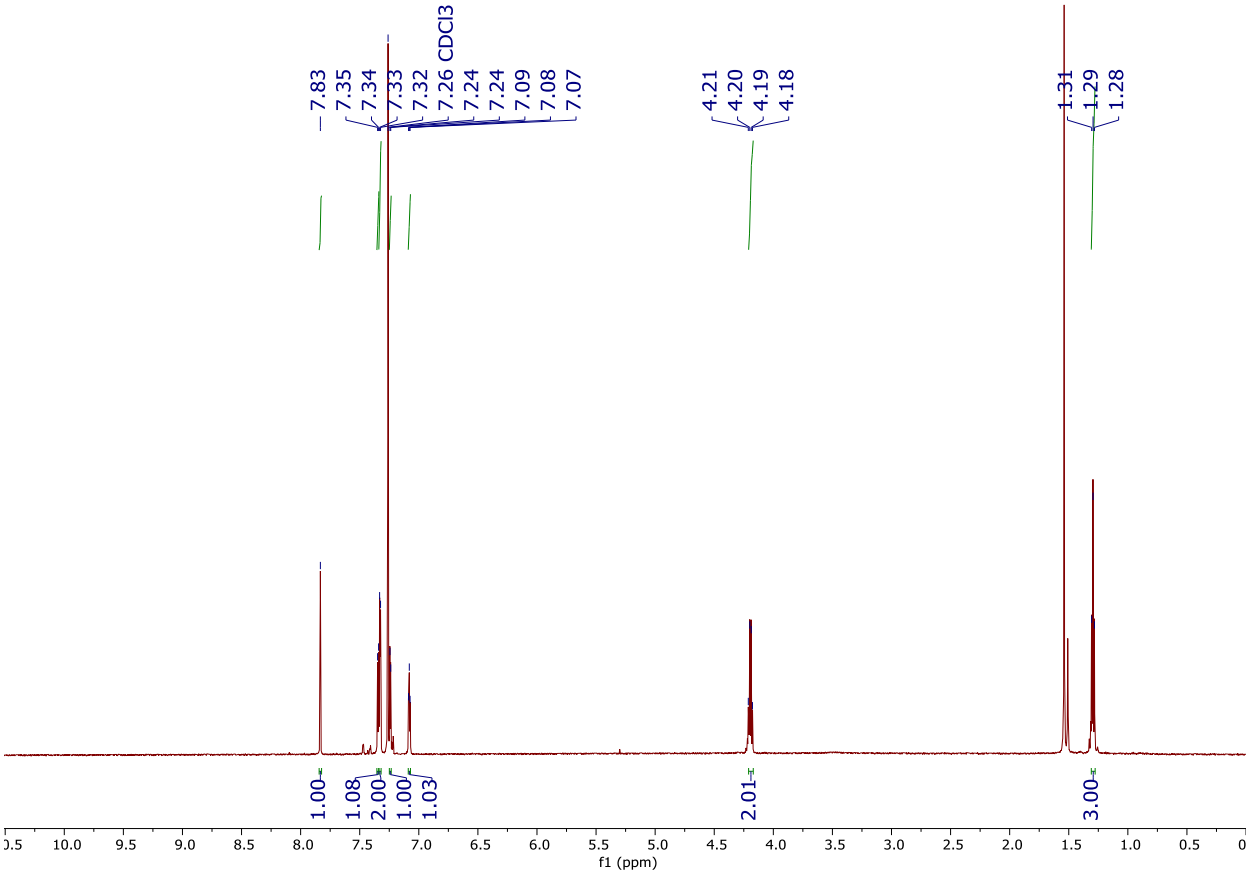
Compound tert-butyl (3,5-bis(isobutylcarbamoyl)benzoyl)glycinate (18)



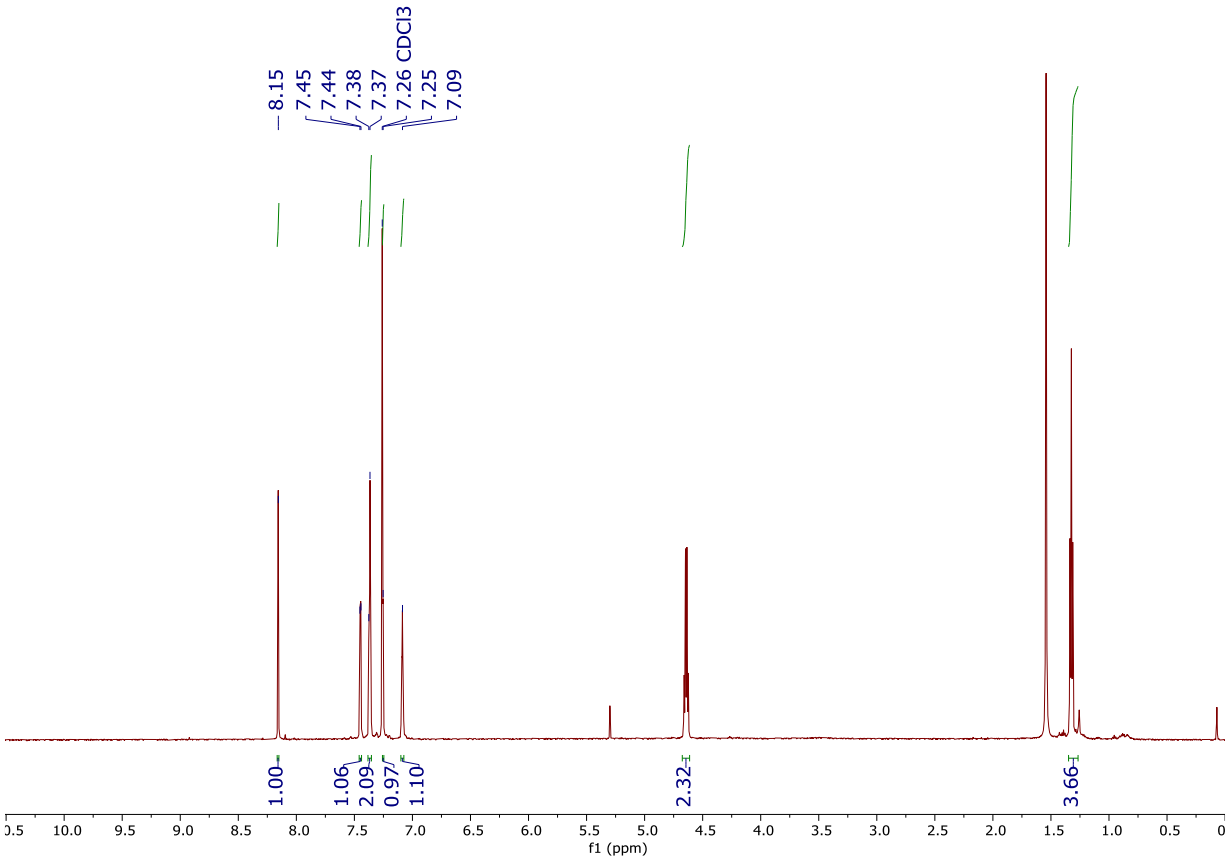
Compound (3,5-bis(isobutylcarbamoyl)benzoyl)glycine (19)



Compound BTR (20)

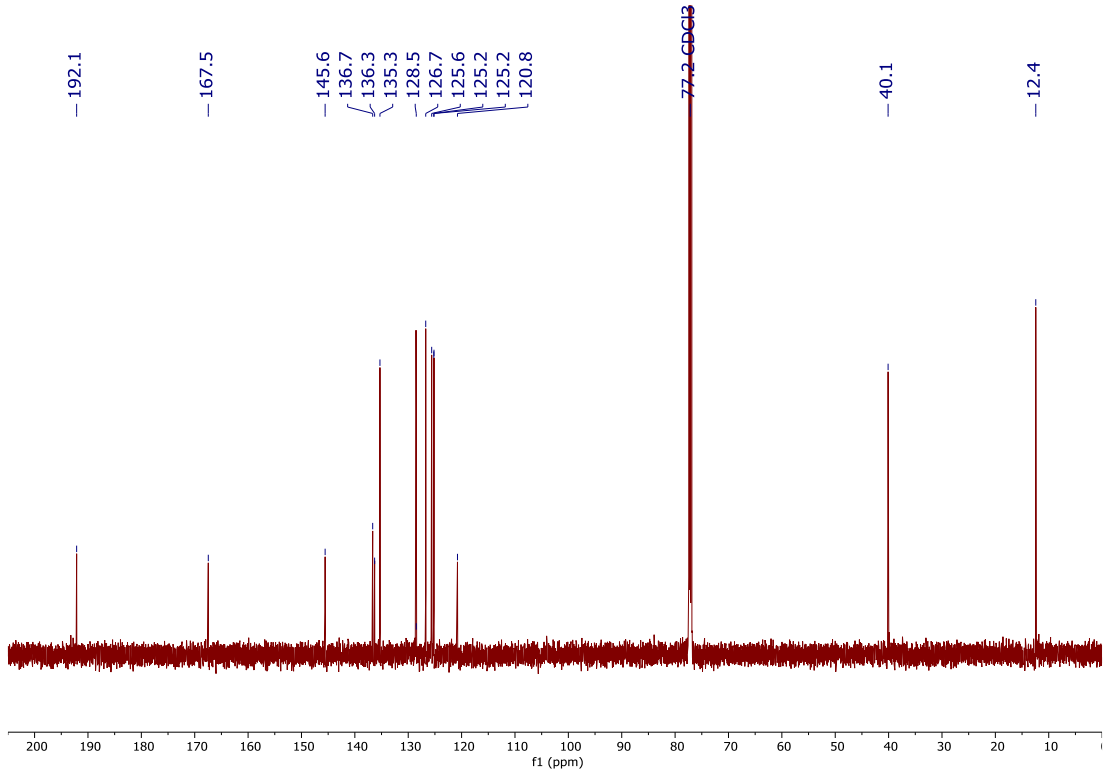


Compound BTR-2S (21)

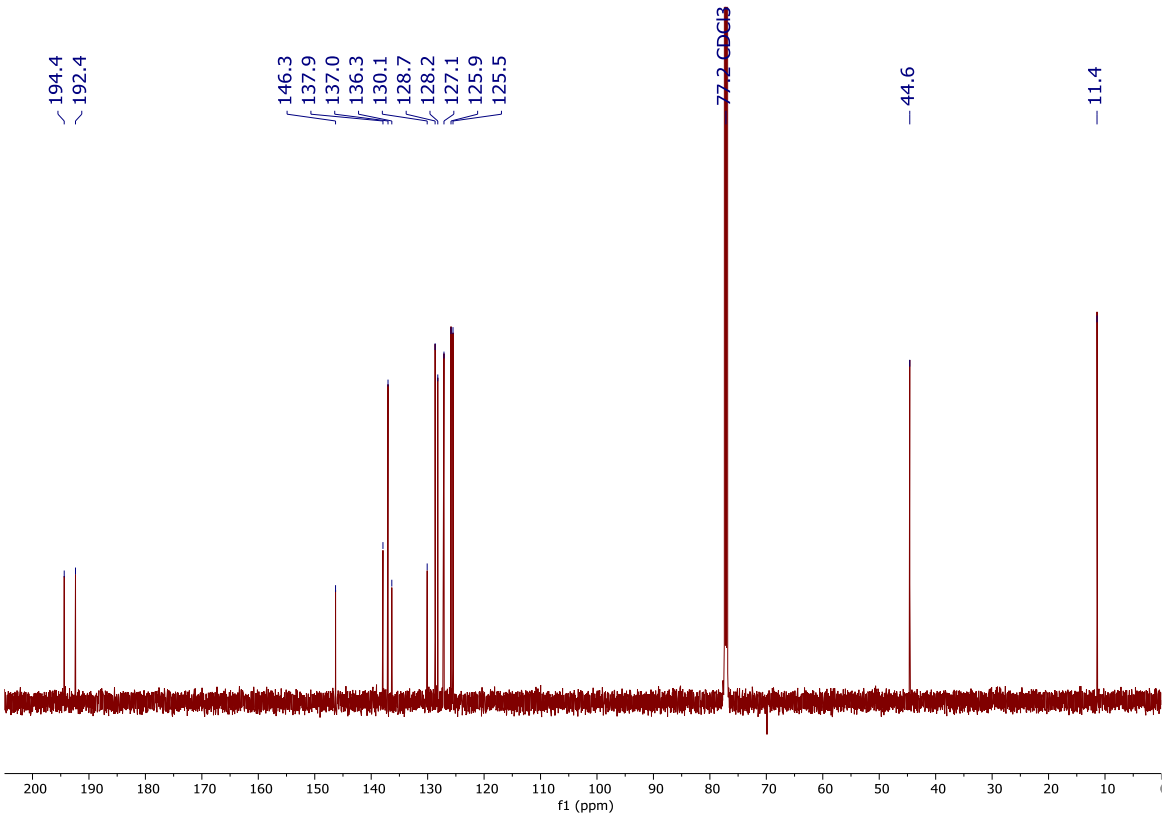


^{13}C NMR Spectra of Compounds in Chapter 3

Compound BTR (20)



Compound BTR-2S (21)



7. References

1. Luo, G.; Ren, X.; Zhang, S.; Wu, H.; Choy, W.; He, Z.; Cao, Y. Recent Advances in Organic Photovoltaics: Device Structure and Optical Engineering Optimization on the Nanoscale. *Small* **2016**, *12*, 1547-1571;
2. Muccini, M. A Bright Future for Organic Field-Effect Transistors. *Nature Materials*, **2006**, *5*, 605-613.
3. Lanzani, G. Materials for Bioelectronics: Organic Electronics Meets Biology. *Nature Materials*, **2014**, *13*, 775-776;
4. Cacialli, F. Organic Semiconductors for the New Millennium. *Philosophical Transactions of the Royal Society A: Mathematical, Physical and Engineering Sciences*, **2000**, *358*, 173-192.
5. Chowdhury, D. Q.; Garner, S. M.; Lewis, S. C. Application of OLED for Automotive Lighting. *2019 26th International Workshop on Active-Matrix Flatpanel Displays and Devices (AM-FPD)*, Kyoto, Japan, **2019**, pp. 1-3.
6. Baran, D.; Ashraf, R.; Hanifi, D.; Abdelsamie, M.; Gasparini, N.; Röhr, J. A.; Holliday, S.; Wadsworth, A.; Lockett, S.; Neophytou, M.; Emmott, C. J. M.; Nelson, J.; Brabec, C. J.; Amassian, A.; Salleo, A.; Kirchartz, T.; Durrant, J. R.; McCulloch, I. Reducing the efficiency–stability–cost gap of organic photovoltaics with highly efficient and stable small molecule acceptor ternary solar cells. *Nature Mater* **2017**, *16*, 363–369.
7. Horowitz, G. Organic Field-Effect Transistors. *Advanced Materials*, **1998**, *10*, 365-377.
8. Harikrishna S., Panda A., Computational Study on the Effect of Substituents on the Structural and Electronic Properties of Thiophene–Pyrrole-Based π-Conjugated Oligomers, *Macromolecules,* **2013**, *46*, 844–855.
9. Zhang, X.; Richter, L.; DeLongchamp, D.; Kline, R.J.; Hammond, M.; McCulloch, I.; Heeney, M.; Ashraf, R.S.; Smith, J.; Anthopoulos, T.; Schroeder, B.; Geerts, Y.; Fischer, D.; Toney, M. Molecular packing of high-mobility diketo pyrrolo-pyrrole polymer semiconductors with branched alkyl side chains. *Journal of the American Chemical Society* **2011**, *133*, 15073–15084.
10. Zhang, C.; Yuan, D.; Wu, H.; Gann, E.; Thomsen, L.; McNeill, C.; Di, C.-A.; Zhu, X.; Zhu, D. Insight into Thin-Film Stacking Modes of π-Expanded Quinoidal Molecules on Charge Transport Property via Side-Chain Engineering. *Journal of Materials Chemistry C* **2017**, *5*, 1935-1943.
11. Ferlauto, L.; Liscio, F.; Orgiu, E.; Masciocchi, N.; Guagliardi, A.; Biscarini, F.; Samorí, P.; Milita, S. Enhancing the Charge Transport in Solution-Processed Perylene Di-imide Transistors via

Thermal Annealing of Metastable Disordered Films. *Advanced Functional Materials* **2014**, 24, 5503-5510.

12. Poelking, C. Organic Electronics in a Nutshell. In *Introduction to Organic Electronics*; Springer: **2018**; pp. 1-11.
13. Heeger, A.J.; MacDiarmid, A.G.; Shirakawa, H. "Electrical Conductivity in Doped Polyacetylene." *Appl. Phys. Lett.* **1976**, *29*, 414.
14. Fu, J.; Fong, P.W.K.; Liu, H.; Huang, C.-S.; Lu, X.; Lu, S.; Abdelsamie, M.; Kodalle, T.; Sutter-Fella, C.M.; Yang, Y.; Li, G. 19.31% Binary Organic Solar Cell and Low Non-Radiative Recombination Enabled by Non-Monotonic Intermediate State Transition. *Nat. Commun.* **2023**, *14*, Article number: 1760.
15. Wadsworth, A.; Hamid, Z.; Kosco, J.; Gasparini, N.; McCulloch, I. The Bulk Heterojunction in Organic Photovoltaic, Photodetector, and Photocatalytic Applications. *Adv. Mater.* **2020**, *32*, 2001763
16. Shoaee, S.; Sanna, A.L.; Sforazzini, G. Elucidating Charge Generation in Green-Solvent Processed Organic Solar Cells. *Molecules* **2021**, *26*, 7439.
17. Wu, J.S.; Cheng, S.W.; Cheng, Y.J.; Hsu, C.S. Donor-Acceptor Conjugated Polymers Based on Multifused Ladder-Type Arenes for Organic Solar Cells. *Chemical Society Reviews* **2015**, *44*, 1113-1154.
18. Manca, M., Piliego, C., Wang, E., Andersson, M., Mura, A., Loi, M. Tracing charge transfer states in polymer:fullerene bulk-heterojunctions. *Journal of Materials Chemistry*, **2013**, *1*, 7321-7325.
19. Gong, M.; Shastry, T.A.; Cui, Q.; Kohlmeyer, R.R.; Luck, K.; Rowberg, A.; Marks, T.; Durstock, M.; Zhao, H.; Hersam, M.; Ren, S. Understanding Charge Transfer in Carbon Nanotube-Fullerene Bulk Heterojunctions. *ACS Applied Materials & Interfaces* **2015**, *7*, 7428-7435.
20. Barth, S.; Bassler, H. Intrinsic Photoconduction in PPV-Type Conjugated Polymers. *Phys. Rev. Lett.* **1997**, *79*, 4445.
21. Dennler, G.; Scharber, M.C.; Brabec, C.J. Polymer-Fullerene Bulk-Heterojunction Solar Cells. *Adv. Mater.* **2009**, *21*, 1323.
22. Kozub, D.R.; Vakhshouri, K.; Kesava, S.V.; Wang, C.; Hexemer, A.; Gomez, E.D. Direct Measurements of Exciton Diffusion Length Limitations on Organic Solar Cell Performance. *Chem. Commun.* **2012**, *48*, 5859.
23. Hedley, G.J.; Ward, A.J.; Alekseev, A.; Howells, C.T.; Martins, E.R.; Serrano, L.A.; Cooke, G.; Ruseckas, A.; Samuel, I.D.W. Determining the Optimum Morphology in High-Performance Polymer-Fullerene Organic Photovoltaic Cells. *Nat. Commun.* **2013**, *4*, 2867.

24. Cui, Y.; Xu, Y.; Yao, H.; Bi, P.; Hong, L.; Zhang, J.; Qin, J.; Ren, J.; Chen, Z.; He, C.; Hao, X.; Wei, Z.; Hou, J. Single-Junction Organic Photovoltaic Cell with 19% Efficiency. *Advanced Materials* **2021**, *33*, Article number: 200420.
25. Awartani, O.; Kudenov, M.; Kline, R.J.; O'Connor, B. In-Plane Alignment in Organic Solar Cells to Probe the Morphological Dependence of Charge Recombination. *Advanced Functional Materials* **2015**, *25*.
26. Ouyang, J.; Wu, F.; Zhao, X.; Yang, X. Regulating the Crystallinity and Self-Aggregation of Fused Ring Electron Acceptors via Branched Side-Chain Engineering for Efficient Organic Solar Cells. *Small* **2022**, *e2201769*.
27. Guo, J.; Hu, K.; Qiu, B.; Zhang, J.; Yang, D.; Zhou, L.; Li, S.; Meng, L.; Zhang, Z.; Li, Y. Fine-Tuning Miscibility and π-π Stacking by Alkylthio Side Chains of Donor Molecules Enables High-Performance All-Small-Molecule Organic Solar Cells. *ACS Applied Materials & Interfaces* **2021**, *13*, 36033–36043.
28. Garcia Romero, D.; Di Mario, L.; Portale, G.; Loi, M. Crystallization Driven Boost in Fill Factor and Stability in Additive-Free Organic Solar Cells. *Journal of Materials Chemistry A* **2021**, *9*, 23783-23792.
29. Liao, X.; Lv, R.; Chen, L.; Chen, Y. Synergistic Effect of Processing Additives and Thermal Annealing in Organic Solar Cells: The "Morphology of Magic". *Physical Chemistry Chemical Physics* **2017**, *19*, 10581-10589.
30. Hou, J.; Guo, X. Active Layer Materials for Organic Solar Cells. In Green Energy and Technology; Springer: **2013**, pp17-42.
31. Wantz, G.; Derue, L.; Dautel, O.; Rivaton, A.; Hudhomme, P.; Dagron-Lartigau, C. Stabilizing Polymer-Based Bulk Heterojunction Solar Cells via Crosslinking. *Polymer International* **2014**, *63*, 1346-1361.
32. Wu, J.-S.; Cheng, S.-W.; Cheng, Y.-J.; Hsu, C.-S. Donor-Acceptor Conjugated Polymers Based on Multifused Ladder-Type Arenes for Organic Solar Cells. *Chemical Society Reviews* **2015**, *44*, 1113-1154.
33. Agbolaghi, S.; Zenoozi, S. A comprehensive review on poly(3-alkylthiophene)-based crystalline structures, protocols and electronic applications. *Organic Electronics* **2017**, *51*, 362-403.
34. Ivanov, M.; Gross, J.; Janke, W. Single-chain behavior of poly(3-hexylthiophene). *The European Physical Journal Special Topics* **2017**, *226*, 667-681.
35. Chen, P.-Y.; Rassamesard, A.; Chen, H.-L.; Chen, S. Conformation and Fluorescence Property of Poly(3-hexylthiophene) Isolated Chains Studied by Single Molecule Spectroscopy: Effects of Solvent Quality and Regioregularity. *Macromolecules* **2013**, *46*, 5657-5663.

36. Le, L.; Luu, T. An investigation on the optical properties of regioregular Poly(3-Hexylthiophene). **2014**. SCIENCE & TECHNOLOGY DEVELOPMENT, Vol 17, No.K4.
37. Wu, J.-S.; Cheng, S.-W.; Cheng, Y.-J.; Hsu, C.-S. Donor-acceptor conjugated polymers based on multifused ladder-type arenes for organic solar cells. *Chemical Society Reviews* **2015**, *44*, 1113-54.
38. Andersson, M.R.; Selse, D.; Berggren, M.; Jaervinen, H.; Hjertberg, T.; Inganaes, O.; Wennerstroem, O.; Oesterholm, J.-E. Regioselective polymerization of 3-(4-octylphenyl)thiophene with FeCl3. *Macromolecules* **1994**, *27*, 6503–6506.
39. Lee, J.; Kwon, Y.; Woo, Je-Wan; Moon, D. Synthesis and Characterization of Fluorine–Thiophene-Based π-Conjugated Polymers Using Coupling Reaction. *Journal of Industrial and Engineering Chemistry* **2008**, *14*, 810-817.
40. Yuan, J.; Zhang, Y.; Zhou, L.; Zhang, G.; Yip, H.; Lau, T.-k.; Lu, X.; Zhu, C.; Peng, H.; Johnson, P.A.; Leclerc, M.; Cao, Y.; Ulański, J.; Li, Y.; Zou, Y. Single-Junction Organic Solar Cell with over 15% Efficiency Using Fused-Ring Acceptor with Electron-Deficient Core. *Joule* **2019**, *3*, 1140-1151.
41. Lin, Y.; Li, Y.; Zhan, X. Small molecule semiconductors for high-efficiency organic photovoltaics. *Chemical Society Reviews* **2012**, *41*, 4245-4272.
42. Chen, J.; Zhang, W.; Wang, L.; Yu, G. Recent Research Progress of Organic Small-Molecule Semiconductors with High Electron Mobilities. *Adv. Mater.* **2023**, *35*, 2210772.
43. Yi, J.; Zhang, G.; Yu, H.; Yan, H. Advantages, Challenges and Molecular Design of Different Material Types Used in Organic Solar Cells. *Nat. Rev. Mater.* **2024**, *9*, 46–62.
44. Shavez, M.; Panda, A. Effects of π-bridge units on the properties of donor-π-acceptor type benzodithiophene-thienothiophene based polymers for organic solar cells. *Chem. Phys. Lett.* **2020**, *756*, 137810.
45. He, K.; Kumar, P.; Yuan, Y.; Zhang, Z.; Li, X.; Liu, H.; Wang, J.; Li, Y. A Wide Bandgap Polymer Donor Composed of Benzodithiophene and Oxime-Substituted Thiophene for High-Performance Organic Solar Cells. *ACS Appl. Mater. Interfaces* **2021**, *13*, 26441–26450.
46. Fitzner, R.; Reinold, E.; Mishra, A.; Mena-Osteritz, E.; Ziehlke, H.; Körner, C.; Leo, K.; Riede, M.; Weil, M.; Tsaryova, O.; Weiß, A.; Uhrich, C.; Pfeiffer, M.; Bäuerle, P. Dicyanovinyl-Substituted Oligothiophenes: Structure–Property Relationships and Application in Vacuum-Processed Small-Molecule Organic Solar Cells. *Adv. Funct. Mater.* **2011**, *21*, 897–910.
47. Li, Z.; He, G.; Wan, X.; Liu, Y.; Zhou, J.; Long, G.; Zuo, Y.; Zhang, M.; Chen, Y. Solution Processable Rhodanine-Based Small Molecule Organic Photovoltaic Cells with a Power Conversion Efficiency of 6.1%. *Adv. Energy Mater.* **2012**, *2*, 74–77.

48. Zhang, Q.-j.; Zhuang, H.; He, J.; Xia, S.; Li, H.; Li, N.; Xu, Q.-f.; Lu, J.-m. Improved Ternary Memory Performance of Donor–Acceptor Structured Molecules Through Cyano Substitution. *J. Mater. Chem. C* **2015**, *3*, 6778–6785.
49. Niazi, M.R.; Hamzehpoor, E.; Ghamari, P.; Perepichka, I.F.; Perepichka, D. Nitroaromatics as n-type Organic Semiconductors for Field Effect Transistors. *Chem. Commun.* **2020**, *56*, 6432–6435.
50. Irfan, A. Exploring the Electron-Hole Transport Nature and Optoelectronic Properties of 4-Nitro-4′-Amino-Azobenzene-Based Dyes. *Struct. Chem.* **2021**, *32*, 1113–1121.
51. Li, M.; Wu, J.; Wang, G.; Wu, B.; Sun, Z.; Xue, S.; Qiao, Q.; Liang, M. The Donor-Dependent Methoxy Effects on the Performance of Hole-Transporting Materials for Perovskite Solar Cells. *J. Energy Chem.* **2020**, *47*, 10-17.
52. Sun, H.; Guo, X.; Facchetti, A. High-Performance n-Type Polymer Semiconductors: Applications, Recent Development, and Challenges. *Chem.* **2020**, *6*, 1310–1326.
53. Tsizh, B.; Dziamski, Z. Chemical deposition and mechanical application of semiconductors thin films. *Scientific Messenger of LNU of Veterinary Medicine and Biotechnologies* **2021**, *23*, 3-6.
54. Schroeder, B.; Nielsen, C.; Westacott, P.; Smith, J.; Rossbauer, S.; Anthopoulos, T.; Stingelin, N.; McCulloch, I. Effects of alkyl chain positioning on conjugated polymer microstructure and field-effect mobilities. *MRS Communications* **2015**, *5*, 435-440.
55. Raychev, D.; Guskova, O. Charge Carrier Mobility in One-Dimensional Aligned π-Stacks of Conjugated Small Molecules with a Benzothiadiazole Central Unit. *Phys. Chem. Chem. Phys.* **2017**, *19*, 8330-8339.
56. Song, P.; Wang, H. High-Performance Polymeric Materials through Hydrogen-Bond Cross-Linking. *Advanced Materials* **2019**, *32*, 1901244.
57. Ward, J.W.; Li, R.; Obaid, A.; Payne, M.M.; Smilgies, D.-M.; Anthony, J.E.; Amassian, A.; Jurchescu, O.D. Rational Design of Organic Semiconductors for Texture Control and Self-Patterning on Halogenated Surfaces. *Adv. Funct. Mater.* **2014**, *24*, 5052–5058.
58. Xu, B.; Holdcroft, S. Molecular Control of Luminescence from Poly(3-hexylthiophenes). *Macromolecules* **1993**, *26*, 4457–4460.
59. Marsella, M.J.; Swager, T.M. Designing Conducting Polymer-Based Sensors: Selective Ionochromic Response in Crown Ether-Containing Polythiophenes. *J. Am. Chem. Soc.* **1993**, *115*, 12214–12215.
60. Brabec, C.J.; Gowrisanker, S.; Halls, J.J.M.; Laird, D.; Jia, S.; Williams, S.P. Polymer–Fullerene Bulk-Heterojunction Solar Cells. *Adv. Mater.* **2010**, *22*, 3839–3856.
61. Maciejewski, J.; Sobczuk, A.; Claveau, A.; Nicolai, A.; Petraglia, R.; Cervini, L.; Baudat, E.; Miéville, P.; Fazzi, D.; Corminboeuf, C.; Sforazzini, G. Photochromic Torsional Switch (PTS): A

Light-Driven Actuator for the Dynamic Tuning of π-Conjugation Extension. *Chem. Sci.* **2017**, *8*, 361–365.

62. Jozeliūnaitė, A.; Rahmanudin, A.; Gražulis, S.; Baudat, E.; Sivula, K.; Fazzi, D.; Orentas, E.; Sforazzini, G. Light-Responsive Oligothiophenes Incorporating Photochromic Torsional Switches. *Chem. Eur. J.* **2022**, *28*, e202202698.
63. Obrezkov, F.A.; Dashitsyrenova, D.D.; Lvov, A.G.; Volyniuk, D.Y.; Shirinian, V.Z.; Stadler, P.; Grazulevicius, J.V.; Sariciftci, N.S.; Aldoshin, S.M.; Krayushkin, M.M.; Troshin, P.A. Light-Sensitive Material Structure–Electrical Performance Relationship for Optical Memory Transistors Incorporating Photochromic Dihetarylethenes. *ACS Appl. Mater. Interfaces* **2020**, *12*, 32987–32993.
64. Irie, M.; Fukaminato, T.; Matsuda, K.; Kobatake, S. Photochromism of Diarylethene Molecules and Crystals: Memories, Switches, and Actuators. *Chem. Rev.* **2014**, *114*, 12174–12277.
65. Ushiogi, Y.; Hase, T.; Iinuma, Y.; Takata, A.; Yoshida, J. Synthesis of Photochromic Diarylethenes Using a Microflow System. *Chem. Commun.* **2007**, *28*, 2947–2949.
66. Fagan, A.; Bartkowski, M.; Giordani, S. Spiropyran-Based Drug Delivery Systems. *Front. Chem.* **2021**, *9*, 720087
67. Ya.N. Malkin, T.B. Krasieva, V.A. Kuzmin. Quantitative study of the photostability of spiropyrans. *Journal of Photochemistry and Photobiology A: Chemistry* **1989**, *49*, 75-88.
68. Matsushima, R.; Sakaguchi, H. Comparison of the Photochromic Properties of Fulgides and Fulgimides. *J. Photochem. Photobiol. A: Chem.* **1997**, *108*, 239–245.
69. Islamova, N.I.; Chen, X.; Garcia, S.P.; Guez, G.; Silva, Y.; Lees, W.J. Improving the Stability of Photochromic Fluorinated Indolylfulgides. *J. Photochem. Photobiol. A: Chem.* **2008**, *195*, 228–234.
70. Crespi, S.; Simeth, N. A.; König, B. Heteroaryl azo dyes as molecular photoswitches *Nat. Rev. Chem.* **2019**, *3*, 33–146.
71. García-Amorós, J.; Velasco D.; Recent advances towards azobenzene-based light- driven real-time information-transmitting materials. *Beilstein J. Org. Chem.* **2012**, *8*, 1003–1017.
72. Chen, H.; Chen, W.; Lin, Y.; Xie, Y.; Liu, S. H.; Yin, J. Visible and near-infrared light activated azo dyes. *Chin. Chem. Lett.* **2021**, *32*, 2359–2368
73. Zhu, J.; Guo, T.; Wang, Z.; Zhao, Y. Triggered azobenzene-based prodrugs and drug delivery systems. *J. Control Release* **2022**, *325*, 475–493
74. Jousselme, B.; Blanchard, P.; Gallego-Planas, N.; Delaunay, J.; Allain, M.; Richomme, P.; Levillain, E.; Roncali, J. Photomechanical Actuation and Manipulation of the Electronic Properties of Linear π-Conjugated Systems. *J. Am. Chem. Soc.* **2003**, *125*, 2888–2889.

75. Mart, R. J.; K. Allemann, K. R. Azobenzene photocontrol of peptides and proteins. *Chem. Commun.*, 2016, *52*, 12262
76. Sanna, A.L.; Pachova, T.; Catellani, A.; Calzolari, A.; Sforazzini, G. Meta-Substituted Asymmetric Azobenzenes: Insights into Structure–Property Relationship. *Molecules* **2024**, *29*, 1929.
77. Beharry, A. A.; Sadovski, O.; Woolley, G. Azobenzene Photoswitching without Ultraviolet Light. *Journal of the American Chemical Society* **2011**, *133*, 19684-19687.
78. Jerca, F. A.; Jerca, V. V.; Hoogenboom, R. Advances and opportunities in the exciting world of azobenzenes. *Nat. Rev. Chem.* **2022**, *6*, 51-69.
79. Bandara, H.; Burdette, S. Photoisomerization in different classes of azobenzene. *Chemical Society Reviews* **2012**, *41*, 1809-1825.
80. Butler, C. S.G.; King, J. P.; Giles, L. W.; Marlow, J. B.; Vidallon, M. L. P.; Sokolova, A.; de Campo, L.; Tuck, K. L.; Tabor, R. F. Design and synthesis of an azobenzene–betaine surfactant for photo-rheological fluids. *J. Colloid Interface Sci.* **2021**, *594*, 669–680.
81. Wu, Z.; Li, X.; Jiang, X.; Xie, T.; Li, H.; Zhang, G.; Jiang J. Photoswitchable de/adsorption of an azobenzene-derived surfactant on a silica surface. *Phys. Chem. Chem. Phys.* **2019**, *21*, 21030-21037.
82. Cuétara-Guadarrama, F.; Vonlanthen, V.; Sorroza-Martínez, K.; González-Méndez, I.; Rivera, E. Photoisomerizable azobenzene dyes incorporated into polymers and dendrimers. Influence of the molecular aggregation on the nonlinear optical properties. *Dyes Pigm.* **2021**, *194*, 109551.
83. Cunha, M. P.; Foelen, Y.; Engels, T. A. P.; Papamichou, K.; Hagenbeek, M.; Debije, M. G.; Schenning, P. H. J. On Untethered, Dual Magneto- and Photoresponsive Liquid Crystal Bilayer Actuators Showing Bending and Rotating Motion. *Adv. Optical Mater.* **2019**, *7*, 1801604.
84. Bléger, D.; Schwarz, J.; Brouwer, A. M.; Hecht, S. o-Fluoroazobenzenes as Readily Synthesized Photoswitches Offering Nearly Quantitative Two-Way Isomerization with Visible Light. *J. Am. Chem. Soc.* **2012**, *134*, 20597−20600.
85. Beharry, A. A.; Sadovski, O.; Woolley G. A. Azobenzene Photoswitching without Ultraviolet Light *J. Am. Chem. Soc.* **2011**, *133*, 19684–19687.
86. Ohzono, T.; Koyama, E. Effects of photo-isomerizable side groups on the phase and mechanical properties of main-chain nematic elastomers. *Polym. Chem*. **2022**, *13*, 2694-2704.
87. Togari, Y.; Hirota, S.; Kitagawa, H.; Tsukamoto, Y.; Kobayashi K. Hydrogen-bonded six-component assembly for capsule formation based on tetra(4-pyridyl) cavitand and isophthalic

acid linker and its application to photoresponsive capsule. *Org. Biomol. Chem.* **2018**, *16*, 7626-7635.

88. Chu, Z.; Han, Y.; Bian, T.; De, S.; Kraĺ, P.; Klajn, R. Supramolecular Control of Azobenzene Switching on Nanoparticles. *J. Am. Chem. Soc.* **2019**, *141*, 1949−1960.
89. Moldt, T.; Przyrembel, D.; Schulze, M.; Bronsch, W.; Boie, L.; Brete, D.; Gahl, C.; Klajn, R.; Tegeder, P.; Weinelt, M. Differing Isomerization Kinetics of Azobenzene-Functionalized Self- Assembled Monolayers in Ambient Air and in Vacuum. *Langmuir* **2016**, *32*, 10795−10801.
90. Singer N.K.; Schlögl K.; Zobel J.P.; Mihovilovic M.D.; González L. Singlet and Triplet Pathways Determine the Thermal *Z/E* Isomerization of an Arylazopyrazole-Based Photoswitch. *J. Phys. Chem. Lett.* **2023**, *14*, 8956−8961.
91. Reimann M.; Teichmann E.; Hecht S.; Kaupp M. Solving the Azobenzene Entropy Puzzle: Direct Evidence for Multi-State Reactivity. *J. Phys. Chem. Lett.* **2022**, *13*, 10882−10888.
92. Ślusarek J.; Nowoświat A.; Olechowska M. Logistic Model of Phase Transformation of Hardening Concrete. *Materials*, **2022**, *15*, 4403 .
93. Jerca, V.V.; Jerca, F.A.; Rau, I.; Manea, A.M.; Vuluga, D.M.; Kajzar, F. Advances in Understanding the Photoresponsive Behavior of Azobenzenes Substituted with Strong Electron Withdrawing Groups.*Optical Materials* **2015**, *48*, 160–164
94. Sawatzki-Park, M.; Wang, S.; Kleemann, H.; Leo, K. Highly Ordered Small Molecule Organic Semiconductor Thin-Films Enabling Complex, High-Performance Multi-Junction Devices. *Chem. Rev.* **2023**, *123*, 8232–8250; DOI:10.1021/acs.chemrev.1c00945.
95. Fratini, S.; Nikolka, M.; Salleo, A.; Schweicher, G.; Sirringhaus, H. Charge Transport in High-Mobility Conjugated Polymers and Molecular Semiconductors. *Nat. Mater.* **2020**, *19*, 491–502; DOI:10.1038/s41563-020-0611-5.
96. Gu, K.; Loo, Y. The Polymer Physics of Multiscale Charge Transport in Conjugated Systems. *J. Polym. Sci., Part B: Polym. Phys.* **2019**, *57*, 1559–1571; DOI:10.1002/polb.24885.
97. X. Yao, W. Shao, X. Xiang, W. Xiao, L. Liang, F. Zhao, J. Lingd, Z. Lu, J. Li, W. Li, Side chain engineering on a small molecular semiconductor: Balance between solubility and performance by choosing proper positions for alkyl side chains, *Org. Electron*., **2018**, *61*, 56–64.
98. A. Khot, B. M. Savoie, How side-chain hydrophilicity modulates morphology and charge transport in mixed conducting polymers, *J. Polym. Sci.*, **2022**, *60*, 610–620.

99. I. E. Kuznetsov, et al., Tailoring the charge transport characteristics in ordered small-molecule organic semiconductors by side-chain engineering and fluorine substitution, *Phys. Chem. Chem. Phys.*, **2022**, *24*, 16041–16049.

100. P. J. W. Sommerville, A. H. Balzer, G. Lecroy, L. Guio, Y. Wang, J. W. Onorato, N. A. Kukhta, X. Gu, A. Salleo, N. Stingelin and C. K. Luscombe, *ACS Polym. Au*, **2023**, *3*, 59−69.

101. Y. He, N. A. Kukhta, A. Marks and C. K. Luscombe, The effect of side chain engineering on conjugated polymers in organic electrochemical transistors for bioelectronic applications, *J. Mater. Chem. C*, **2022**, *10*, 2314–2332.

102. Datt, R.; Suman; Bagui, A.; Siddiqui, A.; Sharma, R.; Gupta, V.; Yoo, S.; Kumar, S.; Singh, S.P. Effectiveness of Solvent Vapor Annealing Over Thermal Annealing on the Photovoltaic Performance of Non-fullerene Acceptor Based BHJ Solar Cells. *Sci. Rep.* **2019**, *9*, 8529.

103. Yoon, S.; Cho, J.; Yu, S.H.; Son, H.J.; Chung, D.S. Effects of iodine doping on small molecule organic semiconductors for high charge carrier mobility and photoconductivity. *Organic Electronics* **2016**, *34*, 28-32.

104. Lu, X.; Guo, Z.; Sun, C.; Tian, H.; Zhu, W. Helical assembly induced by hydrogen bonding from chiral carboxylic acids based on perylene bisimides. *J. Phys. Chem. B* **2011**, *115*, 10871–10876.

105. Özen, B.; Tirani, F.F.; Schenk, K.; Lin, K.-H.; Scopelliti, R.; Corminboeuf, C.; Frauenrath, H. Structure–Property Relationships in Bithiophenes with Hydrogen-Bonded Substituents. **2021**, *27*, 3348-3360.

106. McCullough, R. D. Regioregular, Head-to-Tail Coupled Poly(3-alkylthiophenes) Made Easy by the GRIM Method: Investigation of the Reaction and the Origin of Regioselectivity. *Macromolecules* **2001**, *34*, 4324–4333.

107. Zhang, Q.; Jiao, L.; Shan, C.; Yang, G.; Xu, X.; Niu, L. Synthesis and properties of ferrocene-functionalised polythiophene derivatives. *Synthetic Metals* **2009**, *14*, 1422-1426.

108. Audebert, P.; Hapiot, P. Fast electrochemical studies of the polymerization mechanisms of pyrroles and thiophenes. Identification of the first steps. Existence of π-dimers in solution. *Synthetic Metals* **1995**, *2*, 95-102.

109. Sheina, E.; Liu, J.; Iovu, M.; Laird, D.; McCullough, R.D. Chain Growth Mechanism for Regioregular Nickel-Initiated Cross-Coupling Polymerizations. *Macromolecules* **2004**, *37*, 3526-3528.

110. Aragoni, M.C.; Arca, M.; Devillanova, F.A.; Hursthouse, M.B.; Huth, S.L.; Isaia, F.; Lippolis, V.; Mancini, A.; Ogilvie, H.R.; Verani, G. Reactions of Pyridyl Donors with Halogens

and Interhalogens: An X-ray Diffraction and FT-Raman Investigation. *J. Organomet. Chem.* **2005**, *690*, 1923–1934.

111. Aragoni, M.C.; et al. Square-pyramidal bonding of I2 molecules at the I- nodes of a polyiodide infinite pseudo-cubic 3D-netword. *Cryst. Eng. Comm.* **2004**, *6*, 87, 540-542.

112. Montis, R.; Arca, M.; Aragoni, M.C.; Bauzá, A.; Demartin, F.; Frontera, A.; Isaia, F.; Lippolis, V. Hydrogen- and Halogen-bond Cooperativity in Determining the Crystal Packing of Dihalogen Charge-transfer Adducts: A Study Case from Heterocyclic Pentatomic Chalcogenone Donors. *CrystEngComm* **2017**, *19*, 4401–4412.

113. George, J.; Deringer, V.L.; Dronskowski, R. Cooperativity of halogen, chalcogen, and pnictogen bonds in infinite molecular chains by electronic structure theory. *The Journal of Physical Chemistry. A* **2014**, *118*, 3193-3200.

114. Holzer, W.; Murphy, W.F.; Bernstein, H.J. Resonance Raman Effect and Resonance Fluorescence in Halogen Gases. *J. Chem. Phys.* **1970**, *52*, 399–407.

115. Arca, M.; Aragoni, M.C.; Devillanova, F.A.; Garau, A.; Isaia, F.; Lippolis, V.; Mancini, A.; Verani, G. Reactions Between Chalcogen Donors and Dihalogens/Interalogens: Typology of Products and Their Characterization by FT-Raman Spectroscopy. *Bioinorg. Chem. Appl*. **2006,** 58937, 1–12.

116. Aragoni, M. C.; Arca, M.; Caltagirone, C.; Castellano, C.; Demartin, F.; Jones, P. G.; Pivetta, T.; Podda, E.; Lippolis, V.; Murgia, S.; Picci, G. Role of the Solvent in the Reactivity of Bis-4-imidazoline-2-selone Derivatives toward I2: An Experimental and Theoretical Approach, *J. Org. Chem.*, **2022**, *87*, 5448–15465.

117. Aragoni, M.C.; Arca, M.; Cherchi, M.F.; Devillanova, F.A.; Garau, A.; Isaia, F.; Lippolis, V.; Verani, G. DFT Calculations, Structural and Spectroscopic Studies on the Products Formed Between IBr and N,N'-dimethylbenzoimidazole-2(3H)-thione and -2(3H)-selone. *Dalton Trans.* **2005**, 2252–2258.

118. Adamo, C.; Barone, V. Exchange Functionals with Improved Long-range Behavior and Adiabatic Connection Methods Without Adjustable Parameters: The mPW and mPW1PW Models. *J. Chem. Phys.* **1998**, *108*, 664–675.

119. Schäfer, A.; Horn, H.; Ahlrichs, R. Fully Optimized Contracted Gaussian Basis Sets for Atoms Li to Kr. *J. Chem. Phys*. **1992**, *97*, 2571–2577.

120. Weigend, F.; Ahlrichs, R. Balanced Basis Sets of Split Valence, Triple Zeta Valence and Quadruple Zeta Valence Quality for H to Rn: Design and Assessment of Accuracy. *Phys. Chem. Chem. Phys.* **2005**, *7*, 3297–3305.

121. Roy, L.E.; Hay, P.J.; Martin, R.L. Revised Basis Sets for the LANL Effective Core Potentials. *J. Chem. Theory Comput.* **2008**, *4*, 1029–1031.
122. Cavallo, G.; Metrangolo, P.; Milani, R.; Pilati, T.; Priimagi, A.; Resnati, G.; Terraneo, G. The Halogen Bond. *Chem. Rev.* **2016**, *116*, 2478–2601.
123. Zhang, Y.; Wang, W. Theoretical Rationale for the Role of Strong Halogen Bond in the Design of Organic Semiconductor Materials. *Comput. Theor. Chem.* **2021**, *1194*, 113074.
124. McAllister, L.J.; Präsang, C.; Wong, J.P.-W.; Thatcher, R.J.; Whitwood, A.C.; Donnio, B.; O'Brien, P.; Karadakov, P.B.; Bruce, D.W. Halogen-bonded Liquid Crystals of 4-alkoxystilbazoles with Molecular Iodine: A Very Short Halogen Bond and Unusual Mesophase Stability. *Chem. Commun.* **2013**, *49*, 3946–3948.
125. De Azevedo Santos, L.; van der Lubbe, S.C.C.; Hamlin, T.A.; Ramalho, T.C.; Bickelhaupt, F.M. A Quantitative Molecular Orbital Perspective of the Chalcogen Bond. *ChemistryOpen* **2021**, *10*, 391–401.
126. Oliveira, V.; Kraka, E.; Cremer, D. *Phys. Chem. Chem. Phys.* **2016**, *18*, 33031–33046.
127. Anderson, L.N.; Aquino, F.W.; Raeber, A.E.; Chen, X.; Wong, B.M. Halogen Bonding Interactions: Revised Benchmarks and a New Assessment of Exchange vs Dispersion. *J. Chem. Theory Comput.* **2018**, *14*, 180–190.
128. Reed, A.E.; Weinstock, R.B.; Weinhold, F. Natural Population Analysis. *J. Chem. Phys.* **1985**, *83*, 735–746.
129. Reed, A.E.; Weinhold, F. Natural Localised Molecular Orbital. *J. Chem. Phys.* **1985**, *83*, 1736–1740.
130. Reed, A.E.; Curtiss, L.A.; Weinhold, F. Intermolecular Interactions from a Natural Bond Orbital, Donor-acceptor Viewpoint. *Chem. Rev.* **1988**, *88*, 899–926.
131. Wiberg, K.B. Application of the Pople-santry-segal CNDO Method to the Cyclopropylcarbinyl and Cyclobutyl Cation and to Cyclobutane. *Tetrahedron* **1968**, *24*, 1083–1096.
132. Luo, J.; Xue, Z.Q.; Liu, W.M.; Wu, J.L.; Yang, Z.Q. Koopmans' Theorem for Large Molecular Systems Within Density Functional Theory. J. Phys. Chem. A **2006**, *110*, 43, 12005–12009.
133. Yang, X.G.; Zhang, Y.; Wang, W.; Ma, L.F. Enhanced Optoelectronic Performances of the Cocrystals Between 2,2'-Bi (1,8-naphthyridine) and Iodine Through Strong Halogen Bonds. *Cryst. Growth Des.* **2022**, *22*, 6863–6869.
134. Zhang, Y.; Tajima, K.; Hirota, K.; Hashimoto, K. Synthesis of All-Conjugated Diblock Copolymers by Quasi-Living Polymerization and Observation of Their Microphase Separation. *J. Am. Chem. Soc.,* **2008**, *130*, 7812–7813.

135. Pandolfi, F.; Rocco, D.; Mattiello, L. Synthesis and characterization of new D-π-A and A-π-D-π-A type oligothiophene derivatives. *Org. Biomol. Chem.* **2019**, *17*, 3018-3025.
136. Kurioka, T.; Komamura, T.; Shida, N.; Hayakawa, T.; Tomita, I.; Inagi, S. Ordered-Structure-Induced Electrochemical Post-Functionalization of Poly(3-(2-ethylhexyl)thiophene). *Macromol. Chem. and Phys.*, **2022**, *223*, 2100435.
137. Liu, J.; Loewe, R.S.; McCullough, R.D. Employing MALDI-MS on Poly(alkylthiophenes): Analysis of Molecular Weights, Molecular Weight Distributions, End-Group Structures, and End-Group Modifications. *Macromolecules* **1999**, *32*, 5777–5785.
138. Ma, S.; Zhou, K.; Hu, M.; Li, Q.; Liu, Y.; Zhang, H.; Jing, J.; Dong, H.; Xu, B.; Hu, W.; Tian, W. *Adv. Funct. Mater.* **2018**, *28*, 1802454.
139. Guimard, N.K.E.; Sessler, J.L.; Schmidt, C.E. Toward a Biocompatible and Biodegradable Copolymer Incorporating Electroactive Oligothiophene Units. *Macromolecules* **2009**, *42*, 502–511.
140. Sakai, N.; Sisson, A.L.; Bürgi, T.; Matile, S. Zipper Assembly of Photoactive Rigid-Rod Naphthalenediimide π-Stack Architectures on Gold Nanoparticles and Gold Electrodes. *J. Am. Chem. Soc.* **2007**, *129*, 15758–15759.
141. Khanasa, T.; Jantasing, N.; Morada, S.; Leesakul, N.; Tarsang, R.; Namuangruk, S.; Kaewin, T.; Jungsuttiwong, S.; Sudyoadsuk, T.; Promarak, V. Synthesis and Characterization of 2D-D-π-A-Type Organic Dyes Bearing Bis(3,6-di-tert-butylcarbazol-9-ylphenyl)aniline as Donor Moiety for Dye-Sensitized Solar Cells. *Eur. J. Org. Chem.* **2013**, 2608–2620.